5-14-2020

Polarization Properties of Broad Lines in Active Galactic Nuclei

Brian Christopher Lake
bcl8886@rit.edu

ROCHESTER INSTITUTE OF TECHNOLOGY

MASTER'S THESIS

Polarization Properties of Broad Lines in Active Galactic Nuclei

---

Author:
Brian Christopher Lake

Advisor:
Dr. Andrew Robinson

A thesis submitted in partial fulfillment of the requirements for the degree of Master of Astrophysical Science and Technology

in the

School of Physics and Astronomy
College of Science
Rochester Institute of Technology
Rochester, NY

May 14, 2020

Approved by: _____ _____

Dr. Andrew Robinson — Date

Director, Astrophysical Sciences and Technology

RIT

ASTROPHYSICAL SCIENCES AND TECHNOLOGY
COLLEGE OF SCIENCE
ROCHESTER INSTITUTE OF TECHNOLOGY
ROCHESTER, NEW YORK

CERTIFICATE OF APPROVAL

MASTER'S DEGREE THESIS

The Master's Degree Thesis of Brian C. Lake has been examined and approved by the thesis committee as satisfactory for the thesis requirement for the master's degree in Astrophysical Sciences and Technology.

Dr. Andrew Robinson,
Thesis Advisor

Dr. Jeyhan Kartaltepe

Dr. Michael Richmond

Date

Acknowledgements

First, I would like to extend my gratitude to my advisor Dr. Andrew Robinson for his unending font of patience and assistance throughout this long process. Furthermore, I thank all of the staff and faculty of the School of Physics and Astronomy at RIT for all they have done throughout my academic career. In particular, I extend thanks to Dr. Dawn Hollenbeck for the many hours which she has allowed me to spend in her office, regardless of the reason.

I thank my entire family for their immense support of my academic career. To my father and mother, I thank you for bolstering my love of learning and for pushing me to pursue higher education. To my grandmother, I am ever grateful for the unending love and faith in my abilities. To my aunt, I am thankful for the nights of laughs and meaningful conversations and for your belief in my success from the very beginning.

I would like to thank the Machulskis family for their incredible support. By opening their home and hearts, I was able to continue this project without worry. I will never forget and never be able to fully repay the generosity extended by Gwen, Tony, and Matthew Machulskis.

Finally – though certainly not least – I would like to acknowledge my second family in Rochester; my amazing friends. To Jess Maffett, Tyler Stick, Brendon Strowe, Devon Christman, Christina Magagnoli, Sarah Messner, Peyton Schmidt, Jacob Cozzarin, Isaac Walerstien, Quinton LoRe, Matthew Machulskis, Sarah MacDonald, and all of the others that have been with me throughout this endeavor, I sincerely thank you. This would not have been possible without the incredible amount of support each and every one of you has given me over the years.

Abstract

The center of every large galaxy is believed to host a supermassive black hole (SMBH). In some of these galaxies, the nuclear region is extremely luminous and far outshines the entire stellar population. Called active galactic nuclei (AGN), these central sources are equally fascinating and perplexing. Due to their immense distance and small size, modern observation techniques are unable to resolve the structure of these regions. However, the polarization of scattered light carries the imprint of the geometry and kinematics of both the sources and the scattering medium. Here, we present a study of the broad Hα lines in a sample of 46 AGN.

Following the work of Smith et al. 2002, 2004, and 2005, we show supporting evidence for the proposed two-component scattering model of AGN using the largest sample of spectropolarimetric observations of broad-line AGN assembled to date. Objects of differing polarization classifications (equatorial or polar) are shown to have significant differences in their distributions of both total flux and polarized flux inter-percentile velocity values. Furthermore, clear distinctions between these classifications are found in polarization position angle and core polarization percentage. These results are supported by Kolmogorov-Smirnov tests between the classifications and are in accordance with those suggested by previous studies.

We also explore the validity of a spectropolarimetric method of estimating SMBH masses. In general, SMBH mass estimates require information on the inclination of the object in the sky, but we can avoid requiring this information by using polarized inter-percentile velocity measurements instead. Using this method, we achieve estimates on the order of 10^6 to 10^8 solar masses – estimations consistent with both the expected values and those in the literature.

Contents

1 Active Galactic Nuclei

Certain galaxies have been observed to have extremely luminous central regions with brightnesses far greater than stellar mechanisms could produce. The spectra of these objects further separate them from stellar emission. While the blackbody-like continuum emission of stars peaks between the ultraviolet and near-infrared portions of the electromagnetic spectrum, the emission of these central regions spans the entire spectrum: from gamma rays to radio waves. These objects also exhibit emission lines from a wide range of ionic species which vary in strength, width, and shape between individuals.

The nuclei of these objects remain unresolved by modern telescopes, which indicates that they are incredibly small and massively powerful. The most likely engine to drive such emission is a supermassive black hole (SMBH) which is actively consuming matter in the form of dust and gas surrounding it. As this material falls inwards due to the intense gravity of the SMBH, its gravitational potential energy is converted to internal kinetic energy. This energy expresses itself as a very hot, very broad spectrum.

These intriguing objects are quite aptly named active galactic nuclei (AGN).

1.1 The Central Engine

Gas orbiting the central SMBH has some net angular momentum. The infalling of this gas causes it to flatten, eventually forming a thin disk around the SMBH called an accretion disk. Within this disk, viscous friction between the individual molecules of the gas heats up the ensemble of particles whilst the angular momentum of the system is transferred outwards along the plane of the disk. This generated heat is emitted from the surface of the disk as blackbody radiation.

Under these conditions, two geometries can be considered: thin disks and flared tori. In the simple case of thin disks, the temperature at which the disk radiates is proportional to the radius (Peterson 1997):

$$T \propto r^{-0.75} \tag{1}$$

This radial dependence forms a collection of rings which each radiate as blackbodies of different characteristic temperatures. As a result the total spectrum would be a composite of each of these

blackbodies, culminating in a much broader spectrum than a single-temperature blackbody.

This accretion of material is extremely efficient, converting about 10% of the rest mass energy of accreted gas into thermal emission (compared to the 0.7% converted by fusing Hydrogen into Helium). Furthermore, the process uses very little mass, consuming on the order of about one solar mass of material per year. Due to its high efficiency, such a small amount of mass is sufficient to power a luminous quasar. While its efficiency is unparalleled, it does require a continuous supply of fuel to remain active. The gas orbiting the SMBH cannot infall without losing angular momentum and thus the activity in the nucleus will cease once the inner portions of the gas are consumed. It is for this reason that, despite the current belief that most galaxies host a SMBH at their core, not all galaxies have active galactic nuclei.

Despite SMBHs being necessary for the incredible amounts of energy produced by AGN, they are unable to be directly observed. Instead, their presence is mostly inferred by gravitational effects on the surrounding matter (such as stars and gas). Further inference can be made by tracing kinematics of stellar objects in the same region. The most conclusive evidence comes from the direct imaging of the central radio source of M87, the results of which are consistent with a spinning SMBH (Akiyama et al. 2019).

1.2 Classification of AGN

The term "active galactic nuclei" encompasses many different objects each with their own characteristics. In general, AGN are classified by looking at two main factors:

1. Presence and characteristics of line emission
2. Morphology of radio emission
3. Bolometric luminosity

In some of these cases, the individual classifications represent objects that have different underlying physical processes governing their energy production. In others, the difference is thought to simply be a difference in orientation. The latter of these cases is explored more in section 1.5.1.

1.2.1 Radio-Quiet Objects

Radio-quiet AGN are objects which do not exhibit strong emission in the radio portion of the electromagnetic spectrum. Furthermore, they do not have the characteristically powerful jets nor extended radio lobes (on the order of tens of kiloparsecs) associated with radio-loud objects (explored in section 1.2.2). Despite this, some radio-quiet objects host radio sources on the scales of kiloparsecs which can have similar morphological features – such as jets and lobes – to radio-loud AGN.

1.2.1.1 Seyfert Galaxies

The Seyfert classification was originally defined to contain spiral galaxies with star-like nuclei and broad emission lines following the original study of these objects conducted by Carl Seyfert (Seyfert 1943). These objects are now classified by their spectroscopic properties and are further broken down into two main categories: Seyfert 1 and Seyfert 2 galaxies.

Seyfert 2 galaxies are defined by narrow-line emission superimposed on their continuum emission (which is mainly due to host galaxy starlight). These emission lines have full-width at half-maximums (FWHMs) on the order of hundreds of kilometers per second. Furthermore they can display emission lines which correspond not only to permitted transitions, but also to forbidden transitions.

Seyfert 1 galaxies display the same narrow lines as Seyfert 2s, but their spectra also contain superimposed broad-line and accretion disk emission. These broad lines have FWHMs on the order of thousands of kilometers per second.

Seyfert 1 galaxies are further classified into Seyfert 1.5, 1.8, and 1.9 galaxies. As the number in these classes approaches 2, the broad line strength weakens compared to the strength of the narrow lines. Another classification is the narrow-line Seyfert 1 (NLS1) galaxy. These objects have strong broad lines that are significantly narrower than those of normal Seyfert 1 galaxies. Furthermore, NLS1s have extreme x-ray properties, steep hard x-ray slopes, and exhibit rapid variability in luminosity. Seyfert 1.5s, 1.8s, and 1.9s are thought to be "normal" Seyfert galaxies with low luminosities, while NLS1s are believed to be AGN with lower mass black holes (Barthe, Greene, & Ho; Botte et al. 2004) accreting at a high rate (Collin & Kawaguchi; Warner, Hamann, & Dietrich 2004).

It is believed that these objects are both powered by the same physical mechanism, only viewed

from a different orientation. Under this assumption, the existence of the two types implies that there exist two regions within this class of AGN. The characteristics of each spectra can be used to determine the geometry and physical situations for each of these areas of the AGN.

The first region is known as the broad-line region (BLR) which exists towards the center of the galaxy. The gas of this region orbits the SMBH closely and thus experiences high-velocity bulk motion which results in large line widths. Furthermore the gas in the BLR is of high density, effectively suppressing forbidden transitions via collisions between particles.

The second is known as the narrow-line region (NLR) which exists in the conular area perpendicular to the plane of rotation and further from the center than the BLR. Gas in these regions is far removed from the SMBH and therefore has lower bulk velocities which produce narrow emission lines. The NLR is also far less dense and the rate of collision is not enough to suppress forbidden transitions.

As mentioned earlier, Seyfert 1 and 2 galaxies are thought to be the same objects viewed at different orientations. This variance in viewing angle prohibits observations of the BLR in certain cases due to a proposed optically thick torus of gas and dust which surrounds the accretion disk. In the case that the line-of-sight between the observer and the nucleus of the AGN is blocked by the torus, a Seyfert 2 is observed (since the light from the BLR is blocked by the torus). If the nucleus is not obstructed by the torus the light from the BLR makes it to the observer and a Seyfert 1 is observed. This is one of the fundamental concepts behind the Seyfert unification scheme (as we will discussed further in section 1.5.1)

1.2.1.2 Quasi-Stellar Objects

Quasi-Stellar Objects (QSOs) have spectra similar to Seyfert 1 galaxies, but have much higher luminosities. In many cases, the brightness of the nucleus of these objects drowns out the stellar light components of the host galaxies, though in some cases the two sources can be separated. The systems which host these objects seem to be preferentially disturbed systems (Disney et al. 1995; Disney 1998) which raises the possibility that their intense emission may be a result of extra fuel being introduced by inter-galactic collisions.

About ten percent of these objects display UV absorption features that are significantly blue-shifted. This implies that absorbing gas is escaping the system at velocities of about $0.1c$. Called broad-absorption line quasars, this classification is thought to be caused by the orientation of these QSOs. A number of mechanisms are proposed including absorbing clouds that cover about 10%

of the object's solid angle (Weymann et al. 1991), strong polar outflows (Barthel 1992), or accelerated gas escaping from the surface of the torus (Weymann et al. 1991).

1.2.2 Radio-Loud Objects

Radio-loud AGN are objects which exhibit strong radio emission due to synchrotron radiation (explored in section 2.4.3). Radio-loud AGN are mainly described by their high radio luminosity and can exhibit a range of morphologies. Some of these objects display extended lobes powered by jets. These objects make up about 15% of all observed AGN but this percentage increases alongside optical and X-ray luminosity (Urry, & Padovani 1995). For example, the population percentage can increase by between 20% and 50% as the luminosity in these portions of the spectrum increases for AGN with absolute bolometric magnitudes of ≤ -24.5 (Padovani 1993). Furthermore, these AGN seem to be preferentially hosted by elliptical galaxies (Hutchings, Janson, & Neff 1989; Taylor et al. 1996).

Radio-loud objects have been observed displaying very large ranges of morphology, but can generally be broken down into two main classes: the extended region and the compact region. The extended region consists of two lobes of high radio luminosity. These lobes are symmetric about the core – the compact region – of the system and can have structure on scales of megaparsecs. These lobes are connected to the core via linear features called "jets" which transport energy and particles outwards at relativistic speeds. Though these jets tend to be isotropic, their relativistic nature causes them to have luminosities that are highly dependent on orientation (this effect is called relativistic beaming and is explored in more detail in section 2.4.3).

This orientation-based nature of jet luminosity means that radio-loud AGN themselves have extremely different observed characteristics depending on their relative positioning. One effect of this is that these objects are either jet dominated (when the line of sight is close to that of one of the jets) or lobe dominated (when the jets are not in line with the observer). In the case of a jet-dominated radio loud AGN, the opposite jet becomes incredibly difficult to observe. Due to relativistic beaming, the observed luminosity in the direction anti-parallel to the velocity of the relativistic plasma is very low. In cases where these jets are nearly in-line with the observer, supposed superluminal motion can be observed due to the relativistic nature of the accelerated particles in tandem with their orientation.

It is currently unclear why AGN divide into radio-quiet and radio-loud populations. Despite this, a number of factors including galaxy type, rate of nuclear fuelling, and the spin of the central black

hole have been identified to contribute to whether a galaxy is radio loud or not.

1.2.2.1 Types of Radio-Loud Galaxies

In addition to radio emission morphology, radio-loud AGN are further classified by the properties of their emission lines and luminosity. Unsurprisingly, this similar classification scheme produces a series of analogues to the radio-quiet galaxy types discussed in section 1.2.1.

Broad Line Radio Galaxies (BLRGs) and Narrow Line Radio Galaxies (NLRGs) are analogous to Seyfert 1 and Seyfert 2 galaxies (discussed in section 1.2.1.1) respectively. These objects are usually lobe-dominated and, like radio-loud objects as a whole, are preferentially located within elliptical galaxies (as compared to the spiral hosts of Seyfert galaxies). The emission line properties of BLRGs and NLRGs are very similar to those of their Seyfert counterparts.

Quasars are analogous to QSOs (discussed in section 1.2.1.2). Quasars can be both lobe- or core-dominated but are almost always observed to only have a single jet. This is likely due to one of the jets being faced away from the observer, causing it to dim drastically (as mentioned in section 1.2.2). Much like QSOs these objects exclusively exhibit type 1 spectra (those with characteristics similar to Seyfert 1s), an effect that is similarly explained by a line of sight along the rotational axis of an optically thick torus in a proposed radio-loud unification scheme (which we will touch upon in section 1.5.2).

Blazars do not have an apparent radio-quiet analogue as their spectra contain a host of rather odd properties. First and foremost, these objects have smooth, featureless continuum emission ranging from radio to optical and – in some cases – even ultraviolet wavelengths. Their luminosity varies rapidly and the degree of polarization of observed light is variable on scales of around 5% to 50%. These odd properties are well-described by beamed synchrotron radiation along the line of sight. High apparent superluminal motion observed around these objects is further evidence for this proposition.

1.2.3 Related Phenomenology

Certain objects seem to display properties similar to those of AGN, but do not have obvious connections to them. These objects are often discussed in tandem with AGN, but their fundamental processes may be quite different.

1.2.3.1 Starburst Galaxies

Starbursts are galaxies that exhibit higher-than-average star formation rates as compared to normal galaxies. While this increased star formation rate can exist throughout the galaxy, it tends to be concentrated within the nucleus and/or in rings surrounding the central region. As a result, these galaxies are observed to have HII-region-like spectra with significant amounts of optical emission being produced by the newly birthed stars. It is believed that this increase in star formation is caused by similar mechanisms to those which fuel AGN: galactic interactions or other galaxy-scale perturbations. Despite the commonality in cause, the link between starburst galaxies and AGN is unclear.

Despite their specific connection being uncertain, it has been previously noted that AGN are more likely to exist in starbursts (Heckman et al. 1995). This observation has lead to the proposition of a possible evolutionary link between the two types of galaxies. In this model, a galaxy is interacted with or otherwise perturbed such that large amounts of gas are funneled towards the center. This gas then creates a compact region of star formation which eventually leads to the activation of a SMBH. The excess fuel in the region – the remaining stellar population – feeds the SMBH at a high rate and leads to an AGN (Norman & Scoville 1988).

1.2.3.2 Ultra-Luminous Infrared Galaxies

Ultra-Luminous Infrared Galaxies (ULIRGs) are among the most intensely bright objects in the infrared and boast luminosities exceeding $10^{12}L_{\odot}$ in those wavelengths. They emit approximately 90% of all their light in these wavelengths through what is presumed to be thermal heating of dust due to optical and ultraviolet sources. ULIRGs tend to display properties consistent with obscured AGN, pointing to either an embedded AGN, starburst, or both. The fraction of ULIRGs that exhibit those properties increases with infrared luminosity.

The most powerful ULIRGs appear to be late-stage mergers, effectively having large amounts of gas transported to their cores. This excess of material triggers infrared radiation as a result of heated dust caused by an accreting SMBH and/or starburst activity. It is possible that these objects may be evolutionary predecessors to QSOs (see section 1.2.1.2).

1.2.3.3 Low-Ionization Emission Line Region Galaxies

Low-Ionization Emission Line Regions (LINERs) are objects with spectra similar to Seyfert 2 galaxies (see section 1.2.1.1). These objects make up a significant amount of the local galaxy population, being found in about 19% of galaxy cores. In contrast to Seyfert 2 galaxies, they exhibit strong low-ionization lines – such as OI and NII lines – but have relatively weaker high-ionization lines – such as OIII.

Their relationship to AGN is unclear, but it is proposed that they may be powered by a Seyfert-like continuum. This idea is supported by the existence of broadened Hα features in some LINER spectra. Another proposed source is shock heating or ionization from hot stars rather than the accretion disk of a central SMBH.

1.3 Continuum Emission Mechanics

Normal galaxies have pseudo-blackbody spectra that peak in the near-infrared wavelengths due to their (mostly) stellar sources. AGN spectra, on the other hand, are populated by a series of sources ranging from radio to gamma wavelengths. The spectra of an AGN can be utilized to determine their classification, allowing us to differentiate between radio-loud and radio-quiet objects and – within the radio-loud regime – between blazars and non-blazars.

Blazars have the most obvious spectra, being rather smooth from radio to ultraviolet wavelengths. Despite their smoothness, they are observed to be highly variable (Angel & Stockman 1980). It is believed that the lower-wavelength light is produced via Doppler boosting of the light emitted by synchrotron processes. X-ray emission within their spectra is thought to be the result of inverse Compton scattering (the scattering of lower-energy photons by relativistic electrons). This jet-produced spectrum is enough to drown out any thermal or line emission that exists in these objects.

Non-blazars display a series of distinct features such as the "Big Blue Bump," the 1 μm minimum, and the sub-mm break that indicate multiple emission components. Radio-quiet and radio-loud objects only differ significantly in the radio portion of their spectra, retaining similar characteristics elsewhere. It is unclear how much radiation in these spectra is a result of fundamental processes within the AGN versus secondary processing of the initial radiation.

The simple accretion disk model mentioned in section 1.1 predicts a quasi-blackbody spectrum from optical to soft x-ray wavelengths. There is no direct evidence for these structures since

they are unable to be resolved using modern techniques. Despite this, strong red-ward asymmetry of the broad Fe Kα line (in the x-ray regime) is consistent with gravitationally redshifted thermal emission at the center of an accretion disk surrounding a SMBH (Fabian et al. 1995; Nandra et al. 1997).

The Big Blue Bump is also thought to be from thermal emission of an accretion disk. This feature encompasses over one-half of the bolometric luminosity of obscured, non-blazar AGN. The bump extends from the micrometer regime to the ultraviolet and peaks at approximately 1000Å. This feature is of particular importance as it is likely to be the source of the ionizing radiation that produces both broad- and narrow-line emission.

Though the simple accretion disk model aligns with many of the features of AGN continua, there are issues that arise from observational data. Assuming the emission from the accretion disk is a result of heating from a central source, we would expect to see time variations "echo" across different wavelength regimes. This is due to the fact that the energy from the central source should radiate outwards at the speed of light and be re-emitted at various blackbody temperatures throughout the disk. In practice, we do not see lagging in variability between different wavelength regimes (Clavel et al. 1991; Clavel et al. 1992; Krolik et al. 1991). This implies that the radiation of the accretion disk is emitted simultaneously rather than being emitted at different times. These observations lead to models of disks with temperature gradients not determined by viscous effects, but rather a variable x-ray source powering the entirety of the disk (Collin-Souffrin 1991; Haardt, Maraschi, & Ghisellini 1994; Krolik et al. 1991).

Further issues are shown in the predicted polarization in type 1 objects. An optically thick, geometrically thin accretion disk should produce light that is significantly polarized (ranging from 0% to 11.7%) with an electric field vector perpendicular to the disk's axis of rotation (Antonucci 2001). Observations, on the other hand, tend to show that the polarized light has electric field vectors that are instead parallel to the axis of rotation. It has, however, been shown that this is compatible with some form of an accretion disk model. In the case of an optically and geometrically thick disk – under the assumption that most of the radiation originates in the inner funnel – multiple scattering can cause polarized light with electric field vectors that are perpendicular to the axis of rotation (Coleman & Shields 1990).

The final important component of AGN continua is the thermal emission from extended dusty regions heated by optical and ultraviolet radiation. This light is re-emitted with the same variability in the infrared albeit it with a smaller amplitude and over longer timescales. This emission also lags behind the shorter-wavelength emission which indicates that this dust exists far from the central

source. Furthermore, it allows us to determine the general location of these features. Since the optical light emitted from the central region travels at the speed of light, we know that the radial distance from the emission disk to this extended region (R) is related to the time lag between the optical and infrared signatures (Δt):

$$R < c\Delta t \tag{2}$$

The radial location must be less than this maximal value since light may propagate through non-empty space to reach that point.

1.4 Line Emission

In addition to the continuum emission described in section 1.3, AGN spectra display an abundance of line emission. These lines are split into two main categories – narrow lines and broad lines – on the basis of their width and are thought to be produced by separate mechanisms in distinct regions.

1.4.1 The Narrow-Line Region

The narrow-line region (NLR) is an area with temperatures on the order of about 10^4K and electron number densities of order approximately 10^{10}m^{-3} as indicated by intensity ratios of forbidden lines (Osterbrock 1993). These regions have large spacial scales (on the order of hundreds of parsecs) and thus can be resolved in nearby AGN. These observations have revealed that the NLR appears to be fan-like in two dimensions which is indicative of a projected cone (Christopoulou et al. 1997; Evans et al. 1993; Macchetto, Capetti, & Sparks 1994; Mundell, Holloway, & Pedlar 1995; Pogge 1989).

Narrow-line emission has been determined by both the Hubble Space Telescope and ground-based observation to be closely associated with radio emission. One major correlation is the alignment of OIII lines with the radio axis. Furthermore, objects with linear radio sources tend to have higher narrow-line widths and the highest velocity gas in these regions occurs in areas of radio emission.

Results of observation have implied that the structure, kinematics, and emission of the NLR are influenced by both the ionization cone from the central source (see section 1.5.1) as well as interactions between the radio jet plasma and the gas within the NLR (Das et al. 2006). Shocks from

radio plasma cause sections of the NLR gas to expand and cool by emitting light. The width of these emission lines is low due to the fact that this gas does not have a particularly high bulk velocity. In objects with extended radio lobes, the narrow-line emission originates from arc-like shells thought to be bow-shocks at the interface between the plasma and the emitting gas. These shocks also provide additional ionization in the region.

Beyond the NLR exists the extended narrow-line region (ENLR) which is located at radii on the order of several kiloparsecs. These regions also appear to be fan-like and are again believed to be cones projected into two dimensions. They are thought to be made of interstellar gas that is ionized by radiation from the core, though it is possible that radio emission may also play a role. The emission in this region is narrower than that of the NLR and displays kinematics consistent with galactic velocity fields.

1.4.2 The Broad-Line Region

Much like the accretion disk, the broad-line region (BLR) is a compact region that is unresolvable in even the nearest AGN. As such, the characteristics of this region must be inferred through indirect means. A lower limit on the electron number density can be determined due to the lack of forbidden lines. The omission of these lines from the spectra indicates that they are collisionally suppressed which places this constraint. The semi-forbidden CIII line pair is observed in many cases which places an upper limit on the electron number density of about 10^{16}cm^{-3}. The intensity ratio of these two lines also allow a temperature estimate of approximately 10^4K to be formulated (Netzer 1990).

While these values are useful for understanding the overall properties of the region, it is presumed that there are various different locations at which emission occurs. Each of these separate locations are defined by their own physical conditions and thus make it difficult to describe the BLR as a whole. In fact, the "echoing" of different emission lines (see below) occurs at different times with high-ionization lines first and low-ionization lines last. This implies that these sections of gas are structured in such a way that the highly ionized material is closer to the central source than the lowly ionized material (Kassebaum, Peterson, & Wanders 1997; Peterson et al. 1991; Ulrich, Maraschi, & Urry 1997).

Variations in the broad-line emission correlate to those in the continuum which implies that the BLR is powered by photoionization from the core. The time delay in these different emission variations can again be used to determine the maximum distance at which the BLR begins (via

equation 2). This process is known as reverberation mapping and is touched upon below. The size of the BLR seems to be directly related to the bolometric luminosity of the object, with larger BLRs being attributed to brighter objects (a fairly precise relationship is $R_{BLR} \propto L^{1/2}$) (Carone et al. 1996; Kaspi et al. 2000). Low luminosity objects have BLRs as small as 0.3 parsecs, but they are geometrically thick (with outer radii approximately ten times further extended than their inner radii) (Vestergaard, Wilkes, & Barthel 2000).

Since the BLR is unresolved, we are unable to determine very much about the velocity field(s) of the gas clouds and/or flows nor the spacial distribution(s) of the material. The only aspects of the BLR that we are confident about are that the width of the emission is caused by bulk motion and that this emission is a result of photoionization from the core. Beyond this, there isn't a consensus regarding the physical layout of the BLR. Many models have been suggested including outflows (Zheng, Binette, & Sulentic 1990), irradiated stellar chromospheres (Alexander & Netzer 1994; Edwards 1980; Penston 1988), supernova remnants (Terlevich et al. 1992), Keplerian cloud ensembles (Bradley & Puetter 1986; Wanders et al. 1995), and extended accretion disk regions (Collin-Souffrin et al. 1988). If the BLR is composed of individual clouds, an extremely large amount of them would be required in order to account for the smoothness of the line profiles.

Broad-line profiles are rather diversely shaped across the population of AGN (Eracleous & Halpern 1994; Robinson 1995; Stripe 1991). Profiles of individual broad lines can also differ substantially, supporting the idea of a stratified BLR as mentioned above (Halpern et al. 1996). A multitude of features – including shoulders, red-ward or blue-ward asymmetries, and double peaks – suggest that the BLR is comprised of multiple emission components. Of these features, double peaked profiles are of the most interest. Double peaks occur mainly in the Balmer lines of radio-loud objects (Eracleous & Halpern 1994) and are thought to be the result of a rotating disk. These kinds of disks are already supported in AGN by the idea that the central source of these objects is an accretion disk surrounding a SMBH.

The profile produced by a rotating disk is orientation-dependant due to the difference in line-of-sight velocity profiles. In the case of a face-on disk, the profile is expected to be single peaked and rather narrow since the velocity differences are mostly in the plane of projection. For edge-on disks, the profile should display a pair of broad double peaks (one redshifted and one blueshifted) due to the fact that one portion of the disk is rotating towards the observer while the other is rotating away. This model is supported by a correlation between the inferred inclination and the full-width at half-maximum of Hβ lines. A major issue with the disk model is that only about 10% of BLR galaxies exhibit noticeable double peaks. It is possible, however, that these peaks could be

suppressed in the case of a gas-dominated core and/or a relatively low rotational velocity of a very extended disk.

Due to the fact that the BLR is unresolved and that not much information can be garnered from the various emission lines, different methods of understanding its structure must be employed. One of these methods is reverberation mapping. By examining the time delay between variations in the continuum and those in each emission line, it is theoretically possible to determine the spacial distribution and kinematic properties of the BLR. For example, a BLR with radial outflow would echo variations in the blue portion of each line before the red portions due to the fact that the blue-shifted gas is traveling towards the observer. While the information gathered from this method is useful, it is unfortunately very difficult to obtain. Not only must the data used be of high quality, but it is necessary to achieve good sampling across the profile. These two factors mean that reverberation mapping of objects requires a large amount of telescope time and thus these types of studies are few in number.

Another method that is commonly discussed is that of spectropolarimetry. Spectropolarimetry (discussed at length in chapter 2) is the study of the polarization properties of light as a function of wavelength. By looking at the scattering elements of AGN, we are able to examine what these scatters "see" of the source. In objects with direct lines of sight to the BLR, this information is invaluable as it allows us to compare our observations of the source spectrum to those "made" by scattering elements. With these two pieces, it is possible to test orientation-dependent models of AGN.

1.5 AGN Unification Schemes

Though we discussed many different types of AGN throughout section 1.2, there are many similarities in their spectra. This indicates that the mechanisms that drive these objects is also similar and that the observed differences stem from a relatively small number of factors. Furthermore, radio-loud and radio-quiet objects are nearly identical in their spectra, save for the radio regime. This further indicates that most AGN are – in essence – very similar objects. Effectively, unification schemes attempt to internalize this idea, proposing that the differences in AGN spectra are resultants of orientation effects.

1.5.1 The Seyfert Unification Scheme

The major indication of unification between Seyfert objects is the existence of broad-line and Fe II emission in the polarized flux spectrum of Seyfert 2 galaxy NGC 1068 (Antonucci & Miller 1985). The presence of these lines in the spectrum indicates that both Seyfert 1 and Seyfert 2 galaxies are the same object, but viewed at different orientations. A Seyfert 2 spectrum is observed when the line-of-sight to the observer is obstructed by the circum-nuclear torus, blocking the light from the BLR. When viewed along the rotational axis, we observe a Seyfert 1 spectrum due to the lack of blockage by the torus.

It is presumed that the broad-line and Fe II emissions found in NGC 1068 are scattered by material in the polar region of the object, thus showing the lines prominently in the polarized flux spectrum but not the total flux spectrum. Furthermore, the observation of narrow-line emission in both Seyfert 1 and Seyfert 2 galaxies further implies that the NLR also resides in the extended polar region. This has lead to the unification scheme depicted in figure 1.

Polarized broad lines have been observed in many Seyfert 2 galaxies other than NGC 1068. Despite this, utilizing the polar scattering model described above can be rather problematic for certain objects. This is due to the fact that some of these objects display optical polarization percentages significantly lower than expected from this process. Furthermore, this polarization percentage decreases in wavelength sections that display broad lines. If a polar scattering region was responsible for the appearance of polarized light continua and broad lines, they should share a similar percentage polarization since they have the same scattering path.

It is possible that this lower-than-expected polarization percentage is a result of dilution from a unpolarized source. While this is generally accepted, the origin of this unpolarized light is debated. The simplest solution is that the light is emitted by the stellar population of the host galaxy, but it is unclear whether or not enough light would be produced by these processes. Another possibility is that the AGN continuum emission region extends slightly above the torus, allowing us to see some of that emission in Seyfert 2 galaxies. It could also be that free-free electron interactions in the polar scattering region are the progenitors of this light. It has, however, been observed that Seyfert 2 continua can be dominated by starbursts in the nuclear region; this points to stellar mechanisms being the main cause of the discrepancy.

Non-photometric arguments further support the Seyfert unification scheme. Firstly, there is an observed “photon deficiency” between what is seen in the continuum of Seyfert 2 galaxies and the amount required to produce the characteristic narrow lines. This suggests a hidden ionizing source

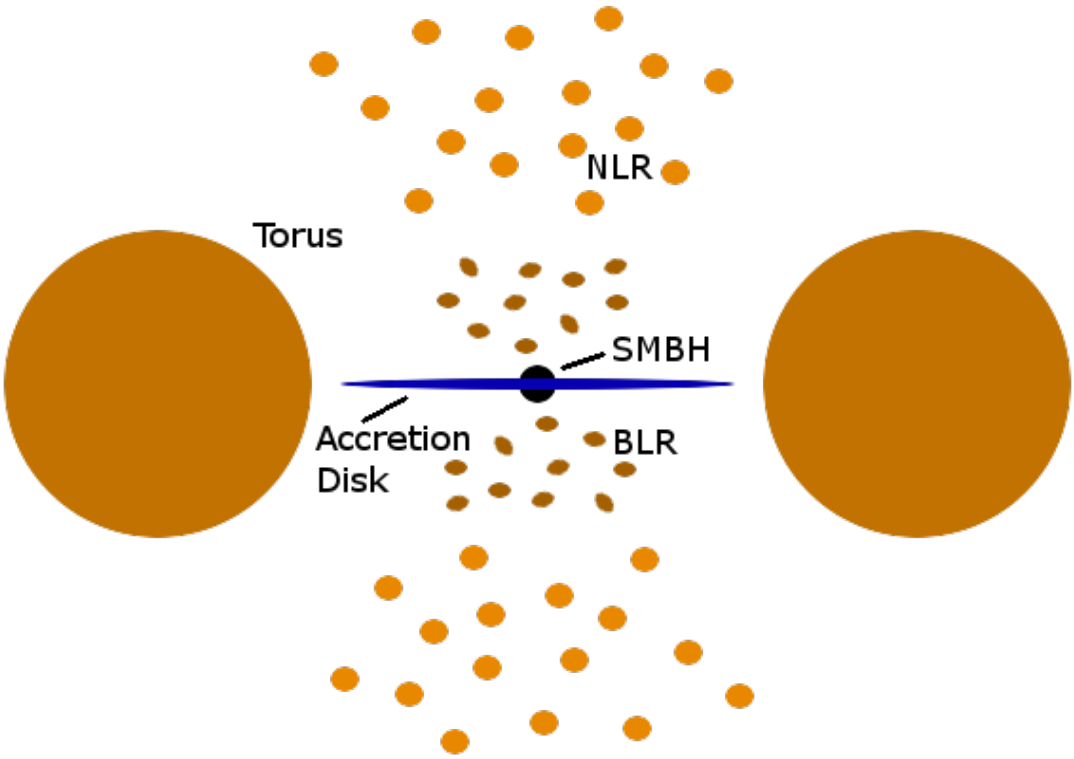

Figure 1: A cross-section of the proposed Seyfert unification scheme. The black circle and blue disk in the center of the figure represent the SMBH and its accretion disk respectively. The two large circles represent a dusty torus surrounding the entire nuclear region. The small, brown, almond-shaped blobs near the accretion disk are broad-line region clouds while the larger tan objects in the same axis represent the narrow-line region clouds.

obscured by a circum-nuclear torus of optically thick material. Furthermore, mapping of narrow-line emission shows that the ionization in these objects is strongly found within co-axial cones. This implies that light from the core is ionizing the material anisotropically, more specifically that it is "funneled" into co-axial cones by the torus.

Observations of infrared broad lines have also been made, pointing to an obscured BLR. These lines experience less extinction while traveling throughout the material and thus are not absent like those of higher wavelength. Seyfert 1 objects have shown higher emission in the soft X-ray portions of their spectra, indicating a higher Hydrogen column density. This is thought to be directly related to Seyfert 1s being viewed along the system axis.

The key component of the Seyfert unification scheme is the torus, a geometrically and optically thick "donut" of dusty material surrounding the core of the AGN. Due to the unresolved nature of the torus, not much is known about its structure and/or makeup. It is thought to be composed of material which absorbs optical and ultraviolet light and then re-emits that light in the infrared. Structures thought to be representative of the torus have been observed using infrared (Marco & Alloin 2000) and molecular emission mapping (Jackson, Paglioni, & Ishizuki 1993; Planesas, Scoville, & Myers 1991; Tacconi et al. 1994).

It is unclear whether or not this unification model can be applied to all Seyferts. Spectropolarimetry studies have shown that only approximately one-third of Seyfert galaxies display polarized broad lines. A correlation was discovered between the presence of the polarized broad Hα line and the IRAS f_{60}/f_{25} ratio wherein only objects with "warm" IRAS colors ($f_{60}/f_{25} < 4.0$) contained them (Heisler, Lumsden, and Bailey 1997). This is thought to be another orientation effect, as those objects with a "cool" IRAS color had the majority of their polar scatterers and hot central dust blocked by the torus. In this case, objects that have polarized broad lines in their spectra would have a higher inclination than those without.

Unfortunately, this interpretation is met with one major issue. X-ray observations of Seyfert 2s have displayed that those with both warm and cold IRAS colors have similar column densities towards the nucleus. This is contrast to what is expected: higher column densities in cool objects due to the material of the torus blocking the view of the central engine. However, it has been noted that the IRAS color is not a measure of inclination, but rather the presence of significant star formation (or lack thereof). Excess star formation could lead to dilution of these polarized broad lines through the introduction of a large amount of unpolarized light.

Despite supporting evidence, there exist significant challenges to the unification scheme. It is likely that not *all* Seyfert 2 objects are simply Seyfert 1s obscured by a circum-nuclear torus. Rather this

unification scheme is most probably correct to low-order approximations, but many other factors influence the specific mechanisms, morphology, and characteristics of each system.

1.5.2 Radio-Loud Unification Schemes

A similar relationship to that between Seyfert 1 and 2 objects can be drawn between quasars and NLRGs. NLRGs have been observed to display both polarized broad lines and broad lines in the infrared regime. It follows that NLRGs could simply be quasars obscured by a circum-nuclear torus.

The anisotropy of radio morphology is also a strong indicator of a unified model. The differences between core- and lobe-dominated objects are almost certainly due to orientation effects. Furthermore, it is strongly believed that blazars are simply objects with their line-of-sight axis aligned with the radio axis.

1.6 Spectropolarimetry of Seyfert 1 Galaxies

The orientation of the electric field vector of optical polarized light (polarization vectors) in Seyfert 2 galaxies is almost always perpendicular to the system axis. This is consistent with polar scattering of emissions from the central engine. Seyfert 1 galaxies, on the other hand, do not generally display polarization vectors of the same directionality.

Seyfert 1 objects, despite being viewed from a higher inclination, should still display polarization vectors perpendicular to the system axis (assuming the scatterers are located along the poles). More often than not though, Seyfert 1s have polarization vectors that are parallel with the system axis. This implies the existence of an equatorial scattering region that surrounds the core.

The location, structure, and kinematics of this source of polarized light are currently unknown, but its signature is not present in Seyfert 2 objects. It is possible that the scattering region is obstructed by the torus in the case of these objects. This could also be a result of both sources (polar scattering included) being directly visible in Seyfert 1s with one dominating the other in terms of brightness.

Spectropolarimetry is useful in determining the geometry of scattering regions within objects, but it is also extremely useful for understanding the BLRs of Seyfert 1 AGN. By using spectropolarimetry, we are able to indirectly view the inner regions of the core as seen by the scatterers. Thus, it is possible to place constraints on orientation-based models of the BLR by comparing the

spectra of both total and polarized light.

The degree of polarization as well as polarization angle variations across the broad Hα line almost certainly contain a wealth of encoded information regarding the structure and kinematics of both the BLR and scattering material. Despite this, few studies have been conducted regarding the spectropolarimetry of Seyfert 1 galaxies.

2 Spectropolarimetry

This work focuses on the analysis of spectropolarimetry observations. Spectropolarimetry is the study of the polarization characteristics of electromagnetic radiation as a function of wavelength.

In the most general sense, light can be described as a traveling transverse wave with both an electric field component and a magnetic field component. These two fields are arranged in such a fashion that they are always perpendicular to each other, and the direction that the light travels is perpendicular to both. For the purposes of spectropolarimetry, it is prudent to simply consider the orientation of the electric field (since the magnetic field can be described by the relationship between the electric field and the direction of the traveling light).

In thermal processes, light is produced in a way that causes its electric field vector to be randomly oriented. This light can become polarized – usually through scattering – if the electric field vectors of each ray become oriented in a non-random way. That is to say that polarized light is electromagnetic radiation with a preferential direction for the electric field vector. This polarization of the light is described through the Stokes Parameters.

2.1 Polarization of Electromagnetic Radiation

Suppose an electromagnetic wave with a frequency ω and a wavelength λ travels in the $\hat{z}$ direction. Again, we will describe this light exclusively through its propagation direction and its general electric field vector. Since the propagation direction and the electric field vector must be perpendicular at all points in space and time, the electric field is fully described by the sum of its $\hat{x}$ and $\hat{y}$ components:

$$\vec{E} = \vec{E_x} + \vec{E_y} \tag{3}$$

Generally speaking,

$$\vec{E_x} = E_{x0} \cos{(kx - \omega t)} \hat{x} \tag{4}$$

$$\vec{E_y} = E_{y_0} \cos{(ky - \omega t + \phi)} \hat{y} \tag{5}$$

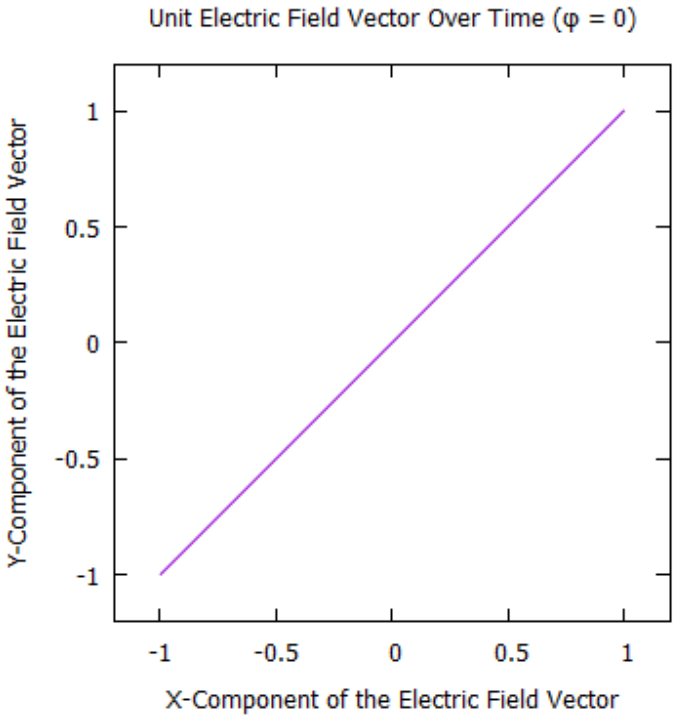

Figure 2: The $\hat{x}$ and $\hat{y}$ components of a unit electric field vector for linearly polarized light.

Where

$$k = \frac{\lambda}{2\pi} : \text{Wave Number}$$
$$E_{x0} : \text{Amplitude of } \vec{E}_x$$
$$E_{y_0} : \text{Amplitude of } \vec{E}_y$$
$$\phi : \text{Phase difference between the vectors}$$

As stated earlier, polarized light is electromagnetic radiation with a non-random orientation of the electric field vector. In the context of these equations that simply means that the phase shift, ϕ, is constant. The value of ϕ determines the "type" of polarization.

The first of the three main types of polarization is linear polarization which occurs when the phase shift between the two components of the electric field is a multiple of π. That is to say that if $\phi = \pm n\pi$ for $n = 0, 1, 2, ...$ then the light is linearly polarized. The path the electric field vector traces in space is shown in figure 2.

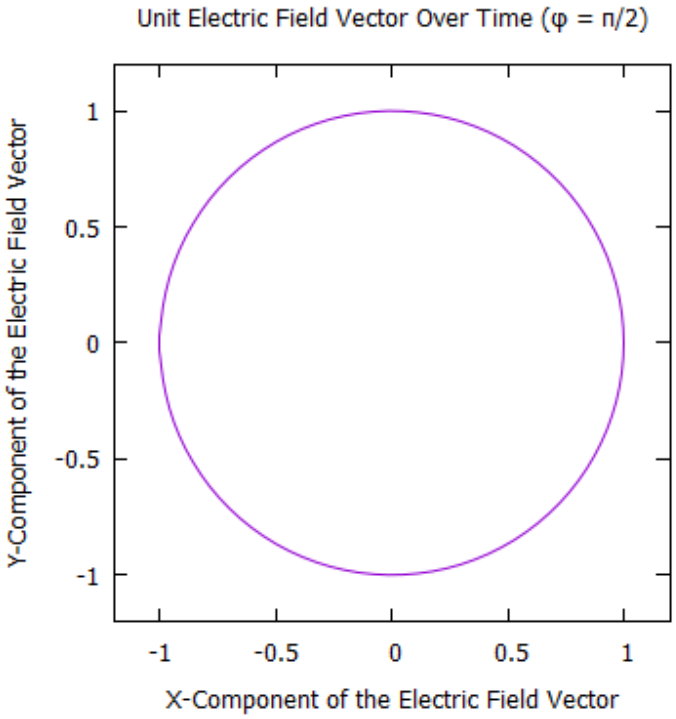

Figure 3: The $\hat{x}$ and $\hat{y}$ components of a unit electric field vector for circularly polarized light.

The second main type of polarization is circular polarization which occurs when the phase shift follows the form of $\phi = \pm n\frac{\pi}{2}$ for $n = 0, 1, 2, ...$ The path the electric field vector traces in space is shown in figure 3.

Phase shifts that do not fall into the two previously mentioned categories form the last major type of polarization: elliptical polarization. If polarized light is not fully linear polarized nor fully circularly polarized, it is – by default – elliptically polarized. The path the electric field vector traces in space is shown in figure 4.

2.2 The Stokes Parameters

In the general case of polarized light, we can define particular geometric quantities that describe the shape that the electric field vector traces in space. The visual representation of these parameters is shown in figure 5.

Through these parameters, we are able to establish a mathematical definition of the Stokes parameters. These values describe the degree of polarization and the polarization state of light and will be discussed in more detail later in this section. Using the geometric parameters shown in figure

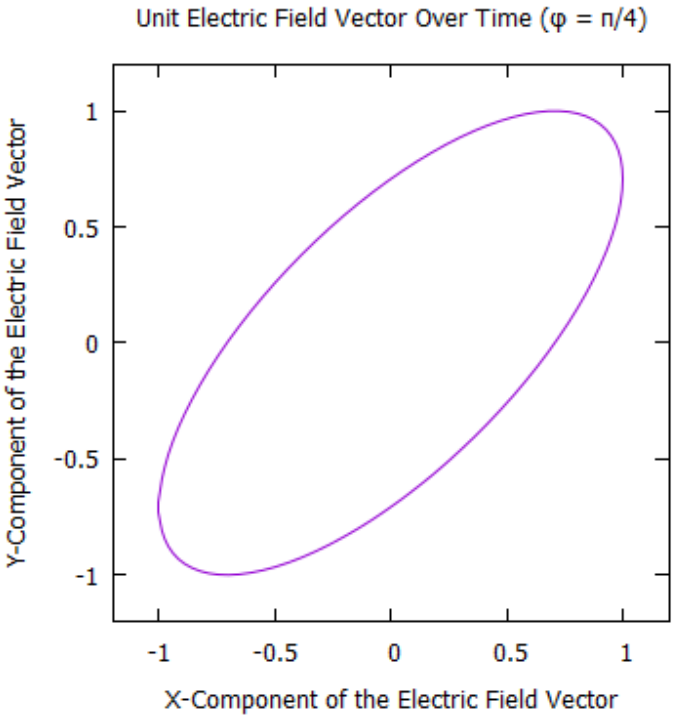

Figure 4: The $\hat{x}$ and $\hat{y}$ components of a unit electric field vector for elliptically polarized light.

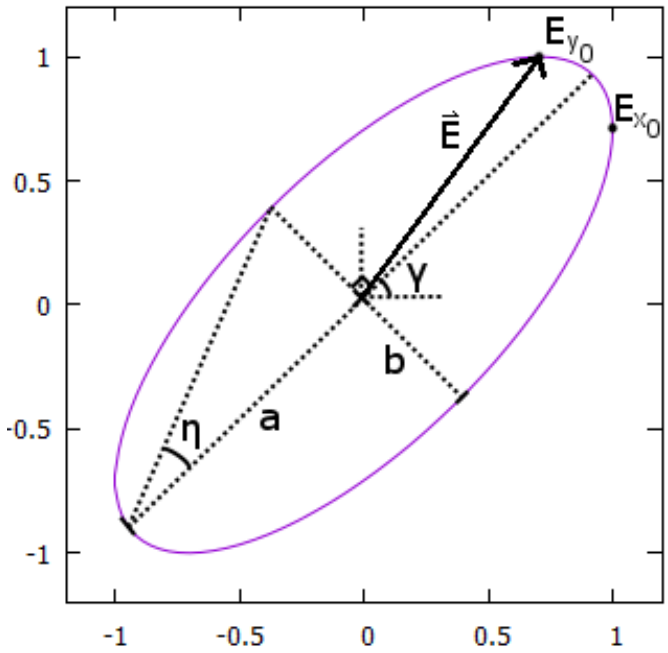

Figure 5: Geometric polarization parameters shown in the case of elliptical polarization.

5, the Stokes parameters are defined as (Rybicki & Lightman 1979)

$$I \equiv a^2 + b^2 \tag{6}$$
$$Q \equiv I\cos(2\eta)\cos(2\gamma) \tag{7}$$
$$U \equiv I\cos(2\eta)\sin(2\gamma) \tag{8}$$
$$V \equiv I\sin(2\eta) \tag{9}$$

The Stokes parameters may also be described in terms of the components of the electric field (Rybicki & Lightman 1979):

$$I = {E_{x0}}^2 + {E_{y_0}}^2 \tag{10}$$
$$Q = {E_{x0}}^2 - {E_{y_0}}^2 \tag{11}$$
$$U = 2E_{x0}E_{y_0}\cos(\phi) \tag{12}$$
$$V = 2E_{x0}E_{y_0}\sin(\phi) \tag{13}$$

While these mathematical forms are useful for calculating the Stokes parameters, they are not particularly illuminating. As such, they are often described as follows:

I : The total intensity of the light

Q : The difference in intensity between vertically linearly polarized light and horizontally polarized light ($I_{0^\circ} - I_{90^\circ}$)

U : The difference in intensity between linearly polarized light at $+45^\circ$ and -45° ($I_{45^\circ} - I_{-45^\circ}$)

V : The difference in intensity between right-handed circularly polarized light and left-handed circularly polarized light ($I_R - I_L$)

For the purposes of this work we will only be considering linearly polarized components of the light. Thus, it can be safely assumed that the last stokes parameter, V, will be zero.

Polarized light need not be completely polarized; it is possible for a series of rays to be partially polarized. For completely polarized light, the square of its total intensity will be exactly equal to the sum of the squares of the Stokes Q and Stokes U parameters:

$$I^2 = Q^2 + U^2 \tag{14}$$

If the light is not completely polarized, then the sum of the squares of Q and U are necessarily less than the square of the total intensity:

$$I^2 > Q^2 + U^2 \tag{15}$$

Light of any constant polarization state can be completely described by its stokes parameters which allows us to represent it as what's known as a Stokes vector. This quantity is simply each of the stokes parameters arranged as vector elements (Rybicki & Lightman 1979):

$$\vec{S} = \begin{bmatrix} I \\ Q \\ U \\ V \end{bmatrix} \tag{16}$$

When represented in this way, we can describe the sum of two incoherent rays as the sum of their Stokes vectors (and – by extension – their individual Stokes parameters):

$$\vec{S}_{Total} = \vec{S}_1 + \vec{S}_2 \tag{17}$$

Under this principal any given ray can be broken down into two component rays. Being interested in polarization, one could break them into a completely unpolarized ray and a completely polarized ray. Assuming the polarized constituent is linearly polarized,

$$\vec{S}_{Total} = \vec{S}_{Unpol} + \vec{S}_{Pol} \tag{18}$$

$$\vec{S}_{Total} = \begin{bmatrix} I_{Unpol} \\ 0 \\ 0 \\ 0 \end{bmatrix} + \begin{bmatrix} I_{Pol} \\ Q \\ U \\ 0 \end{bmatrix} \tag{19}$$

From this perspective it is clear that the total intensity of a given ray is a sum of its polarized intensity and its unpolarized intensity. That is to say

$$I = I_{Unpol} + I_{Pol} \tag{20}$$

With the light broken down in this manner, it is possible to describe two new quantities associated with the polarization state. The first is the percentage polarization, p. This quantity is described as the percentage of the total intensity that is made up of completely polarized light:

$$p = \frac{I_{Pol}}{I} \tag{21}$$

As stated earlier in equation 14, the square of the polarized intensity for completely polarized light is equal to the sum of the squares of the Stokes Q and U parameters. Thus,

$$\boxed{p = \frac{\sqrt{Q^2 + U^2}}{I}} \tag{22}$$

The second of these derived quantities is the polarization position angle, θ. This angle describes the angular orientation of the electric field vector as measured from North. To calculate this value, we can return to our very first definitions of the Stokes Q and U parameters (equations 7 and 8). In these definitions, the second of the two angles, initially referred to as γ, is equivalent to the polarization position angle. Furthermore, we are able to stipulate that the value of η must be zero since we are only concerned with polarized light. As such, we can re-write the equations for each of the Stokes parameters:

$$Q = I\cos(2\theta) \tag{23}$$

$$U = I\sin(2\theta) \tag{24}$$

From these two equations, the functional form of θ can be derived:

$$\boxed{\theta = \frac{1}{2}\tan^{-1}\left(\frac{U}{Q}\right)} \tag{25}$$

In order to calculate I, Q, and U from real sources, we need to be able to look at the polarization characteristics at a few different polarization position angles, namely $\theta = \{0°, 45°, 90°, 135°\}$. Doing this requires use of a device aptly named a spectropolarimeter.

2.3 Spectropolarimeters

As stated at the end of the previous section, a spectropolarimeter is a device that can measure the degree of polarization at four critical angles as a function of wavelength. These devices aim to provide spectrally resolved information regarding a source's polarization characteristics. In general, a spectropolarimeter consists of five major components:

- Half-wave plate
- Slit and/or dekker
- Beam splitter
- Spectrograph
- Detector

These components are arranged along the optical path in order. The schematic for this type of generic system is shown in figure 6.

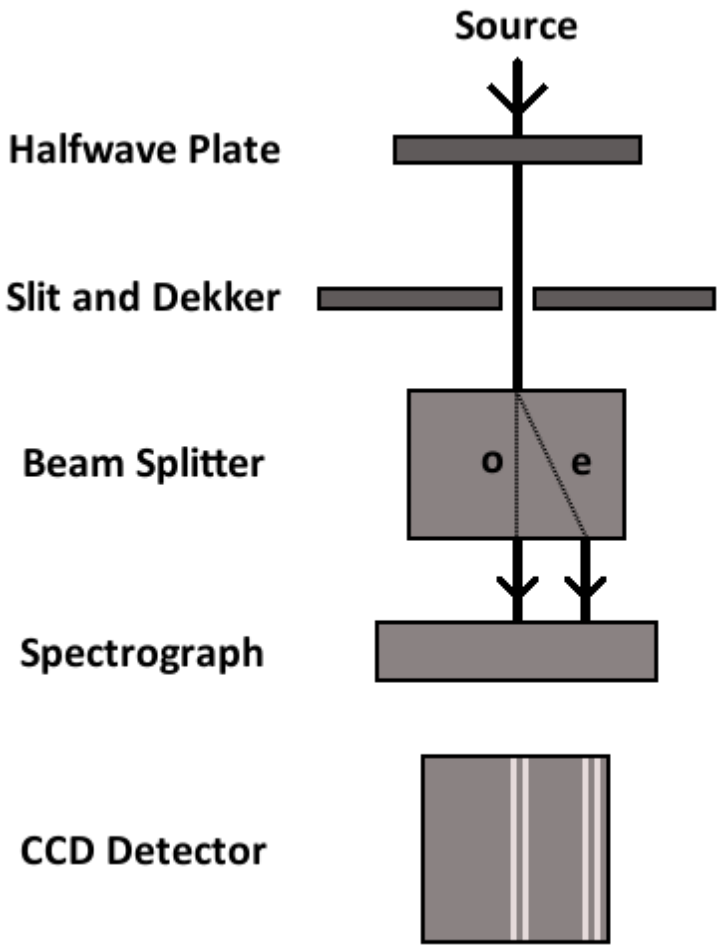

Figure 6: A schematic diagram of a generic spectropolarimeter. The shown detections on the CCD are (from left to right) the ordinary (o) and extraordinary (e) spectra of the object and the o and e spectra of the sky.

2.3.1 Half-wave Plate

A half-wave plate is a type of optical device made of birefringent material known as a retarder. The retarder splits the transmitted light into two orthogonal components. Each of these travel through the material at a different speed. This difference in propagation speed induces a phase shift of π between the component rays which, as a result, rotates the polarization plane of the incoming light. These orthogonal components then recombine as they exit the halfwave plate.

These devices are placed at the front of the optical path in order to rotate the polarization plane without rotating the entire device. Such a process is mechanically difficult and may cause issues involving the placement of the aperture in the sky. Using this system, the full set of critical angles can be analyzed by rotating the half-wave plate by angles of $0°$, $22.5°$, $45°$, and $67.5°$ (since rotating the half-wave plate through an angle of ψ causes a 2ψ rotation of the incident ray's electric field).

2.3.2 Slit and Dekker

The slit portion of the slit and dekker is a simple slit designed to act as an aperture for the object in question. Within this slit is a dekker: a series of smaller slits designed to separate the object and sky measurements. One slit of this device contains the object (in the case of a point source) while the others provide measurements on the background. This setup avoids overlap of sky and source detections caused by the splitting of the ordinary and extraordinary rays downstream.

2.3.3 Beam Splitter

After the slit and dekker, incoming rays pass through a linearly polarizing material which acts as a beam splitter. This device, much like the half-wave plate, splits incident light into two orthogonal components that are each 100% linearly polarized: the ordinary (o) and extraordinary (e) rays. Unlike the half-wave plate, these rays do not recombine and instead emerge from the plate separated by a small angle. The relative intensities of these rays are dependent on the polarization state of the incident ray.

2.3.4 Spectrograph

The last device before the CCD camera is designed to split each o and e ray from the slit and dekker into their component wavelengths. A reflective ruled diffraction grating is used to separate the light into separate wavelength components. These devices cause light diffract and then reflect off of the surface of the grating, leading to an angular separation between the wavelengths of the light. These spectra are then transmitted to the detector.

2.3.5 CCD

At the end of the light's journey, it must be collected by some sort of detecting device. In most cases, this device is a CCD. The resulting measurement will contain pairs of o and e spectra for both the object and the background.

2.3.6 Extraction of Stokes Parameters

The basic data product of recorded by the CCD camera is an image which contains the o and e spectra for both the source and background apertures. These images are first processed using the standard techniques for reducing CCD images containing spectroscopic data, including de-biasing, flat-fielding, extraction of 1-d flux spectra, as well as wavelength and flux calibration.

Afterwards, the Stokes parameters can be calculated using the RATIO method (Smith et al. 2002). First, atmospheric variations throughout the observations can be removed by taking the intensity ratios of the o and e rays (i_o and i_e respectively) at each half-wave plate orientation:

$$I_0 = \frac{i_{e,0}}{i_{o,0}} \tag{26}$$

$$I_{22.5} = \frac{i_{e,22.5}}{i_{o,22.5}} \tag{27}$$

$$I_{45} = \frac{i_{e,45}}{i_{o,45}} \tag{28}$$

$$I_{67.5} = \frac{i_{e,67.5}}{i_{o,67.5}} \tag{29}$$

Since the objects explored in this study are of relatively low polarization, these ratios tend towards

unity.

With atmospheric variations removed, the largest remaining portion of non-source polarization is that of the instrument itself. Since the instrumental polarization should not be orientation-dependent, another set of ratios can be formed which are used to remove the instrumental system gain and effects of the observational conditions:

$$R_Q{}^2 = \frac{I_{22.5}}{I_{67.5}} \tag{30}$$

$$R_U{}^2 = \frac{I_0}{I_{45}} \tag{31}$$

The normalized Stokes parameters, $\bar{Q}$ and $\bar{U}$ can be calculated using the above ratios:

$$\bar{Q} = \frac{R_Q - 1}{R_Q + 1} \tag{32}$$

$$\bar{U} = \frac{R_U - 1}{R_U + 1} \tag{33}$$

The total intensity, the Stokes I of the source, can then be calculated by taking the average intensities of the o and e rays across each of the 4 CCD frames.

2.4 Polarization Mechanisms

Light can become polarized as a result of many physical mechanisms. In the case of astronomical sources though, there are three main methods with which light can become polarized: scattering, dichroic absorption, and synchrotron radiation.

2.4.1 Scattering

Scattering of light occurs when the rays are redirected from their original path due to interaction with matter: the absorption and re-emission of the radiation by material particles. In AGN these particles tend to be dust or free electrons surrounding the emission disk.

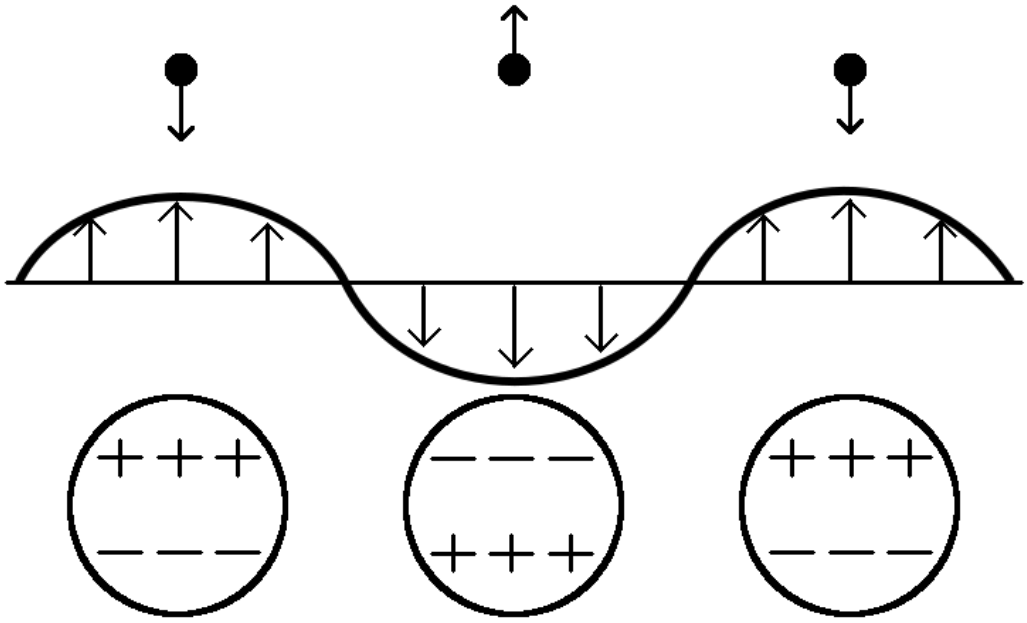

Figure 7: The effect of an incident electric field (denoted by the sinusoid inlaid with arrows) on the two main particles associated with scattering. Shown above the sinusoid is the instantaneous acceleration of a point charge (in this case an electron). Shown below the sinusoid is the redistribution of charge in a neutral particle.

Scattering of light is described in its most general form by Mie scattering theory. If the wavelength of the radiation is much larger than the scattering cross-section of the particle, then Rayleigh scattering occurs. This particular case covers scattering of light from the emission disk by free electrons in the equatorial scattering region (see chapter 3).

When the electric field component of light interacts with matter, it causes the charged particles within the material to accelerate due to the electrical Lorentz force:

$$\vec{a} = \frac{q}{m}\vec{E}$$

This charge-based acceleration redistributes the charge throughout the particle in the case of dust grains or simply accelerates a charged particle in a sinusoidal pattern in the case of a free electron (as shown in figure 7). This redistribution of charge occurs at a frequency equal to that of the incident radiation. Since accelerating charges emit electromagnetic radiation, these perturbed charges emit light of the same frequency as the incident light.

As alluded to earlier, the scattering cross-section of a particle is important to the interaction it has with incident light. For an electron, the scattering cross section is (Rybicki & Lightman 1979)

$$\sigma_e = \frac{8\pi}{3}\left(\frac{{q_e}^2}{m_e c^2}\right)^2 \tag{34}$$

whereas for dust particles (in the Rayleigh scattering regime) it is

$$\sigma_d = \frac{8\pi}{3}\left(\frac{2\pi}{\lambda}\right)^4 |\alpha|^2 \tag{35}$$

Where α is the polarizability of the medium. The most important distinction between these two cross-sections is that dust scattering has a strong inverse relationship with wavelength whereas electron scattering is independent of wavelength. This shows that dust preferentially scatters shorter wavelength blue light.

Scattered light has intensity and polarization characteristics related to the scattering angle, χ. For the case of Rayleigh scattering, the intensity is described by

$$I = \frac{[1-\cos^2(\chi)]k^4|\alpha|^2}{2r^2} I_0 \tag{36}$$

where

I_0 : Intensity of the incident ray

r : Distance from the scattering element to the observer

$k = \dfrac{2\pi}{\lambda}$: Wavenumber

And the degree of polarization is given by (Rybicki & Lightman 1979)

$$p = \frac{1-\cos^2(\chi)}{1+\cos^2(\chi)} \tag{37}$$

2.4.2 Dichroic Absorption

Dichroism refers to the preferential absorption of light at certain polarization position angles. Polaroid sunglasses are an every-day example of this phenomenon, though they use stretched polymers rather than dust grains to produce the effect.

This process results from interactions between electromagnetic radiation and non-spherical dust grains in an external magnetic field. The longer axis of these particles tend to align perpendicularly to the magnetic field they are within. These particles also preferentially absorb the polarization component of light aligned with their longer axis, transmitting a surviving net polarization. As a result, the transmitted light has a net polarization position angle parallel to the magnetic field (since the perpendicular component was preferentially absorbed).

It has been shown that the degree of polarization due to this effect is related to the reddening of the absorbing dust, as measured by the color excess (Serkowski, Mathewson, & Ford 1975). The induced percentage polarization is approximately three times the B-V color excess while the maximum possible value is about nine times the B-V color excess.

2.4.3 Synchrotron Radiation

When electrons travel through a magnetic field, they experience an inwards acceleration due to the magnetic Lorentz force law:

$$\vec{a} = \frac{q}{m}\left(\vec{v} \times \vec{B}\right) \tag{38}$$

Assuming that the velocity of the particle is neither completely parallel nor completely perpendicular to the magnetic field, it will travel in a helical fashion. The inward acceleration that causes it to do so will make the charged particle emit electromagnetic radiation. The intensity of this radiation is largely unimportant when dealing with non-relativistic velocities (which result in cyclotron radiation), but in AGN the assumption that the particles are non-relativistic does not hold.

When velocities approach the speed of light, it is sometimes more useful to refer to them by their Lorentz factors rather than their actual velocities. This value is related to an object's speed:

$$\gamma = \frac{1}{\sqrt{1 - \frac{|\vec{v}|^2}{c^2}}} \tag{39}$$

Where $|\vec{v}|$ is the speed of the object and c is the speed of light.

When charged particles emit electromagnetic radiation whilst traveling at these high speeds, the resulting light is beamed in a cone with an axis of symmetry along the particle's velocity (Rybicki & Lightman 1979). This cone narrows as the speed increases; the half opening angle ($\frac{1}{2}\theta$) is inversely proportional to the Lorentz factor (as defined in equation 39):

$$\frac{1}{2}\theta = \frac{1}{\gamma} \tag{40}$$

This anisotropic emission of light is known as relativistic beaming. In the case of synchrotron radiation, this effect causes a rotating conical beam of emission which has an axis of symmetry perpendicular to the magnetic field (Rybicki & Lightman 1979) (as shown in figure 8).

Any light that travels directly towards the observer is linearly polarized in an orientation perpendicular to that of the external magnetic field (Rybicki & Lightman 1979). Since the emission region is a cone though, not all of the light received will be from electrons traveling directly towards the observer. These other angles will produce elliptically polarized light. In theory though, the polarization state of the rays at equivalent angles above and below the cone's axis of symmetry will be equal but opposite. If there are enough free electrons emitting light in this fashion, the elliptically polarized rays will cause cancellation (Rybicki & Lightman 1979).

In total, a synchrotron process will result in linearly polarized light at a position angle perpendicular to that of the external magnetic field. The theoretical limit of this process is approximately 75% polarization (Rybicki & Lightman 1979). Despite this, the light generally reaches us with a polarization percentage of only about 10% due to the fact that light which is not directly in-line with the emission cone is circularly polarized rather than linearly polarized. It is important to note that in the cases of scattering and dichroic absorption, the light is polarized due to secondary processing by something other than the source. Synchrotron radiation, on the other hand, is a source of intrinsically polarized light.

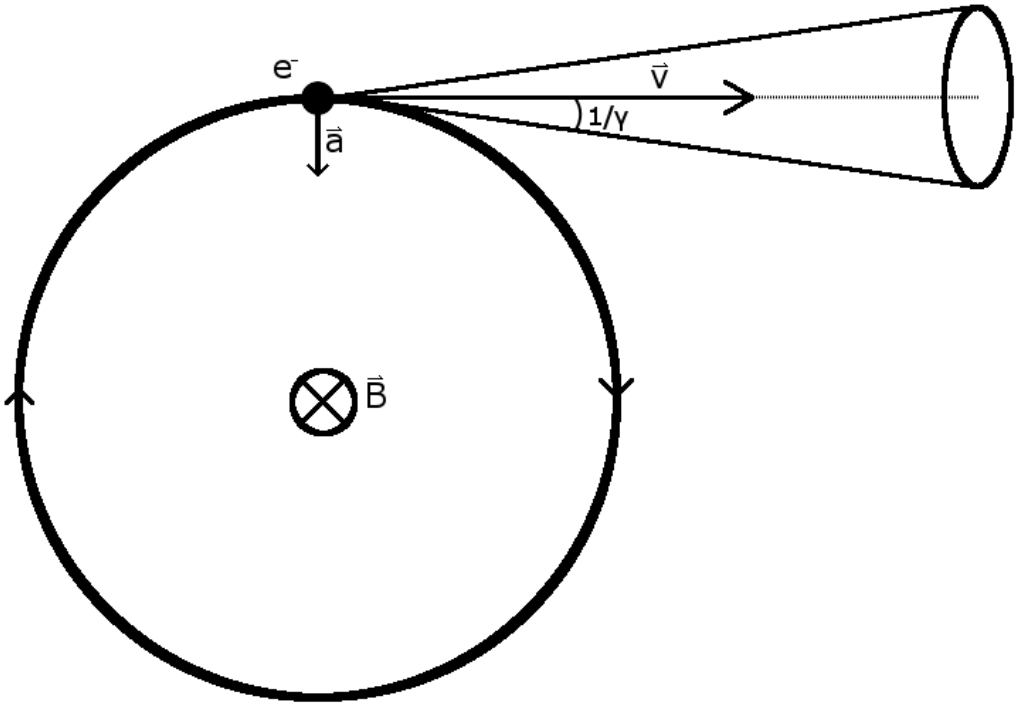

Figure 8: A schematic of synchrotron radiation emitted by a relativistic electron under the influence of a magnetic field. The tangential velocity of the electron is denoted by $\vec{v}$ and is completely in the plane of the page. The magnetic field is denoted by $\vec{B}$ and is presumed normal to the plane of the page. The acceleration on the electron due to the magnetic field (shown by $\vec{a}$) is thus pointed towards the center of the drawn orbit. The cone is displayed in the upper portion of the diagram includes all possible emission paths for the electromagnetic radiation produced by this process. It has a half-opening angle of $\frac{1}{\gamma}$ and has an axis of symmetry along the electron's instantaneous velocity.

3 Two-Component Scattering in AGN

It is believed that scattering is the dominant source of polarization in AGN. In general, AGN are thought to contain two main scattering structures: the equatorial scattering region and the polar scattering region. Depending on the orientation of the object, the characteristics of the polarized light will differ, with particular signatures being indicative of either equatorial or polar domination.

The discussion that follows is largely based on the predictions made by Smith et al. (2005).

3.1 The Two-Component Scattering Model

The two-component scattering model is primarily defined by the presence of two distinct scattering geometries within AGN. The first of these is the equatorial scattering region which consists of a thick ring of co-rotating scatterers and is oriented co-axially with both the AGN emission disk and the torus (see section 1.5.1). The second is the polar scattering region, defined by scatterers arranged in a conical frustum along the rotational axis of the AGN. A visual representation of these geometries can be seen in figure 9.

Depending on the orientation of the AGN, the observer will detect a polarization spectrum which is dominated by either equatorial or polar scattering (see sections 3.4 and 3.5). For example, an AGN observed edge-on would have both the emission disk and equatorial scattering region blocked by the torus. As a result, the only significant emission that will reach the observer is that of the polar-scattered light. We would consider this object to be a "polar-class" or "polar-dominated" object.

On the other hand, an AGN may be oriented in such a way that the observer's view of the equatorial scattering region is not obscured. In this case, we could expect to see aspects of both scattering components, though it is more likely that the equatorial signatures would drown out those of the polar region. Thus, most AGN are able to be classified as either equatorial- or polar-class objects.

3.2 Basic Equatorial Scattering Geometry

The basic geometry for a simple equatorial scattering model consists of three major structures: a continuum source, a rotating emission disk, and a nearby co-planar ring (or disk) of scattering elements. The system is in turn surrounded by a circum-nuclear torus in accordance with the

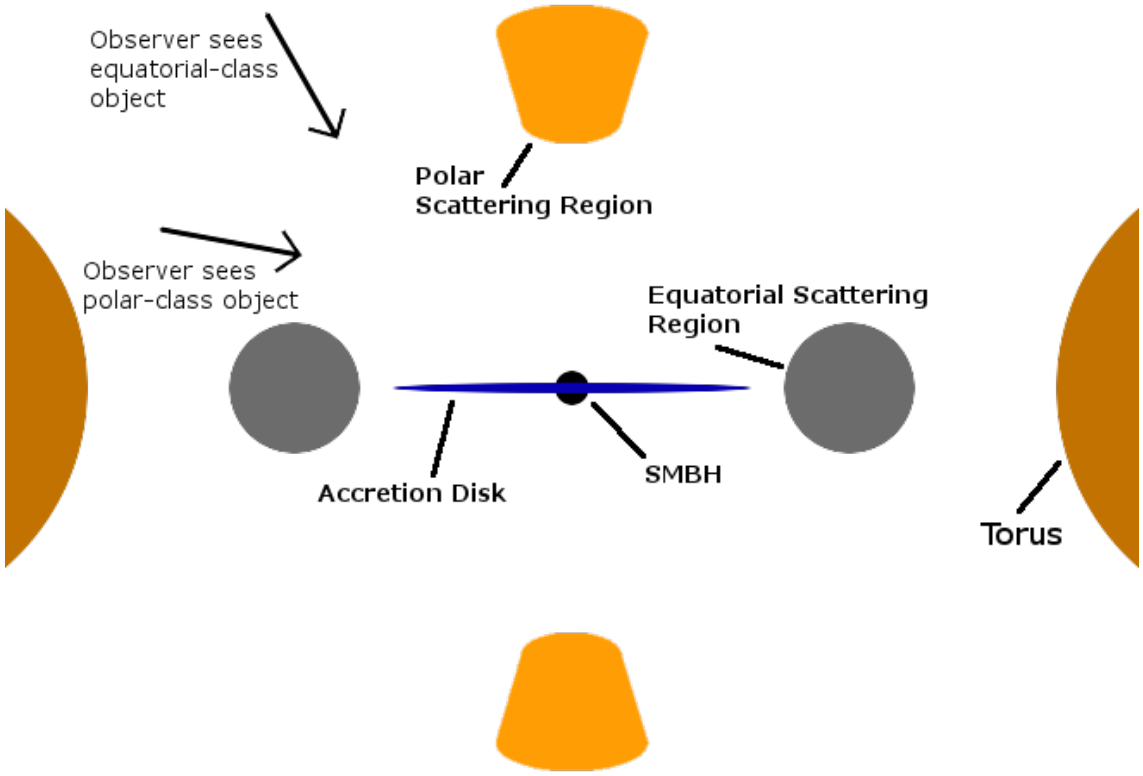

Figure 9: A diagram of the two-component scattering model. The two gray circles represent a co-axial thick disk surrounding the central emission source (the equatorial scattering region), while the two orange conical frustums represent the polar scattering region. The observer lines-of-sight in the upper left are examples of different viewing angles which are thought to lead to particular signatures in polarized spectra (see sections 3.4 and 3.5).

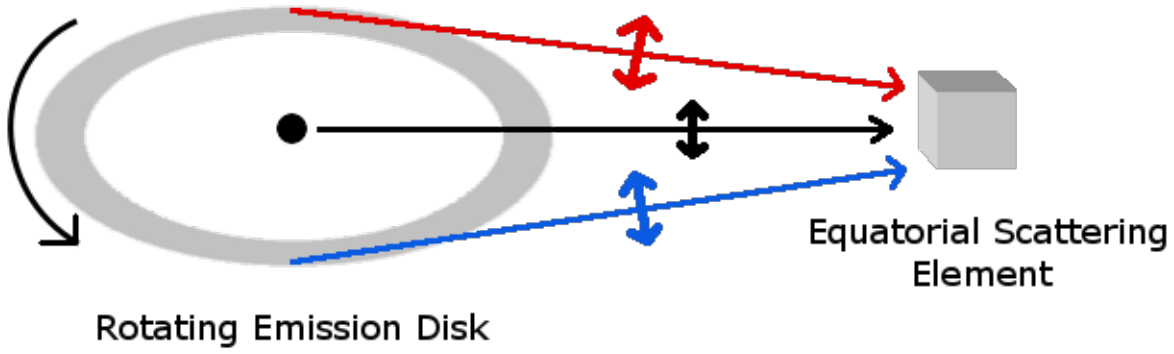

Figure 10: A schematic of the basic equatorial scattering geometry. The axis of rotation for this system is arbitrarily inclined from the observer's line of sight (assumed to be perpendicular to the page). The singular scattering element is but one piece of a larger ring which is co-planar with the rotating emission disk. The thin lines pointing from the emission disk to the scattering element represent (from top to bottom) redshifted emission, source emission, and blueshifted emission. The thick, double-headed lines on each of these thinner lines represent the polarization vectors as seen by the observer. (Based on figures from Smith et al. (2005).)

Seyfert unification scheme (see section 1.5). Each of these structures are assumed to lie within the same equatorial plane and they are thus coaxial. This system axis can have an arbitrary inclination to the observer's line of sight which affects the observed characteristics; we will discuss this further in section 3.3.1.

For simplicity, let us first consider the case of a single scattering element within the equatorial plane. Light from the continuum source, as well as that from the rotating emission disk, is emitted isotropically. A fraction of this light is then scattered and re-directed to the observer via interactions with the equatorial scattering element. This newly-directed light finds itself (at least partially) linearly polarized with a polarization vector perpendicular to the plane containing the incident and scattered rays (which is known as the scattering plane). A schematic diagram of this system is shown in figure 10.

In the case of the central source continuum, this polarization is completely linear and has a polarization vector parallel (in projection) to the system axis. On the other hand, emission from the rotating disk is in general only partially linearly polarized. This is due to the fact that the scattering plane is tilted relative to the continuum emission plane, resulting in elliptical polarization. On either extreme edge of the disk – the locations of maximal Doppler shift with respect to the scattering element – the polarization position angle (PA) is equally but oppositely offset from the system axis due to the symmetry of the disk. In other words, the PA of the maximally redshifted light will be

offset from the continuum PA by the same magnitude as that of the maximally blueshifted light but with the opposite sign. The changing orientation of the scattering plane (with respect to the observer's line of sight) leads to the rotation of the PA across a given line profile which is centered on the continuum PA.

In general, this PA "swing" is still present when the geometry is scaled up to a complete co-planar ring of scatterers. While it is true that in the case of a face-on disk (as we will discuss further in section 3.3.1) circular symmetry will cause cancellation of the polarization vectors, inclination of the disk creates a non-symmetric polarization across the line profile. Despite this, those along the major axis will produce more polarized light post-scattering due to their larger scattering angle. This effect breaks the symmetry present in a face-on system and leads to a PA swing.

In the case of the scattering ring, a PA profile will be produced by each element of the scattering region individually. The structure of these PA spectra will be equivalent in shape and central wavelength, but will be offset from the continuum PA by various values between 0 and 90 degrees. In figure 11, we can see that this offset in PA occurs due to geometric effects.

Looking more closely at four specific scattering clumps within the ring, we can see how the individual PA spectra differ. Elements 1 and 2 are located in positions such that the central polarization vector from the central continuum source will be parallel to the system axis in projection. Due to this, their offset from the continuum PA will be zero. Element 3 is located such that its central polarization vector will appear perpendicular to the system axis, leading to an offset of 90 degrees. Finally, element 4 finds itself an arbitrary angle from the axis formed by elements 1 and 2. This location will produce a central polarization vector offset by the same arbitrary value. In other words, an element θ degrees from the major axis will have a PA which varies about θ.

This model also predicts strong variations in polarization percentage across the spectrum due to the way that the scattering elements "see" the emission disk. Light from the central rotating emission disk can only be directly observed if there is a line of sight to the observer which is not blocked by the obscuring torus. Thus, direct observations of the central emission region only occur when the disk is not edge-on. The scattering elements, on the other hand, always observe this disk in an edge-on orientation (since they are co-planar with the emission disk). As a result, the scattering elements will always "see" the maximal line-of-sight velocity (v_0), while that seen by the observer will be lower due to the inclination:

$$v = v_0 \sin(i) \tag{41}$$

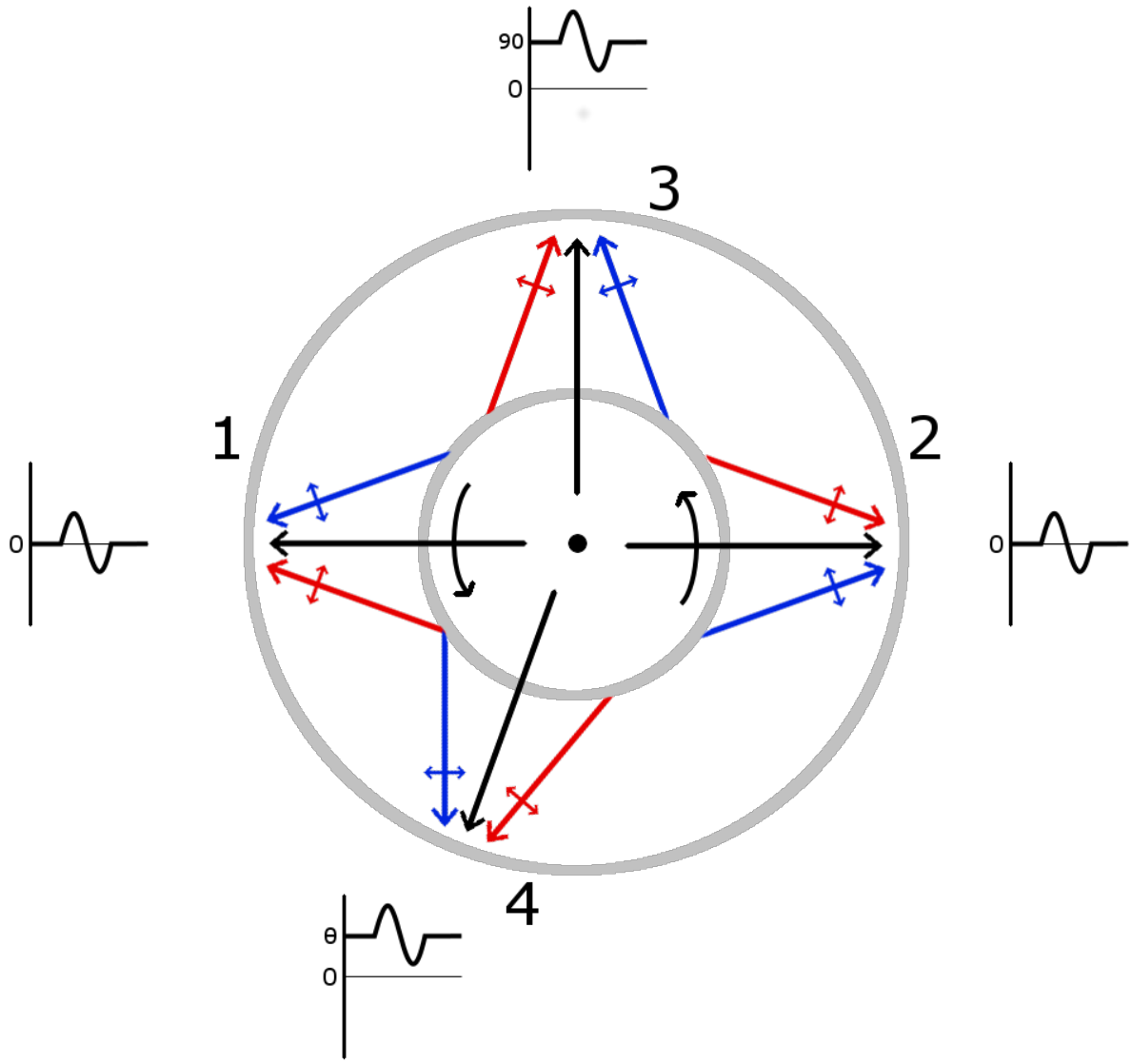

Figure 11: A schematic displaying the affect of orientation on the average observed PA in scattered light. Scattering elements near locations 1 and 2 will display a near-zero average PA due to their polarization vectors' alignment with the system axis (in projection). The opposite is true for those near location 3 (or 180 degrees offset from this location), which have polarization vectors perpendicular to the system axis. In general, a scattering element located some angle, θ, from region 1 or 2 will have an average PA of θ. (Based on figures from Smith et al. (2005).)

Since equatorial-class objects are expected to be viewed from an orientation which has a line of sight to the central region, the observed line-of-sight velocity will be significantly lower than maximal. This means that the line profile of the scattered, polarized light is broader than that of the direct, unpolarized light. Due to this dichotomy, we expect to observe an increase in polarization percentage in the wings of the line profile and a characteristic dip in the center.

3.3 Effects of Various Parameters on PA Swing

The PA spectrum caused by these scattering rings can vary between objects due to a multitude of factors. Thanks to these differences (alongside other measurements), the PA swing of objects can tell us a good deal about certain parameters of interest. For the purposes of this study, we will focus primarily on two of these parameters: orientation of the system and distance between the emission and scattering rings.

3.3.1 Orientation

The orientation of these systems is twofold, namely the offset of the system axis from north in the sky and the inclination of the disk. The prior simply causes the continuum PA to be shifted (as the PA is measured from north) but does not have an effect on the structure of the PA spectrum. The inclination, on the other hand, will have an observable effect on the PA swing.

To understand this concept, let us consider three separate systems: one of a high inclination (nearly face-on), another of intermediate inclination, and one of a low inclination (nearly edge-on). A depiction of these systems can be seen in figure 12. At high inclinations (but not completely face-on), the maximally redshifted and maximally blueshifted light have very different PAs due to the projected path they take from the emission disk. This causes a large PA swing across the line profile. It is important to note that in the case of a perfectly face-on disk, the polarization would completely cancel due to circular symmetry. As the inclination decreases, the difference in PA across the line decreases as well. This is due to the lessening difference in the projected paths taken by each maximally shifted line. In the case of an edge-on disk, there is no PA difference across the line and thus the PA swing approaches zero.

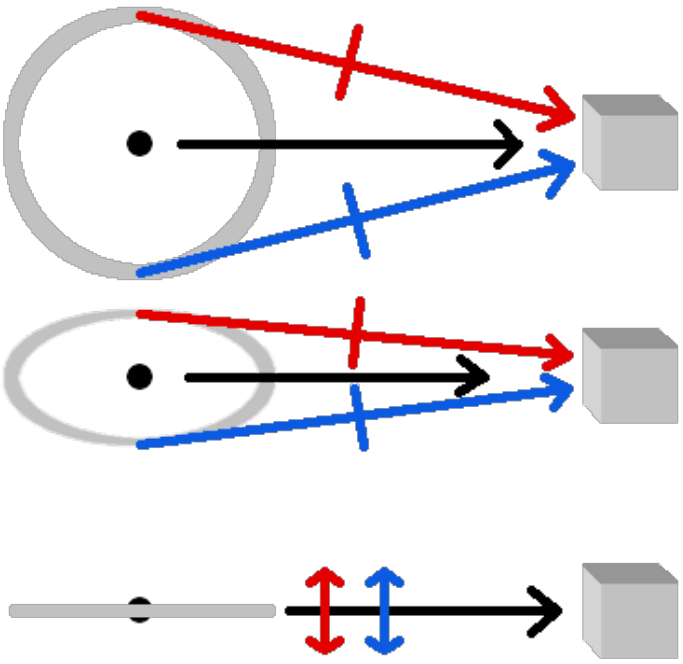

Figure 12: A schematic of three different object inclinations. The observer's line of sight for these systems is assumed to be perpendicular to the page. The red and blue arrows extending from the emission disk to the scattering elements represent the maximally redshifted and blueshifted portions of the disk while the black arrow is the continuum flux. The lines perpendicular to these lines show the PA of their respective arrow. (Based on figures from Smith et al. (2005).)

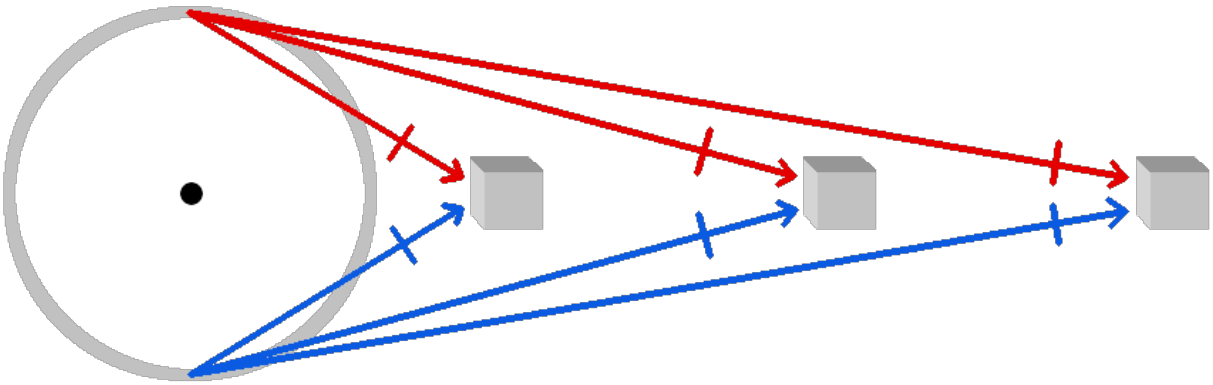

Figure 13: A schematic displaying three different distances from an emission disk to a scattering ring. The observer's line of sight for these systems is assumed to be perpendicular to the page. The red and blue arrows extending from the emission disk to the scattering elements represent the maximally redshifted and blueshifted portions of the disk while the black arrow is the continuum flux. The lines perpendicular to these lines show the PA of their respective arrow. (Based on figures from Smith et al. (2005).)

3.3.2 Distance Between Emission and Scattering Disks

The distance between the emission and scattering disks causes a similar effect in the value of the PA swing to system orientation. Let us consider another three systems, each with a different distance from an arbitrarily inclined emission disk to a similarly inclined scattering ring. A graphical depiction of these systems is shown in figure 13. At small separations, there is a large difference between the PAs of the maximally redshifted light and the maximally blueshifted light. This leads to a high PA swing at low separation distances. As this distance increases, the projected path of these rays converge and cause the total PA swing across the line to decrease.

3.4 Spectral Signatures of Equatorial-Class Objects

As described in section 3.1, we would expect equatorial dominated objects to be those observed from a more face-on orientation. Because of this, we would expect to see a low percentage polarization of the Hα core since the unpolarized light from the emission disk is not blocked by the torus. Furthermore, some equatorial-class objects would display double-peaked spectra due to the Doppler shifts present across the emission disk.

The equatorial scattering region – being co-axial with the emission disk – will "see" the unpolarized emission of the AGN edge-on. Because of this, the scattered light will display the largest

possible difference in polarization position angle across the Hα profile. As a result, equatorial-class objects are expected to have high PA swings across the profile.

An example of these properties can be seen in the polarization spectrum of Mrk 6 (E2) (figure 14).

3.5 Spectral Signatures of Polar-Class Objects

Section 3.1 tells us that we should expect polar dominated objects to be those observed from an edge-on orientation. As a result, we would expect to see a high percentage polarization of the Hα core since the unpolarized light from the emission disk is obscured by the torus. Furthermore, we would expect pronounced narrow lines to appear in the polarization spectra of these AGN, as the NLR is also blocked by the torus.

The polar scattering region is along the axis of rotation and will "see" the unpolarized emission of the AGN face-on. As a result, the scattered light will display little to no difference in polarization position angle across the Hα profile. Thus, polar-class objects are expected to have low PA swings across the profile.

An example of these properties can be seen in the polarization spectrum of F 51 (figure 15).

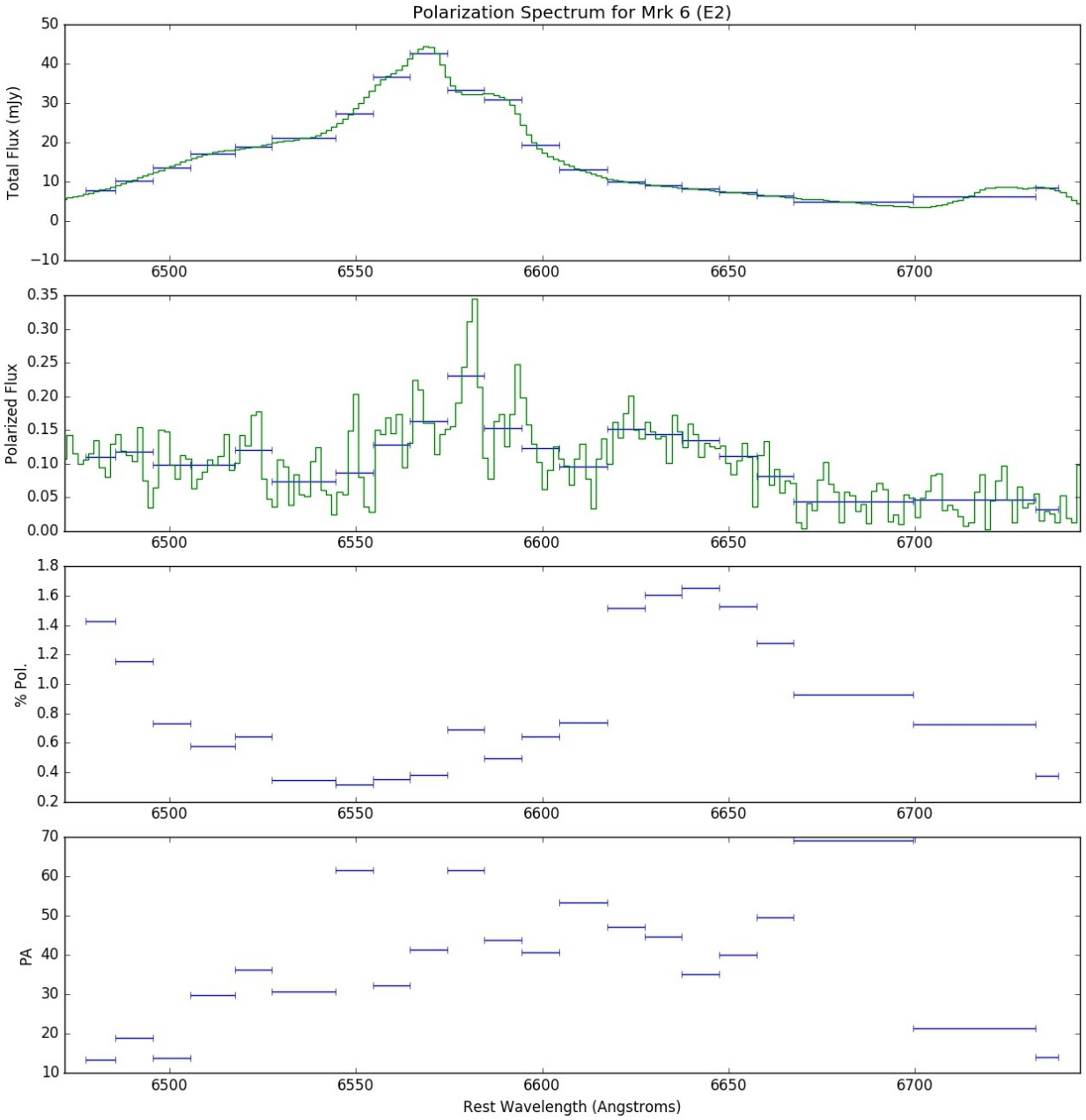

Figure 14: The polarization spectrum of Mrk 6 (E2). This object's spectra shows many properties indicative of equatorial scattering. Percentage polarization drops significantly in the broad Hα region, the polarized flux displays a double peak, and there is a large swing in PA values.

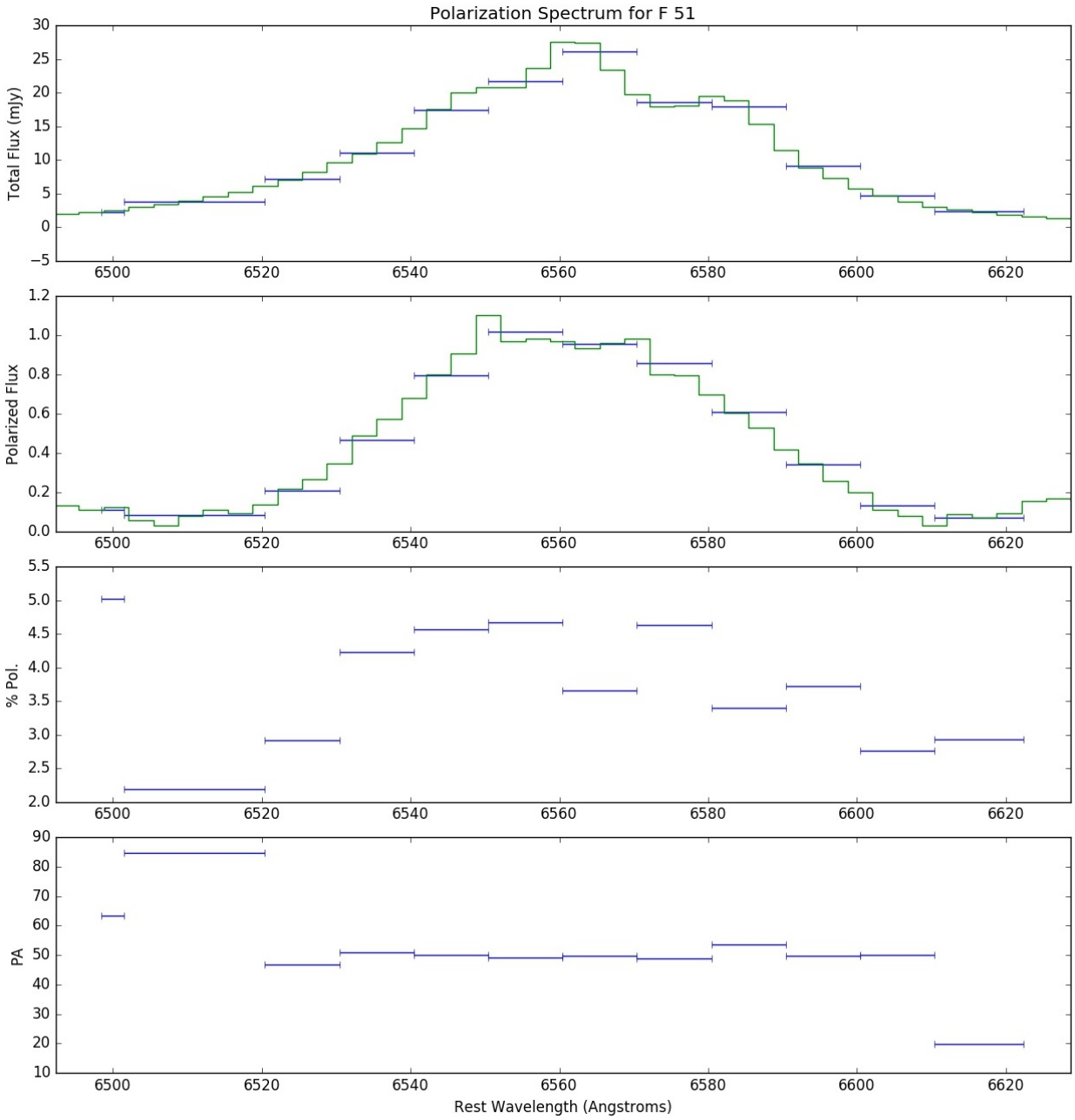

Figure 15: The polarization spectrum of F 51. This object's spectra shows many properties indicative of polar scattering. Percentage polarization rises significantly in the broad Hα region and there is no large swing in PA values (the values far from the median PA on the edges of the continuum are a result of low signal-to-noise).

4 Data Analysis

4.1 Observational Data

The observational data for this study were obtained through observations with the 4.2m William Herschel Telescope (WHT) at the Observatorio del Roque de los Muchachos, and the 3.9 m Anglo-Australian Telescope (AAT) at the Anglo-Australian Observatory. The WHT observations utilized the red arm of the ISIS dual-beam spectrograph in conjunction with the R316R grating. The AAT observations utilized the Royal Greenwich Observatory spectrograph in con-junction with the 270R grating. A list of the telescope, instrument, and grating used to observe each object is given in table 1.

The sample was selected from the Veron Catalog of Quasars and AGN[1] and includes objects classified as broad-line (Seyfert 1; see section 1.2.1.1) AGN which are bright enough to provide high signal-to-noise spectropolarimetry with integration times of less than 2 hours (those with V magnitudes less than $\sim$15 or 16).

Prior to their analysis in this study (described at length in chapter 4), the data were processed using standard methods. Standard CCD reductions were performed and each spectra was background subtracted, wavelength calibrated, and flux calibrated prior to generation of the Stokes spectra. Details of this reduction are given in Smith et al. (2002).

Object	Telescope	Observation Date
2E 4066	WHT	Oct. 1998
Akn 120 E1	WHT	Sep. 1998
Akn 120 E2	WHT	Oct. 1998
Akn 564	WHT	Sep. 1998
Akn 564 Apr03	WHT	June 2003
ESO 12-21	AAT	Aug. 1997
ESO 113-45	AAT	Aug. 1997
ESO 141-35	AAT	May 1997
F 51	AAT	Apr. 1997
I zw 1 (Aug06)	WHT	Aug. 2006
I zw 1 (E1)	WHT	Sep. 1998

[1] https://heasarc.gsfc.nasa.gov/W3Browse/all/veroncat.html

I zw 1 (E2)	WHT	Oct. 1998
I zw 1 (Sep02)	WHT	Sep. 2002
IC 3599 (Apr03)	WHT	Apr. 2003
IRAS 17002+5153	WHT	June 2003
KUG 1031 (Apr03)	WHT	Apr. 2003
Mrk 6 E1	WHT	Feb. 1997
Mrk 6 E2	WHT	Oct. 1998
Mrk 279	WHT	Feb. 1997
Mrk 290	WHT	June 1999
Mrk 304	AAT	May 1997
Mrk 335	WHT	Oct. 1998
Mrk 478 Apr03	WHT	Apr. 2003
Mrk 478 Jun03	WHT	June 2003
Mrk 486	WHT	Apr. 2003
Mrk 486 (Apr03)	WHT	Apr. 2003
Mrk 507	WHT	Apr. 2003
Mrk 509 E1	AAT	Aug. 1996
Mrk 509 E2	AAT	May. 1997
Mrk 509 E3	AAT	Aug. 1997
Mrk 590	WHT	Aug. 2003
Mrk 705	WHT	Feb. 1997
Mrk 766	WHT	Apr. 2003
Mrk 766 (Apr03)	WHT	Apr. 2003
Mrk 841	AAT	May 1997
Mrk 871	AAT	May 1997
Mrk 876	WHT	June 1997
Mrk 915	AAT	Aug. 1997
Mrk 926	AAT	Aug. 1997
Mrk 1239	WHT	Apr. 2003
MS 1849.2-7832	AAT	Aug. 1997
NGC 985	AAT	Aug. 1996
NGC 3227	WHT	Apr. 2003
NGC 3516	WHT	Feb. 1997
NGC 3783	AAT	May 1997

NGC 4051	WHT	June 1999
NGC 4051 (Apr03)	WHT	Apr. 2003
NGC 4151 (Apr03)	WHT	Apr. 2003
NGC 4593 E1	WHT	Feb. 1997
NGC 4593 E2	AAT	May 1997
NGC 5548	WHT	June 1997
NGC 6104	WHT	June 1999
NGC 7213	AAT	May 1997
NGC 7469 (E1)	WHT	June 1997
NGC 7469 (E2)	AAT	Aug. 1997
NGC 7469 (E3)	WHT	Sep. 1998
NGC 7603	WHT	June 1997
PB 3894	WHT	Feb. 1998
QSO B0257+0228	WHT	Sep. 2002
UGC 3478	WHT	Oct. 1998
WAS 45	WHT	June 1999
WAS 45 (Apr03)	WHT	Apr. 2003

Table 1: List of observing telescopes and dates.

An example of the observed polarization spectra (after adjusting for spectroscopic redshift; see section 4.4) is shown in figure 16.

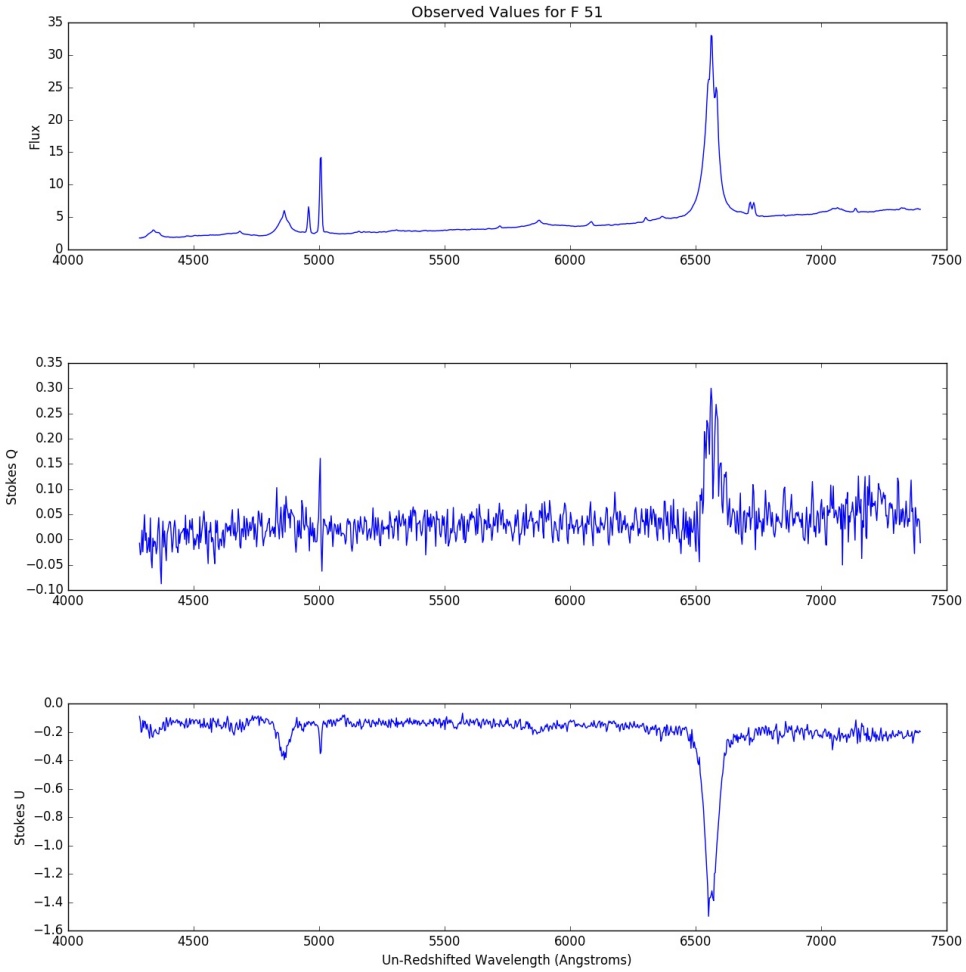

Figure 16: The observed polarization spectrum for F51 after accounting for spectroscopic redshift (see section 4.4)

4.2 Object Characteristics

Relevant observational information for each object is listed in table 1.

Object	Object Type	Bolometric Luminosity (W)	Polarization Class
2E 4066	Sy1	$4.57 \cdot 10^{40}$	Unreliable
AKN 120	Sy1	$4.75 \cdot 10^{38}$	Equatorial
AKN 564	NLS1	$4.15 \cdot 10^{38}$	Null/Interstellar
ESO 12-21	Sy1	$2.10 \cdot 10^{37}$	
ESO 113-45	Sy1	$5.67 \cdot 10^{38}$	Equatorial
ESO 141-35		$1.48 \cdot 10^{37}$	
F 51	Sy1	$2.59 \cdot 10^{38}$	Polar
I zw 1	NLS1	$4.99 \cdot 10^{38}$	Equatorial
IC 3599	NLS1	$1.32 \cdot 10^{38}$	Null/Interstellar
IRAS 17002+5153	NLS1	$6.25 \cdot 10^{38}$	
KUG 1031	NLS1	$2.59 \cdot 10^{38}$	Null/Interstellar
Mrk 6	Sy1.5	$3.60 \cdot 10^{38}$	Equatorial
Mrk 279	Sy1	$5.68 \cdot 10^{38}$	Unreliable
Mrk 290	Sy1.5	$4.79 \cdot 10^{38}$	Unreliable
Mrk 304	Sy1	$4.76 \cdot 10^{38}$	Unreliable
Mrk 335	NLS1	$3.88 \cdot 10^{38}$	
Mrk 478	NLS1	$5.07 \cdot 10^{38}$	Null/Interstellar
Mrk 486	NLS1	$2.91 \cdot 10^{38}$	Polar
Mrk 507	NLS1	$3.20 \cdot 10^{38}$	Polar
Mrk 509	Sy1.5	$5.43 \cdot 10^{38}$	Equatorial
Mrk 590	Sy1	$4.63 \cdot 10^{38}$	
Mrk 705	NLS1	$4.55 \cdot 10^{38}$	
Mrk 766	Sy1	$4.16 \cdot 10^{38}$	Polar
Mrk 841	Sy1.5	$4.75 \cdot 10^{38}$	Unreliable
Mrk 871	Sy1.5	$1.63 \cdot 10^{37}$	
Mrk 876	Sy1	$8.49 \cdot 10^{38}$	Equatorial (?)
Mrk 915	Sy1	$3.71 \cdot 10^{38}$	Polar
Mrk 926	Sy1.5	$7.41 \cdot 10^{38}$	Equatorial
Mrk 1239	NLS1	$1.50 \cdot 10^{38}$	Polar*
MS 1849.2-7832	Sy1	$2.18 \cdot 10^{37}$	Equatorial (?)

NGC 985	Sy1	$5.11 \cdot 10^{38}$	Equatorial
NGC 3227	Sy1.5	$1.94 \cdot 10^{38}$	Polar
NGC 3516	Sy1.5	$3.10 \cdot 10^{38}$	Unreliable
NGC 3783	Sy1.5	$3.82 \cdot 10^{38}$	Equatorial
NGC 4051	NLS1	$1.77 \cdot 10^{38}$	Unreliable
NGC 4151	Sy1.5	$2.11 \cdot 10^{38}$	Equatorial
NGC 4593	Sy1	$3.52 \cdot 10^{38}$	
NGC 5548	Sy1.5	$5.07 \cdot 10^{38}$	
NGC 6104	Sy1.5	$1.12 \cdot 10^{38}$	Equatorial
NGC 7213	Sy1	$1.85 \cdot 10^{38}$	Null/Interstellar
NGC 7469	Sy1	$3.49 \cdot 10^{38}$	Equatorial (?)
NGC 7603	Sy1.5	$5.24 \cdot 10^{38}$	Null/Interstellar
PB 3894	NLS1	$5.41 \cdot 10^{38}$	Equatorial
QSO B0257+0228	QSO	$7.59 \cdot 10^{38}$	Unreliable
UGC 3478	NLS1 (?)	$2.30 \cdot 10^{38}$	Unreliable
WAS 45	Sy 1.9	$1.66 \cdot 10^{37}$	Polar

Table 2: Characteristics of polarization sample. Bolometric luminosities are based on K-Band for 2E 4066, IC3599, Mrk 915, NGC 6104, and QSO B0257+0228. 12μm measurements were used for ESO 12-21, ESO 141-35, IRAS 17002+5153, Mrk 871, MS 1849.2-7832, and WAS 45. 2-10keV measurements were used for all remaining objects.

The first of these is object type. The types listed here utilize the same definitions for AGN classifications outlined in section 1.2 and were taken from information available in the NASA/IPAC Extragalactic Database (NED)[2] as well as previous studies similar to our own (Smith et al. 2002; Smith et al. 2005).

Second is the bolometric luminosity. These luminosities were primarily calculated from reported 2-10keV X-ray fluxes (obtained from NED) using an empirical soft X-ray bolometric correction (Runnoe, Brotherton, & Shang 2012 (1)):

[2]https://ned.ipac.caltech.edu

$$\log(L_{\text{bol}}) = (33.06 \pm 3.17) + (0.29 \pm 0.072)\log(L_{2-10\text{keV}}) \tag{42}$$

Some objects did not have reported values within this range. For these cases, we utilized other empirical corrections including a 2μm correction (for K-band measurements) (Runnoe, Brotherton, & Shang 2012 (2)):

$$\log(L_{\text{bol}}) = (1.847 \pm 3.176) + (0.981 \pm 0.071)\log(L_{2\mu\text{m}}) \tag{43}$$

and a 12μm correction (Runnoe, Brotherton, & Shang 2012 (2)):

$$\log(L_{\text{bol}}) = (8.195 \pm 4.303) + (0.822 \pm 0.096)\log(L_{2\mu\text{m}}) \tag{44}$$

Since most of the data in NED are presented as fluxes, we first had to convert each flux to a luminosity. This was done using the simple equation

$$L = 4\pi r^2 F \tag{45}$$

where r is the distance to the object (using redshift-independent distances from NED when available, Hubble distances otherwise). In the few cases where our calculated redshift differed significantly from the expected value (namely ESO141-45 and NGC 7213), we instead utilized Hubble's Law:

$$D = \frac{v}{H_0} \tag{46}$$

Where $H_0(\approx 65\text{km s}^{-1}\,\text{Mpc}^{-1})$ is the Hubble constant. Since the redshifts of these objects are relatively low, we can use a simple relationship in conjunction with equation 46 to determine their distance:

$$z \approx \frac{v}{c} \tag{47}$$

thus,

$$D = \frac{z}{H_0} c \tag{48}$$

Lastly, we give the object's polarization class. This gives information regarding the object's optical polarization spectrum and whether it is clearly dominated by a certain scattering geometry (as discussed in chapter 3 and section 1.5). For the tables to follow, the polarization classes are defined as:

Equatorial: Signature implies equatorial scattering dominates

Polar: Signature implies polar scattering dominates

Null/Interstellar: Signature shows no significant polarization or cannot be distinguished from foreground interstellar population

Unreliable: Polarization signal is not clear enough to draw conclusions

Objects with no listed classification did not have obvious features in their polarization spectrum or had spectra that did not have obvious signatures, despite significant signal. Specifics for how these classifications were assigned are described in section 5.1.

4.3 Summary of Analysis Techniques

The reduced observational data set for each object consists of six associated values: wavelength, total flux density, fluxes in Stokes Q and U, and the variance in the aforementioned Stokes parameters. The objective of this analysis is twofold:

1. To determine the polarization position angle swing across the broad Hα profile
2. To determine the width of the polarized broad Hα profile

To achieve these goals, we first accounted for the redshifting of each object. This was done by fitting Gaussian profiles to observed narrow lines and shifting each spectrum's wavelength values to align these peaks with their rest wavelengths (see section 4.4).

The newly shifted total flux and Stokes spectra then had their wavelength range restricted such that they contained primarily the broad Hα profile. The wavelength range was tuned by hand and was centered at the wavelength at which 50% of the integrated total flux was contained in each side of the spectrum. As such, the wavelength range we were left with in each case flanked the 50th percentile of the total flux equally on both the red and blue sides of the profile (see section 4.5).

These polarization spectra had their continua modeled using a linear fit which omitted data values more than three standard deviations from the mean value across the reduced wavelength range. This fitted continuum was subtracted from each spectrum (see section 4.6).

The inter-percentile velocities of the Hα lines were then measured from the spectra using two separate methods for the total flux and the polarized flux. In the case of total flux, we simply found the locations of the 25th and 75th percentiles and utilized the inter-percentile wavelength range (see section 4.7.1). For the polarized flux, we instead ran a series of Monte-Carlo trials to determine the most statistically likely value of the inter-percentile wavelength range (see section 4.7.2).

For measurements involving polarization characteristics of the spectrum (such as the polarized inter-percentile velocity and the polarization position angle swing), we first binned the data to achieve higher signal-to-noise. The process with which the data were binned is explained at length in section 4.8.

Finally, we utilized these binned data to determine a host of values associated with the polarization characteristics of the spectra. We began by calculating the polarization position angle swing using two methods. The first of these involved finding the average polarization position angle on either side of the broad Hα core (see section 4.9.1). The second determined the polarization position angle swing within the broad Hα line by simply finding the difference in the largest and smallest value (see section 4.9.2).

We then determined the average percentage polarization and polarization position angle swing in both the broad Hα core and the continuum region. This was conducted via modified forms of the equations used to define each of these values (see section 4.10).

4.4 Spectroscopic Redshift

Spectroscopic redshift values are required to convert interpercentile wavelength ranges to interpercentile velocities (see section 4.7). To obtain these values, we looked at emission lines present in

the data. We aimed to fit Gaussian profiles to the following emission lines based on their relative strength and narrowness:

- Oxygen [III] (5007Å)
- Nitrogen [II] (6583Å)
- Narrow Hydrogen α (6563Å)
- Narrow Hydrogen β (4861Å)
- Broad Hydrogen α (Assuming 6563Å)

These lines were modeled in GNUplot using a generalized Gaussian curve which included terms for a linear offset. This function was of the form

$$f(x) = ae^{-\frac{(x-b)^2}{2c^2}} + dx + f \tag{49}$$

Where a, b, c, d, and f are fit parameters that represent the following related quantities:

a : Amplitude of the Gaussian (in milliJanskys)
b : Mean value of the Gaussian (in Angstroms)
c : Standard deviation of the Gaussian (in square Angstroms)
d : Slope of the continuum flux (in milliJanskys per Angstrom)
f : Vertical offset of the continuum flux (in milliJanskys)

Before the fit was applied to the data, initial values were fed to the code. These values were estimated by eye from the shape of the emission line profiles. The one exception for this process is the slope of the continuum, d, which is chosen to have an initial value of $\pm 1 \text{mJy}\text{Å}^{-1}$.

For an example of this process, we can look to figure 17 which shows the portion of the flux spectra for Mrk 509 E1 that corresponds to the Oxygen III emission line. Initial guesses for each of the fit parameters were determined by visual inspection of the data. These values were (again with d being set to $\pm 1 \text{mJy}\text{Å}^{-1}$ by default):

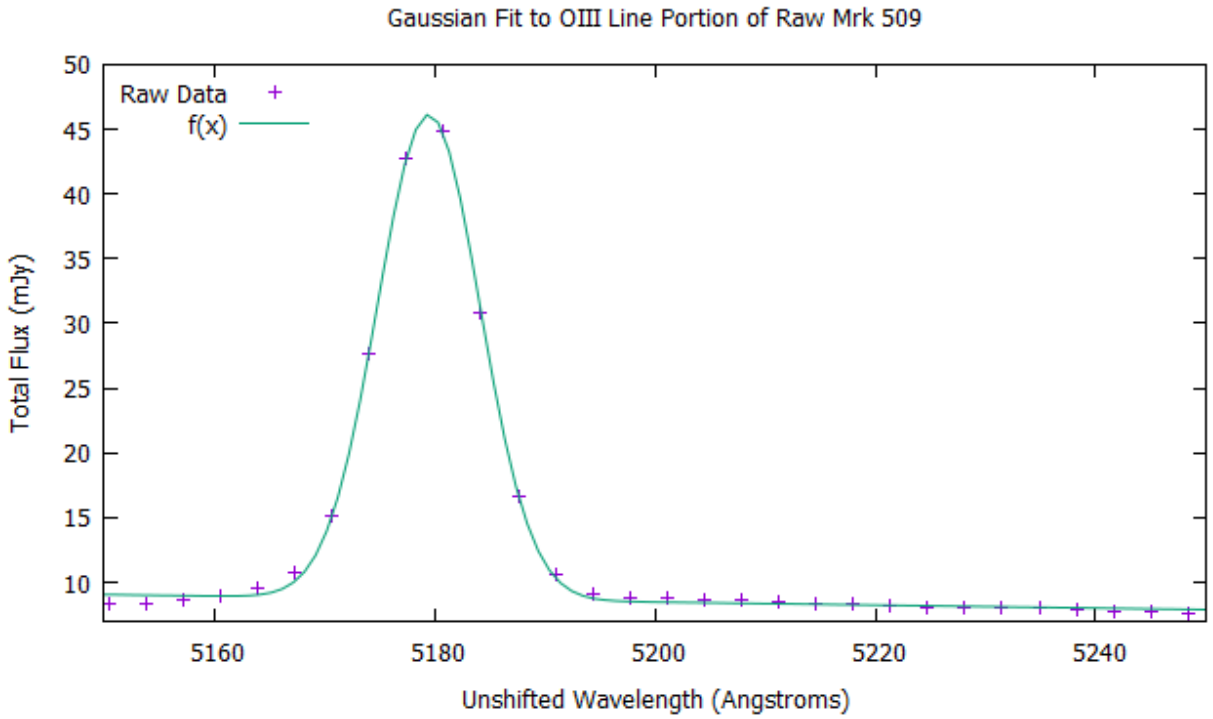

Figure 17: The O[III](5007Å) emission line portion of the Mrk 509 E1 flux spectrum with a Gaussian profile (defined by equation 49) fitted to the data.

$$a = 35\text{mJy}$$
$$b = 5180\text{Å}$$
$$c = 10\text{Å}$$
$$f = 10\text{mJy}$$

From here, the built-in fitting procedure in GNUplot was used to fit the Gaussian profile defined in equation 49 to the portion of the spectrum that corresponded to the chosen emission line. In the case of our example, this provided the result plotted in figure 17.

This fitting process produces a model for the best-fitting profile which can then be used to determine the spectroscopic redshift. Specifically, we can look at the value of b to determine the center of the line profile and, by extension, the difference in wavelength between the rest emission and the redshifted emission.

Our example yielded the following results:

$$
\begin{aligned}
a &= (37.4 \pm 0.4)\text{mJy} \\
b &= (5179.46 \pm 0.05)\text{Å} \\
c &= (4.65 \pm 0.05)\text{Å} \\
d &= (-0.012 \pm 0.003)\text{mJyÅ}^{-1} \\
f &= (70 \pm 12)\text{mJy}
\end{aligned}
$$

As stated above, the value of b corresponds to the redshifted center of the line profile, λ_{obs}. Using this value and the known rest wavelength of the line profile, λ_{rest}, we can determine a spectroscopic redshift in wavelength:

$$\Delta\lambda = \lambda_{obs} - \lambda_{rest} \tag{50}$$

The reported uncertainty of this value is simply that which was given by the fit code.

In general, astronomers usually discuss redshifts using a unit-less quantity, z:

$$z = \frac{\lambda_{obs} - \lambda_{rest}}{\lambda_{rest}} \tag{51}$$

In the example of Mrk 509 E1, the associated redshift values are $\Delta\lambda = 172$Å and $z = 0.034352$.

The uncertainty in the redshift can be determined using the analytical uncertainty propagation formula:

$$\delta f(\xi_0, \xi_1, ..., \xi_{max}) = \sqrt{\sum_{n=0}^{n_{max}} \left[\left(\delta\xi_n \frac{\partial f}{\partial \xi_n} \right)^2 \right]} \tag{52}$$

Using this with equation 51 and under the assumption that $\delta\lambda_{rest} = 0$,

$$\delta z = \frac{\delta\lambda_{obs}}{\lambda_{rest}} \tag{53}$$

Using a different version of equation 51,

$$\lambda_{rest} = \frac{\lambda_{obs}}{1+z} \tag{54}$$

we shifted the observed spectrum to the rest frame.

4.4.1 Multiple Gaussian Fits

For spectra with strong narrow lines in close proximity to each other, a multiple Gaussian fit was sometimes used. This followed the same process described earlier in this section, but involved more complex fit equations:

$$f(x) = \sum_{n=1}^{n_{max}} \left[\text{Normal}_n\left(x, a_n, b_n, c_n\right)\right] + dx + f \tag{55}$$

where

$$\text{Normal}_n\left(x, a_n, b_n, c_n\right) = a_n e^{-\frac{(x-b_n)^2}{2{c_n}^2}} : \text{a Gaussian distribution}$$
$$d : \text{Slope of the continuum flux}$$
$$f : \text{Vertical offset of the continuum flux}$$

Despite looking analytically complex, fitting these functions is no more difficult than fitting single Gaussian profiles. Much like above, initial guesses for the individual a_n, b_n, and c_n values (as well as a value for f) are provided to the code.

4.4.2 Redshift Results

A list of redshift values obtained from the fits for each object is displayed in table 3. This table also displays which line was used to determine each redshift as well as its percent discrepancy with the value reported in the SIMBAD astronomical database[3].

[3] http://simbad.u-strasbg.fr/simbad

For objects with multiple resultant redshifts, we chose to primarily use the one associated with specific lines. These lines, in order from most desirable to least desirable, are as follows:

1. Narrow Hα
2. [NII]6584
3. [OIII]5007
4. Narrow Hβ
5. Broad Hα

The redshift value we chose for each objected has been emboldened in table 3.

Object	Line	$\Delta\lambda$ (Å)	z	% Discrepancy
2E 4066	Broad Hα	1977 ± 0.6	**0.30123** $\pm$ 0.00009	1.43%
Akn 120 (Epoch 1)	Broad Hα	220 ± 0.2	**0.03352** $\pm$ 0.00003	3.78%
(Epoch 2)	Broad Hα	220 ± 0.2	**0.03352** $\pm$ 0.00003	3.78%
Akn 564	Broad Hα	162 ± 2	**0.0247** $\pm$ 0.0003	0.94%
(Apr. 03)	Narrow Hβ	118 ± 0.3	0.024228 ± 0.00006	2.58%
	[OIII]4959	121 ± 0.07	0.02440 ± 0.00001	2.57%
	[OIII]5007	122 ± 0.06	**0.02437** $\pm$ 0.00001	2.21%
	Broad Hα	159 ± 0.3	0.02423 ± 0.00005	2.77%
ESO 12-21	Narrow Hβ	160 ± 0.2	0.03292 ± 0.00004	1.44%
	[OIII]4959	162 ± 0.3	0.03267 ± 0.00006	2.18%
	[OIII]5007	164 ± 0.4	**0.03275** $\pm$ 0.00008	1.92%
	Broad Hα	215 ± 0.4	0.03276 ± 0.00006	1.91%
ESO 113-45	Broad Hβ	225 ± 2	0.0463 ± 0.0004	3.92%
	[OIII]4959	229 ± 0.3	0.04618 ± 0.00006	4.14%
	[OIII]5007	231 ± 0.09	**0.04614** $\pm$ 0.00002	4.23%
	Broad Hα	305 ± 0.8	0.0465 ± 0.0001	3.53%
ESO 141-35	Broad Hβ	181 ± 0.9	0.0372 ± 0.0002	135.99%
	[OIII]4959	183 ± 0.08	0.03690 ± 0.00002	133.89%
	[OIII]5007	185 ± 0.08	**0.03695** $\pm$ 0.00002	134.18%
	Broad Hα	240 ± 0.7	0.0366 ± 0.0001	131.77%

F 51	Broad Hβ	67 ± 0.6	0.0138 ± 0.0001	4.02%
	[OIII]4959	70 ± 0.05	0.01412 ± 0.00001	1.71%
	[OIII]5007	70 ± 0.07	**0.01398** ± 0.00001	2.65%
	Broad Hα	92 ± 0.5	0.01402 ± 0.00008	2.39%
IC 3599 (Apr03)	Narrow Hβ	103 ± 0.2	0.02119 ± 0.00004	2.07%
	[OIII]4959	104 ± 0.1	0.02097 ± 0.00002	1.02%
	[OIII]5007	105 ± 0.08	**0.02097** ± 0.00002	1.01%
	Broad Hα	139 ± 3	0.0212 ± 0.0005	2.02%
IRAS 17002+5153	Broad Hα	1894 ± 0.5	**0.28859** ± 0.00008	0.14%
I zw 1 (Aug06)	Broad Hβ	298 ± 0.2	0.06130 ± 0.00004	2.17%
	Broad Hα	396 ± 0.2	**0.06033** ± 0.00003	0.56%
(Sep02)	Broad Hβ	294 ± 0.3	0.06048 ± 0.00006	0.80%
	Broad Hα	398 ± 0.3	**0.06064** ± 0.00005	1.07%
(Epoch 1)	Broad Hβ	294 ± 0.4	0.06048 ± 0.00008	0.80%
	Broad Hα	397 ± 0.4	**0.06049** ± 0.00008	0.82%
(Epoch 2)	Broad Hα	398 ± 0.3	**0.06064** ± 0.00005	1.07%
KUG 1031 (Apr03)	Narrow Hβ	211 ± 0.2	0.04341 ± 0.00004	0.78%
	[OIII]4959	215 ± 0.3	0.04336 ± 0.00006	0.66%
	[OIII]5007	217 ± 0.2	**0.04334** ± 0.00004	0.63%
	Broad Hα	284 ± 0.4	0.04327 ± 0.00006	0.47%
Mrk 6 (Epoch 1)	Broad Hα	114 ± 0.7	**0.0174** ± 0.0002	6.99%
(Epoch 2)	Broad Hα	117 ± 0.8	**0.0178** ± 0.0002	4.54%
Mrk 279	Broad Hα	202 ± 0.4	**0.03078** ± 0.00006	0.58%
Mrk 290	Broad Hα	199 ± 0.6	**0.03032** ± 0.00009	0.30%
Mrk 304	Broad Hβ	318 ± 0.9	0.0654 ± 0.0002	1.32%
	[OIII]4959	324 ± 0.5	0.0653 ± 0.0001	1.44%
	[OIII]5007	327 ± 0.3	**0.06534** ± 0.00006	1.48%
	Broad Hα	431 ± 0.5	0.06567 ± 0.00008	0.94%
Mrk 335	Hα	170 ± 0.2	**0.02590** ± 0.00003	1.91%
Mrk 478 (Apr. 03)	Narrow Hβ	377 ± 0.2	**0.07756** ± 0.00004	0.72%
	Broad Hα	506 ± 0.3	0.07710 ± 0.00005	0.13%
(Jun. 03)	Narrow Hβ	374 ± 0.3	**0.07694** ± 0.00006	0.08%
	Broad Hα	505 ± 0.3	0.07695 ± 0.00005	0.07%
Mrk 486	Narrow Hβ	188 ± 0.3	0.03868 ± 0.00006	0.83%
	[OIII]4959	192 ± 0.2	0.03872 ± 0.00004	0.72%

	[OIII]5007	194 ± 0.2	**0.03875** ± 0.00004	0.65%
(Apr03)	Broad Hβ	188 ± 0.3	0.03868 ± 0.00006	0.83%
	[OIII]4959	192 ± 0.2	0.03872 ± 0.00004	0.72%
	[OIII]5007	194 ± 0.2	**0.03875** ± 0.00004	0.65%
	Broad Hα	254 ± 0.3	0.03870 ± 0.00005	0.76%
Mrk 507	Broad Hβ	268 ± 0.5	0.0551 ± 0.0001	1.37%
	[OIII]5007	278 ± 0.3	**0.05552** ± 0.00006	0.68%
(Epoch 1)	Broad Hβ	167 ± 0.5	0.0344 ± 0.0001	0.82%
	[OIII]4959	171 ± 0.05	0.03448 ± 0.00001	1.19%
	[OIII]5007	172 ± 0.05	**0.03435** ± 0.00001	0.81%
	Broad Hα	226 ± 0.4	0.03444 ± 0.00006	1.05%
(Epoch 2)	Broad Hβ	167 ± 0.6	0.0344 ± 0.0001	0.82%
	[OIII]4959	170 ± 0.08	0.03428 ± 0.00002	0.60%
	[OIII]5007	171 ± 0.05	**0.03415** ± 0.00001	0.22%
	Broad Hα	224 ± 0.4	0.03413 ± 0.00006	0.16%
(Epoch 3)	Broad Hβ	168 ± 0.7	0.0346 ± 0.0001	1.42%
	[OIII]4959	171 ± 0.05	0.03448 ± 0.00001	1.19%
	[OIII]5007	172 ± 0.04	**0.03435** ± 0.00001	0.81%
	Broad Hα	226 ± 0.5	0.03444 ± 0.00008	1.05%
Mrk 590	[OIII]4959	130 ± 0.2	0.02622 ± 0.00004	0.48%
	[OIII]5007	131 ± 0.07	**0.02616** ± 0.00001	0.28%
Mrk 705	Broad Hα	194 ± 0.3	**0.02956** ± 0.00005	2.71%
Mrk 766	Narrow Hβ	64 ± 0.3	0.01317 ± 0.00006	3.59%
	[OIII]4959	65 ± 0.09	0.01311 ± 0.00002	3.13%
	[OIII]5007	65 ± 0.2	**0.01298** ± 0.00004	0.81%
(Apr 03)	Narrow Hβ	64 ± 0.3	0.01317 ± 0.00006	3.59%
	[OIII]4959	65 ± 0.1	0.01311 ± 0.00002	3.13%
	[OIII]5007	66 ± 0.09	**0.01318** ± 0.00002	3.71%
	Broad H-Alpha	86 ± 0.6	0.01310 ± 0.00009	3.10%
Mrk 841	[OIII]4959	182 ± 0.03	0.03670 ± 0.00001	0.77%
	[OIII]5007	184 ± 0.03	**0.03675** ± 0.00001	0.90%
	Broad H-Alpha	229 ± 0.8	0.0349 ± 0.0002	4.19%
Mrk 871	Broad Hβ	167 ± 0.8	0.0344 ± 0.0002	2.68%
	[OIII]4959	166 ± 0.2	0.03347 ± 0.00004	0.22%
	[OIII]5007	168 ± 0.08	**0.03355** ± 0.00002	0.46%

Mrk 876	Broad Hα	850 ± 0.7	**0.1295** $\pm$ 0.0002	6.50%
Mrk 915	Narrow Hβ	117 ± 0.3	0.02407 ± 0.00006	0.11%
	[OIII]4959	119 ± 0.04	0.02400 ± 0.00001	0.19%
	[OIII]5007	120 ± 0.04	**0.02397** $\pm$ 0.00001	0.32%
	Broad Hα	160 ± 2	0.0244 ± 0.0003	1.4%
Mrk 926	Narrow Hβ	229 ± 0.2	0.04711 ± 0.00004	0.19%
	[OIII]4959	233 ± 0.2	0.04699 ± 0.00004	0.07%
	[OIII]5007	236 ± 0.2	**0.04713** $\pm$ 0.00004	0.24%
	Broad Hα	312 ± 3	0.0475 ± 0.0005	1.1%
Mrk 1239	Narrow Hβ	98 ± 0.2	0.02016 ± 0.00004	2.86%
	Narrow Hα	130 ± 0.3	**0.01981** $\pm$ 0.00005	1.06%
MS 1849.2-7832	Narrow Hβ	207 ± 2	0.0426 ± 0.0005	1.39%
	[OIII]4959	209 ± 0.3	0.04215 ± 0.00006	0.35%
	[OIII]5007	211 ± 0.06	**0.04214** $\pm$ 0.00001	0.34%
	Broad Hα	278 ± 0.9	0.0424 ± 0.0002	0.85%
NGC 985	Broad Hβ	218 ± 2	0.0448 ± 0.0004	3.96%
	[OIII]4959	212 ± 0.05	0.04275 ± 0.00001	0.90%
	[OIII]5007	214 ± 0.05	**0.04274** $\pm$ 0.00001	0.93%
	Broad Hα	291 ± 0.9	0.0443 ± 0.0001	2.78%
NGC 3227	Broad Hβ	16 ± 0.7	0.0033 ± 0.0002	9.82%
	[OIII]4959	18 ± 0.2	0.00363 ± 0.00004	0.55%
	[OIII]5007	19 ± 0.09	**0.00380** $\pm$ 0.00002	3.96%
	Broad Hα	27 ± 0.6	0.00411 ± 0.00009	12.71%
NGC 3516	Broad Hα	54 ± 0.4	**0.00823** $\pm$ 0.00006	6.67%
NGC 3783	Broad Hβ	48 ± 0.5	0.0099 ± 0.0001	1.23%
	[OIII]4959	48 ± 0.07	0.00968 ± 0.00001	0.78%
	[OIII]5007	48 ± 0.06	**0.00959** $\pm$ 0.00001	1.73%
	Broad Hα	64 ± 0.4	0.00975 ± 0.00006	0.03%
NGC 4151 (Apr03)	Broad Hβ	17 ± 0.5	0.0035 ± 0.0001	7.21%
	[OIII]4959	17 ± 0.2	0.00343 ± 0.00004	5.09%
	[OIII]5007	17 ± 0.09	**0.00330** $\pm$ 0.00002	4.08%
	Broad Hα	24 ± 0.7	0.0037 ± 0.0002	12.1%
NGC 4593 (Epoch 1)	Broad Hα	57 ± 0.5	**0.00869** $\pm$ 0.00008	4.09%
(Epoch 2)	Broad Hβ	42 ± 0.5	0.0086 ± 0.0001	3.55%
	[OIII]4959	40 ± 0.05	0.00807 ± 0.00001	3.33%

	[OIII]5007	41 ± 0.2	**0.00819** ± 0.00004	1.86%
	Broad Hα	56 ± 0.6	0.00853 ± 0.00009	2.26%
NGC 5548	Broad Hα	109.3 ± 0.3	**0.01661** ± 0.00005	2.08%
NGC 6104	[NII]6548	183 ± 0.3	0.02795 ± 0.00005	0.39%
	Narrow Hα	183 ± 0.3	**0.02788** ± 0.00005	0.16%
	N[II] (6584Å)	183 ± 0.2	0.02780 ± 0.00003	0.16%
NGC 7213	[OIII]4959	23 ± 0.5	0.0046 ± 0.0001	20.97%
	[OIII]5007	25 ± 0.4	**0.00499** ± 0.00008	14.93%
	Broad Hα	44 ± 0.7	0.0067 ± 0.0001	14.23%
NGC 7469 (Epoch 1)	Broad Hα	109 ± 0.5	**0.01661** ± 0.00008	4.59%
(Epoch 2)	Broad Hβ	80 ± 0.6	0.0165 ± 0.0002	3.64%
	[OIII]4959	78 ± 0.2	0.01573 ± 0.00004	0.95%
	[OIII]5007	79 ± 0.2	**0.01578** ± 0.00004	0.64%
	Broad Hα	110 ± 0.6	0.01676 ± 0.00009	5.55%
(Epoch 3)	Broad Hα	110 ± 0.5	**0.01676** ± 0.00008	5.55%
NGC 7603	Broad Hα	177 ± 0.3	**0.02697** ± 0.00005	7.94%
PB 3894	Narrow Hα	529 ± 0.3	**0.08060** ± 0.00005	0.49%
QSO B0257+0228	Broad Hβ	556 ± 2	0.1144 ± 0.0005	0.54%
	[OIII]4959	559 ± 0.6	0.1127 ± 0.0002	1.98%
	[OIII]5007	566 ± 2	**0.1130** ± 0.0004	1.70%
	Broad Hα	747 ± 0.6	0.11382 ± 0.00009	1.03%
UGC 3478	Broad Hα	84 ± 0.4	**0.01280** ± 0.00006	1.55%
WAS 45	[NII]6548	168 ± 0.7	0.0257 ± 0.0002	2.63%
	Narrow H-Alpha	168 ± 0.3	**0.02560** ± 0.00005	2.39%
	[NII]6584	168 ± 0.3	0.02552 ± 0.00005	2.07%
(Apr03)	Narrow H-Beta	124 ± 0.08	0.02551 ± 0.00002	2.04%
	[OIII]4959	126 ± 0.2	0.002541 ± 0.00004	1.63%
	[OIII]5007	127 ± 0.07	0.02536 ± 0.00001	1.46%
	[NII]6548	168 ± 3	0.0257 ± 0.0005	2.63%
	Narrow H-Alpha	168 ± 0.9	**0.0256** ± 0.0002	2.39%
	[NII]6584	168 ± 0.8	0.0255 ± 0.0002	2.07%

Table 3: Spectroscopic redshifts found by fitting a Gaussian function to the chosen line profile in GNUplot. Reported discrepancies were found by comparison to SIMBAD data. The calculated redshift values for ESO 141-45 and NGC 7213 are used despite their large discrepancies. The value for NGC 4051 is taken to be 0.00216 in accordance with the value reported on SIMBAD.

4.5 Broad-Line Region Selection

The spectra in this study cover various wavelength ranges; some are restricted only to the Hα region while others extend to Hβ. For the purposes of this study, we focus mainly on the broad-line Hα. In order to restrict the analysis to the wavelength range of interest, a method for selecting a suitable wavelength range to encompass the broad Hα line was needed.

First, we made an educated guess of the central wavelength of the broad Hα line. While it is not true that the center of the broad Hydrogen α emission will consistently match that of the narrow-line emission, it is a good place to start. Thus, we first restricted our data to a region that included wavelengths in a 600Å range on either side of the narrow Hα emission wavelength (6563Å). If the spectrum did not include values that spanned this range, the largest possible range was chosen instead.

The total flux of the restricted spectrum (including the continuum flux) was obtained through numerically integrating over wavelength. The median of the cumulative flux distribution was then found and used as the new central wavelength for the restricted region (with the same 600Årange on either side). This process was repeated five times. After a primary range was obtained, the continuum was subtracted and the same process was conducted using a smaller wavelength range. This range is user-defined and this was tailored to each object individually. The spectrum segment with the restricted wavelength range that is produced as a result of this process is hence referred to as the "Hα spectrum."

It is important to note that while the wavelength range of the Hα spectrum was found using the total flux spectrum, equivalent wavelength limits were used to extract restricted spectra for the Stokes Q and U parameters as well as their associated variances.

4.5.1 Strong Narrow Lines

NGC 6104 and WAS 45 contain particularly strong narrow lines superimposed on the broad Hα profile. For NGC 6104 and the first data set for WAS 45, these lines were subtracted directly using the fit performed for redshift determination (see section 4.4). In the case of the second data set for WAS 45 (WAS 45 (Apr03)), narrow line subtraction proved to be quite difficult due to small offsets in each peak when compared to the fit. For this particular object, we modeled the broad-line portion of the spectrum as a sum of four Gaussian profiles (see section 4.4.1): NII (6548Å), narrow Hα, NII (6584Å), and broad Hα. The spectrum used for analysis was then reconstructed using the resulting fit to the broad Hα profile.

4.6 Continuum Subtraction and Polarized Intensity Calculation

With the wavelength range of the data restricted, continuum subtraction can be more easily performed for the Stokes Q and U spectra. It is imperative that this underlying continuum be removed as we aim to determine the polarization properties of the broad Hα line. The continuum within the restricted wavelength range is assumed to be approximately linear, allowing us to determine a simple linear model within the range.

While in most cases it is a simple process of linear regression to determine a continuum, the observational data for the Stokes parameters are quite noisy (as seen in figure 18). To avoid statistical outliers from unduly influencing the fit, only points that were within three standard deviations of the mean were considered. These selected data were fit with a line of the form

$$f(x) = ax + b \tag{56}$$

where a and b are fit parameters that relate to the slope and vertical offset of the continuum respectively.

This linear continuum fit was then subtracted from the Hα segments of the Q and U spectra to produce the continuum-subtracted Hα Stokes Q and U spectra.

With these continuum-subtracted spectra, we can now calculate the polarized intensity spectrum. The value of the polarized intensity at each wavelength was calculated using equation 14. Since the spectra of both Q and U have significant observational uncertainty associated with them, un-

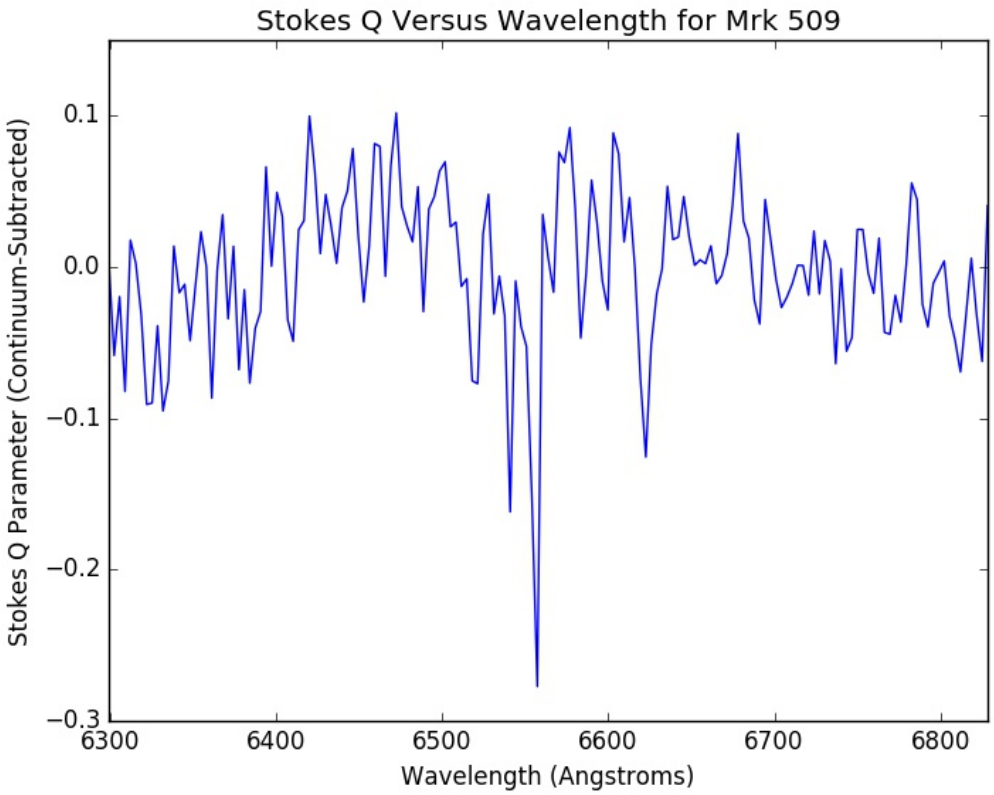

Figure 18: Reduced Stokes Q parameter versus wavelength in the broad-line Hα spectrum of Mrk 509 E1. Uncertainty in the measurements have been omitted for the sake of clarity.

certainty in the polarized intensity must be handled properly. To this end, we invoke the analytical uncertainty propagation formula (equation 52) in conjunction with equation 14 to find

$$\delta I_{pol} = \sqrt{\frac{Q^2(\delta Q)^2 + U^2(\delta U)^2}{Q^2 + U^2}} \tag{57}$$

4.7 Inter-Percentile Velocity Determination

For the purposes of this study, inter-percentile velocity shall be defined as the velocity which encompasses 50% of the broad-line region's flux. So far in the analysis of the data we have focused on wavelengths rather than velocities. Through this lens, the inter-percentile velocity can instead be represented by a wavelength range that is centered at the broad-line peak which contains half of the total flux in the broad-line profile.

To determine this range, we first determined the wavelengths at which the cumulative flux reached 25% and 75% of the total. These two values were then subtracted in order to determine the range – centered at the broad-line core – which contained 50% of the total flux.

4.7.1 Total Flux Line Profile

The total flux of the continuum-subtracted Hα spectrum was determined by numerical integration via the trapezoid rule (much like in section 4.5). Then, a modified integration routine was utilized to determine the wavelength locations of the 25th and 75th percentiles of the integrated flux. A visual representation of this process is seen in figures 19 and 20.

With these two quartile locations, the inter-percentile velocity range (in terms of wavelength) is simply their difference. The Doppler formula then provides us with a simple expression for converting this wavelength value into a velocity value:

$$\Delta v = \frac{\Delta\lambda}{\lambda_0} c \tag{58}$$

where λ_0 is the line center. In this study, this value is taken to be the wavelength at which the cumulative total flux reaches 50% of the total flux over the broad-line profile.

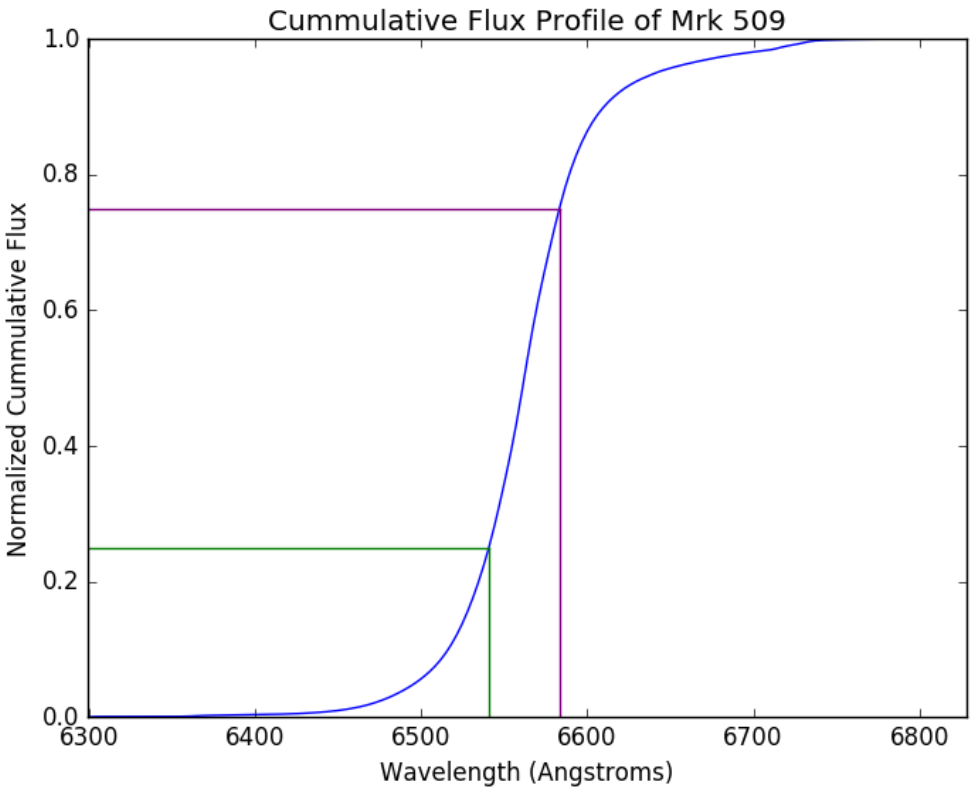

Figure 19: Cumulative flux (continuum-subtracted and normalized) spectrum for the Hα spectrum of Mrk 509 E1. The plotted lines are the locations at which the cumulative flux reaches 25% and 75% of the total.

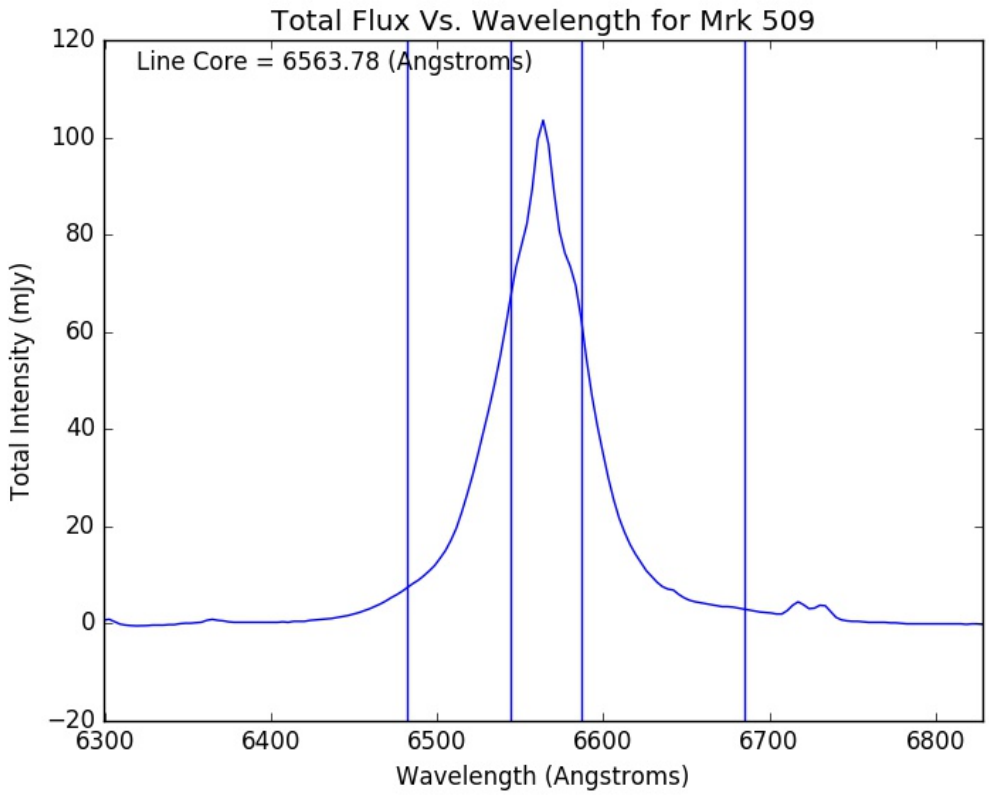

Figure 20: Total (continuum-subtracted) flux for the Hα spectrum of Mrk 509 E1. The four vertical lines are the locations at which the cumulative flux reaches 2.5%, 25%, 75% and 97.5% (from left to right respectively) of the total. The wavelength locations of the two inner values were subtracted to determine the interpercentile wavelength range, as given in the title.

4.7.2 Polarized Flux

Due to the noisy nature of the polarized flux profile, we had to utilize a more complex methodology than was adopted in section 4.7.1. We first assumed the probability distribution of the noise in the Stokes parameters to follow that of a Gaussian distribution:

$$f(x) = Ae^{-\frac{(x-\mu)^2}{2\sigma^2}} \tag{59}$$

where

A : Amplitude of the Gaussian

μ : Mean value of the Gaussian

σ : Standard deviation of the Gaussian

In order to determine the most probable value of the IPV, we generated 1000 Monte-Carlo trials using different realizations of the Stokes spectra. For each wavelength bin in the Stokes parameter spectra, a random shift was added to its flux value. These random shifts were taken from the Gaussian distribution outlined in equation 59. In each case, the mean of the probability density function (μ) was chosen to be zero and the standard deviation (σ) was set to the uncertainty in the Stokes parameter value.

Each of these newly formed Stokes parameter realizations were then used to calculate a polarized intensity spectrum (via equation 14). Due to the quadrature nature of equation 14, the resulting spectrum contains an artificial continuum greater than zero which was subtracted.

For each of these newly realized spectra, we attempted to calculated an IPV value using the same method outlined in section 4.7.1. In our initial tests with the code we found that the values achieved using that method yielded quantized results; only certain values were permitted to exist. This was a result of the non-continuous nature of our data. The bins made from the subtracted flux profile tended to be somewhat large, which lead to coarse resolution of the cumulative flux distribution. To deal with this issue, we implemented a system of linear interpolation.

First, an approximate wavelength of the desired percentile was determined using the simple method described above. Using this location and the location of the previous point (in wavelength), we

performed a linear interpolation between the data. using the cumulative flux at these wavelengths, we then determined remaining flux which must be included in order for the desired percentile to be achieved. The missing flux was calculated using the trapezoid rule. Under these assumptions, the wavelength at which this percentile occurs is given by

$$\lambda_{\%} = \lambda_0 + \frac{-y_0 + \sqrt{{y_0}^2 + 2mR}}{m} \tag{60}$$

where

λ_0 : Wavelength of the "previous point"

y_0 : Flux of the "previous point"

m : Slope of the constructed line

R : Calculated remainder between integrations

These IPV values determined from the 1000 realizations of the Stokes spectra are randomly distributed and follow a Gaussian probability density. These data were represented by a histogram (an example of which can be seen in figure 21) for the purposes of interpretation.

To determine the number of bins used in this histogram, we invoked the Rice Rule (Lane 2007). The rule states that the optimal number of bins for a normally distributed data set of size n is given by

$$k = \lceil 2n^{1/3} \rceil \tag{61}$$

For our sample size of 1000 normally distributed IPV values, the Rice Rule tells us to use 20 bins.

The resulting IPV distribution was then fitted with using the GNUplot fitting procedure. Each bin was assigned an associated uncertainty of one-half of the bin width in wavelength and $\sqrt{n}$ in count. An example fit can be seen in figure 22. From this fit, we extract the most probable inter-percentile wavelength range value (the center of the fitted Gaussian) and its associated deviation (the standard deviation of the fitted Gaussian).

These values are again expressed in terms of wavelength, meaning that equation 58 must be utilized

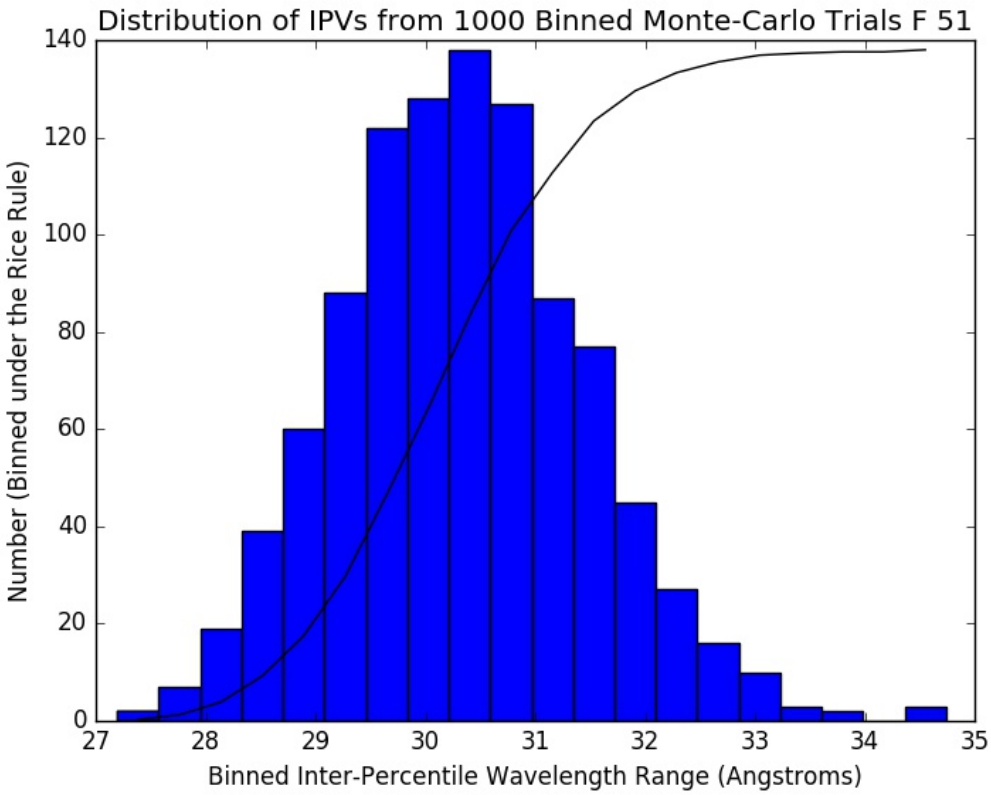

Figure 21: Distribution of IPV values from 1000 realizations of the continuum-subtracted polarized Hα spectrum from F 51. The black line plotted over the histogram is the the scaled (such that 100% is represented by the maximum bin value) cumulative distribution function.

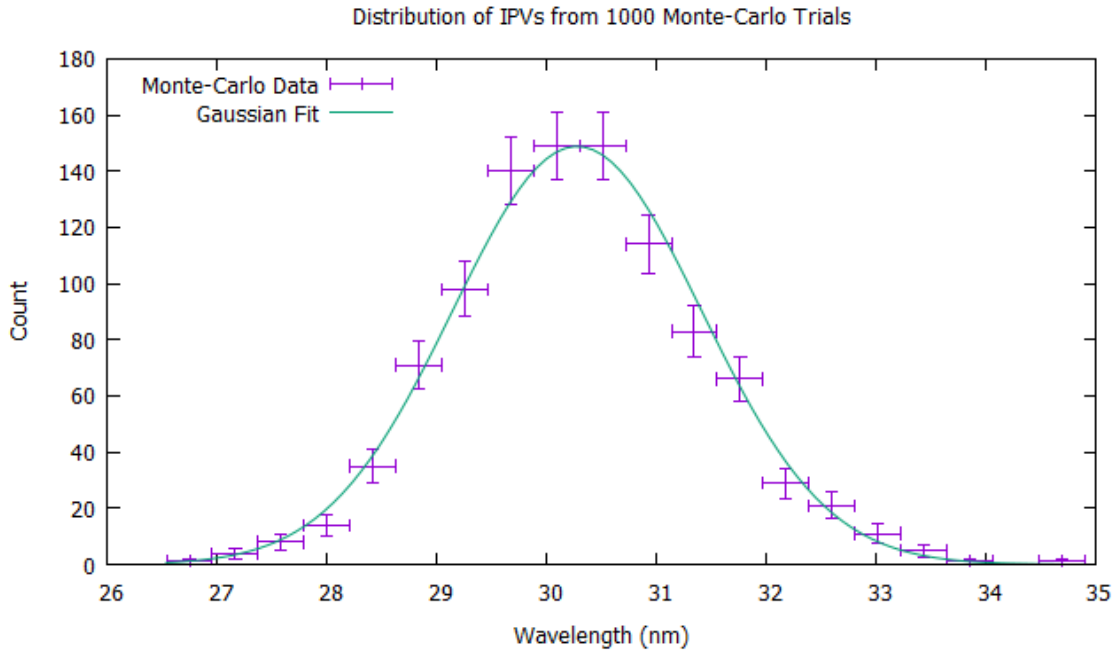

Figure 22: A Gaussian fit to the data shown in figure 21. The uncertainties in wavelength and count are give by half of each bin width and the square root of the bin count respectively.

again. We further find that – via equation 52 – our associated uncertainty is given by

$$\delta(\Delta v) = \frac{c}{\lambda_0}\sqrt{[\delta(\Delta\lambda)]^2 + \left(\frac{\Delta\lambda}{\lambda_0}\right)^2 (\delta\lambda_0)^2} \tag{62}$$

The uncertainty in the line center, $\delta\lambda_0$, can be assumed to be zero due to the high signal to noise. With this simplification, our associated uncertainty becomes

$$\delta(\Delta v) = \frac{\Delta\lambda}{\lambda_0}c \tag{63}$$

4.8 Data Binning

As discussed earlier, the polarized flux data (even post continuum-subtraction) is rather noisy in many cases. In order to increase the signal-to-noise ratio, a system was implemented to dynamically bin the data values. This process was based on the distance between the bin's center and the

broad-line core as well as the bin's total signal to noise. This allows us to determine physical values related to the object without worrying about them being lost to the inaccuracy of the measurements themselves.

The first of these bins had a 10Å width and was centered at the broad Hα core. The next two bins on both sides of the first also had their widths set to 10Å. Beyond this inner 50Å range (covering the core of the line profile), the dynamic binning routine was utilized. This routine was run separately on both the red side and blue side of the broad-line core.

To determine the optimal bin size, the routine established a running sum for both the calculated polarized intensity and its uncertainty (which was added in quadrature). It then continued to add values to this sum until one of three criteria were met:

1. The width of the bin was greater than or equal to one half of the distance between the bin center and the broad-line core.
2. The value of the cumulative polarized flux was greater than or equal to a five times the cumulative uncertainty (added in quadrature).
3. The bin would have extended beyond a wavelength range which contains 95% of the total broad-line flux (47.5% on either side of the broad-line core).

If the current bin met any of these criteria, the routine stored the bin's center, value, and width and moved on to form the next bin in that direction (in relation to the broad-line core). This was continued until a bin met criterion 3 above, at which point the routine ended. The same routine was run in the opposite direction afterwards. This binning scheme produces results like those shown in figure 23.

Once the bin boundaries were determined, the polarized flux, each of the Stokes parameters, and their respective variances (both prior to and after continuum subtraction) were binned within the same wavelength ranges. The uncertainty in these values was calculated by summing the variances of each individual point within a given bin in quadrature.

In addition, mean values for each of these bins were computed. This better represents the true shape of the distribution and is useful for qualitative analysis. An example is shown in figure 24.

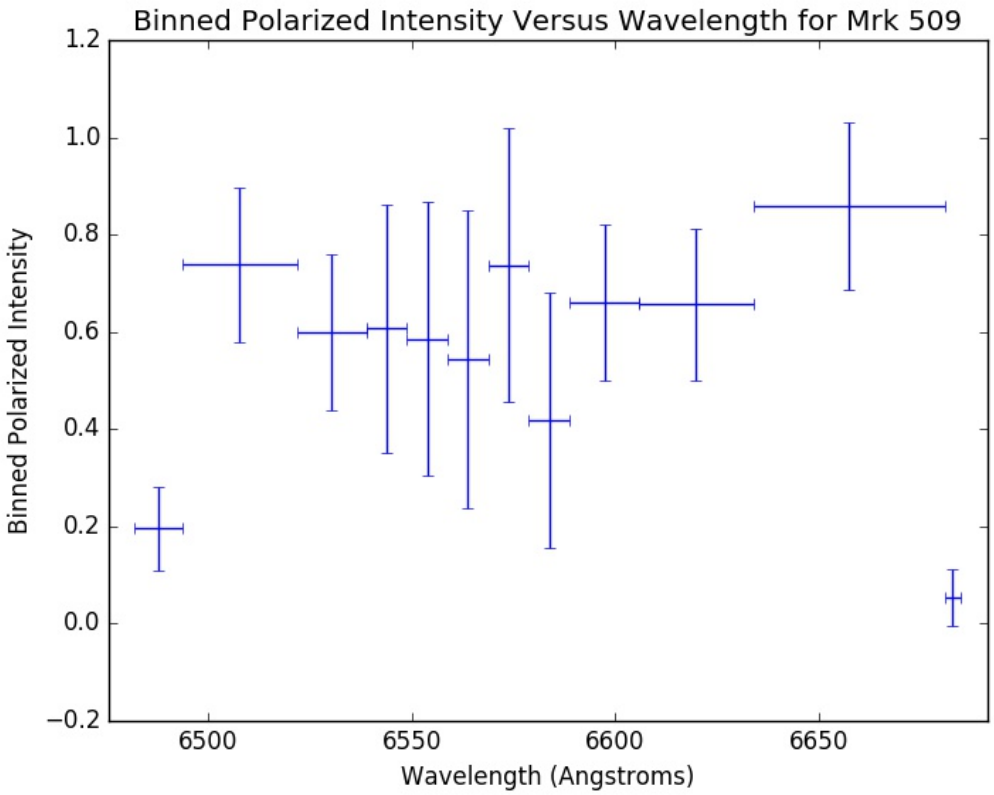

Figure 23: Binned (5σ significance) polarized intensity versus wavelength data in the Hα spectrum of Mrk 509 E1. The error bars for each bin represent the bin width (in the wavelength axis) and the cumulative uncertainty (in the intensity axis).

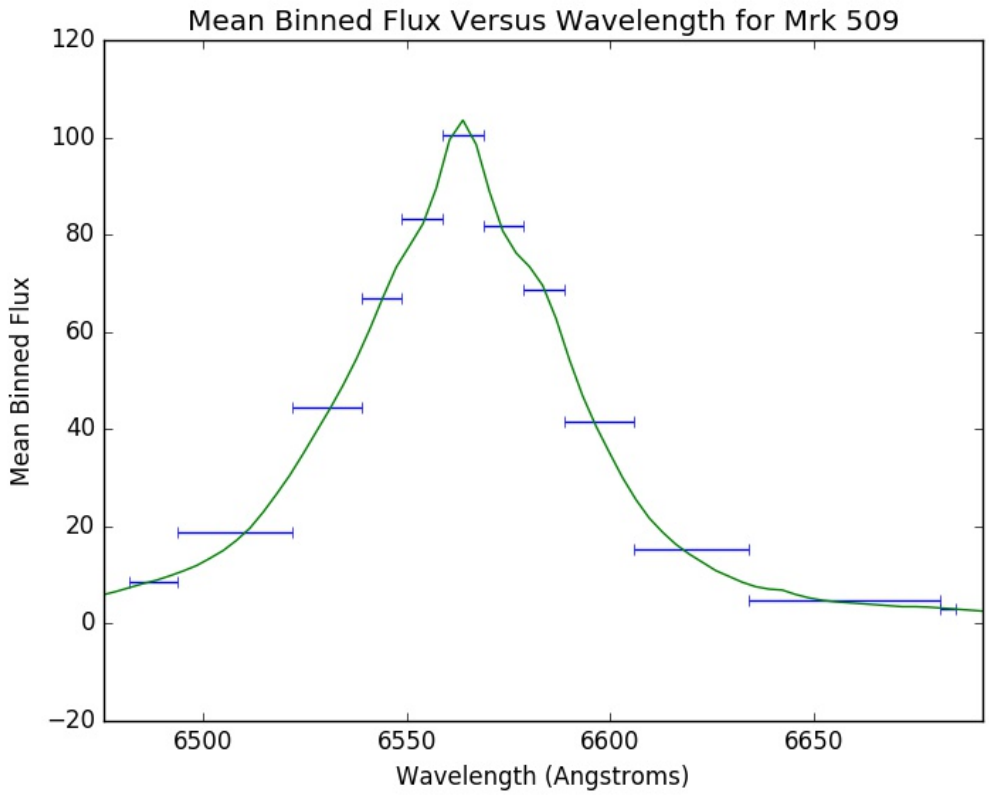

Figure 24: Mean binned total flux values for the broad Hα spectrum in Mrk 509 E1. The green curve plotted with the bins is the total flux spectrum (unbinned).

4.9 Polarization Position Angle and PA Swing

As described in section 2.2, the polarization position angle describes the orientation on the plane of the sky of the electric vector of polarized light. The amount by which it changes indicates certain aspects of the geometry of AGN (see section 3.3) and is useful for determining these non-resolvable characteristics. For example, a large polarization position angle swing (PA swing) is indicative of equatorial scattering. In order to find this PA swing we first need to calculate values for the PA itself.

From both the non-subtracted and continuum subtracted stokes parameters, we are able to determine the PA spectrum using equation 25). Again, we invoke the general form for analytical uncertainty (equation 52) in order to arrive at the uncertainty in the calculation:

$$\delta\theta = \frac{1}{2}\sqrt{\frac{U^2(\delta Q)^2 + Q^2(\delta U)^2}{Q^2 + U^2}} \tag{64}$$

The binned PA values were calculated by using the binned Stokes parameter values in equation 25. This method reveals a complication in the measurement of the PA swing; the values for the PA which are calculated using the continuum-subtracted data often vary wildly over the profile (as seen in figure 25). This is due to the fact that in many cases the continuum-subtracted Stokes spectra are noisy and fluctuate about zero. This drowns out important information about their ratio across the spectrum.

For this reason, the following methods of calculating the PA swing focus on the values of the PA calculated using the non-continuum subtracted binned Stokes parameters (an example of which is shown in figure 26).

4.9.1 PA Swing Via Integration Across the Total Flux IPV

To determine the PA swing, we utilized a few different methods. The first of these methods was to determine the average polarization position angle on both sides of the line core and then subtract them. The average PA value can be found using a modified version of equation 25:

$$\bar{\theta} = \frac{1}{2}\tan^{-1}\left(\frac{\bar{U}}{\bar{Q}}\right) \tag{65}$$

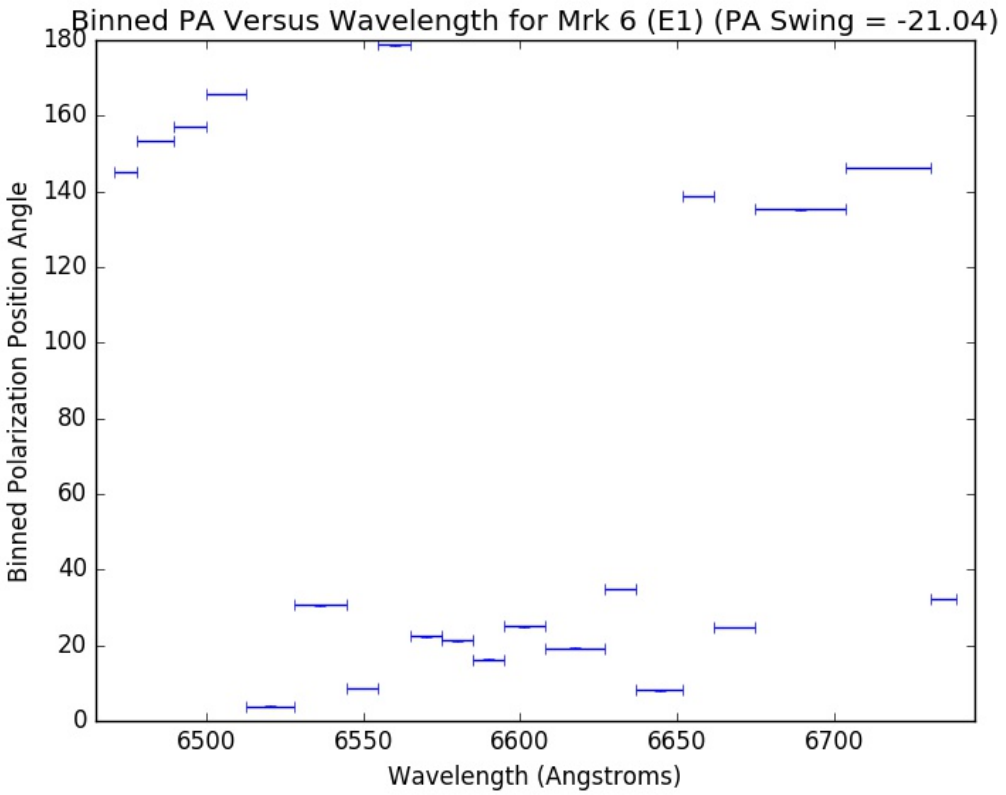

Figure 25: Polarization position angles calculated from continuum-subtracted Stokes Q and U parameter bins (of 5σ significance) for Mrk 6. These data vary wildly across the profile due to the fluctuation of the Stokes parameters about zero and the nature of the inverse tangent function. The PA swing value reported in the title is irrelevant.

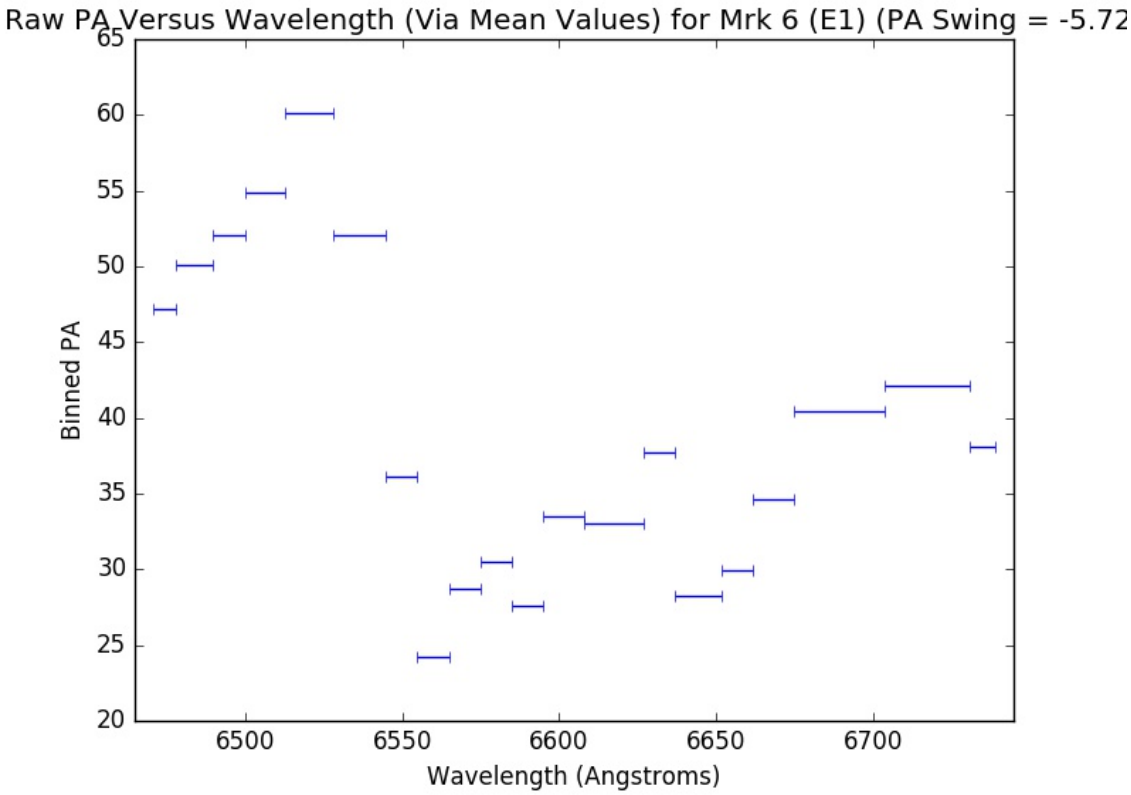

Figure 26: Polarization position angles calculated from reduced Stokes Q and U parameter bins (of 5σ significance) for Mrk 6 (E1). These values are much more indicative of the actual PA spectrum than those calculated using the continuum-subtracted data (as seen in figure 25). The single datum with a value of about 130° is a noise-related outlier. The PA swing value reported in the title is irrelevant.

Finding $\bar{U}$ and $\bar{Q}$ is achieved by integrating over each side of the profile. That is to say that for both the blue and red sides of the spectrum,

$$\bar{\theta} = \frac{1}{2}\tan^{-1}\left(\frac{\int U d\lambda}{\int Q d\lambda}\right) \tag{66}$$

Since our data are in the form of bins, we can simply sum across the bins. Our integrals then become sums:

$$\bar{\theta} = \frac{1}{2}\tan^{-1}\left(\frac{\sum_i U_i w_i}{\sum_i Q_i w_i}\right) \tag{67}$$

where

$$U_i, Q_i : \text{Bin value for the Stokes parameters}$$
$$w_i : \text{Width of each bin}$$

This summation is done across each bin on either side of the center bin (including the center bin in each case) to determine a blue-side and red-side average PA. The PA swing is then just the difference of these values:

$$\theta_{swing} = \bar{\theta}_{blue} - \bar{\theta}_{red}$$

4.9.2 PA Swing Via Direct Peak-to-Peak Measurement

The algorithm described in section 4.9.1 is designed to measure systematic swings across the Hα spectrum, akin to those that are expected from equatorial scattering. Not all of the objects in our sample exhibit this type of large-scale behavior though. An example of this can be easily seen in figure 26: the average PA swing calculated using the method described above is only 1.4° whereas there is a clearly visible swing over the first three bins of about 15°. In these cases, we took a simpler approach in determining the PA swing value.

The data analysis script saves its data in graphical and numerical form. With the numerical data,

we simply found the highest and lowest values of the PA across the broad Hα profile and subtracted them. In the aforementioned case, the PA swing measured using this method is approximately 14°.

4.10 Average Percentage Polarization and PA of the Core and Continuum

To measure the average percentage polarization in the two major regions of the broad Hα line, we utilized a numerical approximation of equation 22:

$$p = \frac{\sqrt{\left(\int Q d\lambda\right)^2 + \left(\int U d\lambda\right)^2}}{\int I d\lambda} \tag{68}$$

The average PA was calculated via a similar numerical approximation (see equation 66).

Within the inner 95%, these calculations were first conducted using the binned data. In this case, our approximation for the average percentage polarization becomes

$$p = \frac{\sqrt{\left(\sum_i Q_i w_i\right)^2 + \left(\sum_i U_i w_i\right)^2}}{\sum_i I_i w_i} \tag{69}$$

where

I_i : Bin value for the total flux

and our approximation for the average PA mirrors equation 67

For wavelengths outside of the inner 50% (but still within the inner 95%) of the broad Hα cumulative flux, we approximated the integrals using trapezoid rule. This allowed us to come to an average PA and percentage polarization of the continuum. Trapezoid rule was also used for the unbinned data within the core to determine both non-subtracted and continuum subtracted averages for the PA and percentage polarization within that region.

5 Results

Of the multitude of parameters isolated by our analysis, we determined that a small selection of them would be the most illuminating to examine. We chose to look at the central wavelengths of the total flux and polarized flux spectra, the velocity shift between these central wavelengths, the inter-percentile velocities of the total flux, and polarized flux spectra, and the ratio of these IPV values (section 5.2). Furthermore, we examined the PA swing – calculated through both methods as described in sections 4.9.1 and 4.9.2 – the percentage polarization of the continuum and the Hα core, as well as the ratio of these polarization percentages (see section 5.3).

5.1 Object Classification

Using the results taken from our analysis in conjunction with the two-component scattering model for Seyfert AGN (see section 1.5.1), we were able to determine a polarization class for most objects in our study. This classification is a way of describing whether each object's polarization spectrum is dominated by either polar or equatorial scattering, or has no significant polarization. These classifications were used in table 2 and follow very similar criterion as those outlined in previous studies (Smith et al. 2002; Smith et al. 2004; Smith et al. 2005).

Objects which are dominated by polar scattering are thought to be those that are close to being edge-on, as the line-of-sight to the BLR is partially blocked by the torus. Attenuation of broad-line Hα in addition to very narrow polarized flux features (from the polar scattering region's face-on viewing angle) cause the percentage polarization of the Hα core in these objects to be high. Furthermore, polar objects should not show significant PA swing, due to their face-on orientation. Thus, objects which had both high polarization percentage of the core as well as low PA swing were classified as polar objects.

Equatorial objects, on the other hand, are expected to have low polarization percentages of the Hα core in conjunction with high PA swings. Since these objects are thought to be viewed closer to face-on, a majority of the light reaching the observer is non-polarized and a significant PA swing is present across the Hα profile. Furthermore, some equatorial objects display double-peaked polarized flux profiles as a result of Doppler shifts. Those objects which displayed low polarization percentage of the core as well as high PA swing were classified as equatorial objects.

Objects classified as null/interstellar were those which had little to no polarization features in

the Hα region. These objects differ from unreliable ones in that they – in most cases – had a significant signal-to-noise ratio across their spectra; they simply did not show any features in the line core. Those objects which did not have sufficient signal-to-noise ratios for their polarization were classified as unreliable. Finally, objects which did not fall into any of these categories outright (either through complicated or strange spectra) were left uncategorized.

5.2 Line Profile Parameters

While the ratio between the polarized flux IPV and the total flux IPV is a useful quantity, there are cases in which it is unreliable. For objects with low polarization, the IPV of the polarized flux profile calculated by the analysis code will be much larger than it likely is due to the low signal-to-noise of the measurements. In these cases, the low signal-to-noise leads to the creation of bins with very similar mean values across the entirety of the broad Hα profile. As a result, the IPV measured for these objects is a function of the width of the region rather than any actual structure. Cases in which this issue arises have been marked (*).

Similarly, the calculation of the polarized IPV is generally conducted using the binned polarized flux spectrum (see sections 4.8 and 4.7.2). In the cases where the features of the flux spectrum are large enough to influence the values of these bins, this approach can yield probability distributions that do not appear Gaussian. In these cases, we simply used the the distribution of polarized IPV values calculated using the unbinned data to find the most probable polarized IPV $\left(^{\dagger}\right)$.

Object	Total Flux Center (Å)	Pol. Flux Center (Å)	Shift (km s^{-1})	Total Flux IPV (km s^{-1})	Pol. Flux IPV (km s^{-1})	Ratio
2E 4066	6566	6582	-731	3859	3859 ± 869	1.76*
Akn 120 (E1)	6566	6573	-320	3056	3056 ± 777	1.75
Akn 120 (E2)	6563	6559	183	3200	3200 ± 320	1.14
Akn 564	6564	6567	-137	658	658 ± 275	1.53
Akn 564 (Apr03)	6563	6565	-91	736	736 ± 229	1.43
ESO 113-45	6571	6580	-411	2374	2374 ± 822	1.5
ESO 12-21	6564	6564	0	747	747 ± 275	1.65
ESO 141-35	6565	6569	-183	2837	2837 ± 549	1.16
F 51	6565	6562	137	1523	1523 ± 92	0.9
I zw 1 (Aug06)	6563	6564	-46	851	851 ± 412	1.5
I zw 1 (E1)	6563	6570	-320	874	874 ± 320	1.26
I zw 1 (E2)	6564	6564	0	827	827 ± 320	1.22

I zw 1 (Sep02)	6562	6564	-91	783	783 ± 229	1.4
IC 3599 (Apr03)	6564	6584	-914	518	518 ± 229	1.85
IRAS 17002+5153	6562	6579	-777	2058	2058 ± 641	1.95
KUG 1031 (Apr03)	6563	6557	274	725	725 ± 275	1.64
Mrk 1239	6564	6567	-137	742	742 ± 92	1.23
Mrk 279	6566	6571	-229	2285	2285 ± 549	1.28*
Mrk 290	6566	6566	0	2025	2025 ± 457	1.33*
Mrk 304	6565	6556	411	3052	3052 ± 823	1.83*
Mrk 335	6564	6564	0	1117	1117 ± 183	1.02
Mrk 478 Apr03	6561	6567	-274	1053	1053 ± 458	1.43
Mrk 478 Jun03	6565	6570	-229	980	980 ± 366	1.63
Mrk 486	6563	6564	-46	1233	1233 ± 92	1
Mrk 486 (Apr03)	6563	6564	-46	1233	1233 ± 92	1
Mrk 507	6563	6561	91	1004	1004 ± 138	0.82
Mrk 509 (E1)	6564	6564	0	1941	1941 ± 503	1.44
Mrk 509 (E2)	6563	6573	-457	1946	1946 ± 503	1.36
Mrk 509 (E3)	6567	6573	-274	1940	1940 ± 640	1.58
Mrk 590	6564	6559	229	2500	2500 ± 960	2.18
Mrk 6 (E1)	6570	6571	-46	3045	3045 ± 594	1.62
Mrk 6 (E2)	6569	6582	-594	3045	3045 ± 412	1.42
Mrk 705	6566	6568	-91	1307	1307 ± 640	3.57
Mrk 766	6564	6562	91	1045	1045 ± 92	0.83
Mrk 766 (Apr03)	6563	6561	91	1045	1045 ± 92	0.83
Mrk 841	6557	6560	-137	2542	2542 ± 550	1.46*
Mrk 871	6570	6567	137	1795	1795 ± 366	1.17
Mrk 876	6565	6591	-1188	4303	4303 ± 869	1.27
Mrk 915	6567	6564	137	1508	1508 ± 366	0.97
Mrk 926	6577	6574	137	2650	2650 ± 685	1.38
MS 1849.2-7832	6566	6563	137	2667	2667 ± 732	1.63
NGC 985	6576	6566	457	3104	3104 ± 411	1.04
NGC 3227	6569	6561	366	1204	1204 ± 138	0.99
NGC 3516	6567	6559	366	2400	2400 ± 731	1.69*
NGC 3783	6565	6565	0	1687	1687 ± 595	1.52
NGC 4051	6565	6561	183	739	739 ± 275	1.73
NGC 4051 (Apr03)	6564	6564	0	754	754 ± 275	1.7

NGC 4151 (Apr03)	6569	6566	137	2259	2259 $\pm$ 503	1.5
NGC 5548	6565	6576	-503	2979	2979 $\pm$ 549	1.03
NGC 6104	6593	6593	0	5214	5214 $\pm$ 1002	1.23
NGC 7213	6582	6589	-320	1383	1383 $\pm$ 320	1.38
NGC 7469 (E1)	6565	6566	-46	1456	1456 $\pm$ 412	1.54
NGC 7469 (E2)	6571	6574	-137	1367	1367 $\pm$ 274	1.07
NGC 7469 (E3)	6565	6569	-183	1327	1327 $\pm$ 412	1.55
NGC 7603	6566	6577	-503	2173	2173 $\pm$ 640	1.85
NGC 4593 (E1)	6564	6560	183	1866	1866 $\pm$ 366	1.25
NGC 4593 (E2)	6564	6558	274	1995	1995 $\pm$ 458	1.24
PB 3894	6564	6561	137	1185	1185 $\pm$ 503	1.93
QSO B	6572	6571	46	1963	1963 $\pm$ 503	1.42*
UGC 3478	6564	6562	91	799	799 $\pm$ 183	0.97*
WAS 45	6576	6576	0	1573	1573 $\pm$ 457	1.6
WAS 45 (Apr03)	6570	6564	274	2431	2431 $\pm$ 320	0.77

Table 4: Central wavelengths and IPV values for broad Hα profiles in total and polarized flux. The velocity shifts in column four was calculated by subtracting total flux centroid from the polarized flux centroid. The IPV ratio in column seven was calculated by dividing the polarized flux IPV by the total flux IPV.

5.3 Polarization Parameters

The PA spectrum of some objects exhibit erratic behavior over the profile. In some of these cases, directly measured PA swing values were unable to obtained while in others their reliability is questionable. These objects have been marked (*).

Object	Avg. PA Swing (Degrees)	Direct PA Swing (Degrees)	Continuum % Polarization	Core % Polarization	Ratio
2E 4066	15.49	61.41	0.2	0.19	0.95
Akn 120 (E1)	2.92	48.49	0.82	0.49	0.6
Akn 120 (E2)	5.07	43.32	0.66	0.4	0.61
Akn 564	5.99	30.24	0.44	0.38	0.86

Akn 564 (Apr03)	3.59	53.01	0.43	0.36	0.84
ESO 113-45	21.17	103.47	0.1	0.16	1.6
ESO 12-21	3.75	33.29	0.31	0.54	1.74
ESO 141-35	0.76	13.83	1.5	1.03	0.69
F 51	0.65	9.44	3.89	4.87	1.25
I zw 1 (Aug06)	18.62	20.14	0.66	0.36	0.55
I zw 1 (E1)	1.97	34.03	0.6	0.38	0.63
I zw 1 (E2)	3.53	26.04	0.69	0.37	0.54
I zw 1 (Sep02)	1.79	27.04	0.57	0.38	0.67
IC 3599 (Apr03)	4.82	80.45	0.28	0.22	0.79
IRAS 17002+5153	74.98	86.31	0.72	0.52	0.72
KUG 1031 (Apr03)	1.95	19.35	0.52	0.55	1.06
Mrk 1239	1.51	9.05	4.63	2.93	0.63
Mrk 279	0.81	62.48	0.54	0.1	0.19
Mrk 290	4.77	63.46	0.63	0.47	0.75
Mrk 304	5.83	42.32	0.66	0.72	1.09
Mrk 335	7.32	71.74	0.28	0.51	1.82
Mrk 478 (Apr03)	12.37	93.73	0.22	0.12	0.55
Mrk 478 (Jun03)	19.57	86.68	0.19	0.12	0.63
Mrk 486	26.97	22.14	2.04	1.66	0.81
Mrk 486 (Apr03)	26.97	22.14	2.04	1.66	0.81
Mrk 507	0.05	7.74	1.73	2.68	1.55
Mrk 509 (E1)	1.24	30.05	0.95	0.63	0.66
Mrk 509 (E2)	2.06	27.63	1.09	0.52	0.48
Mrk 509 (E3)	3.37	33.23	0.87	0.54	0.62
Mrk 590	9.89	82.99	0.61	0.22	0.36
Mrk 6 (E1)	5.72	35.76	1.55	0.89	0.57
Mrk 6 (E2)	7.35	32.81	1.15	0.91	0.79
Mrk 705	5.79	52.78	0.78	0.49	0.63
Mrk 766	0.4	4.86	2.77	2.53	0.91
Mrk 766 (Apr03)	0.4	4.86	2.77	2.53	0.91
Mrk 841	2.38	48.99	1.34	0.6	0.45
Mrk 871	0.95	42.18	0.48	0.52	1.08
Mrk 876	4.54	45.96	0.72	0.51	0.71
Mrk 915	6.91	56.51	0.3	0.43	1.43

Mrk 926	11.54	61.14	0.09	0.13	1.44
MS 1849.2-7832	6.76	40.34	2.18	1.45	0.67
NGC 985	5.55	38.12	1.02	0.75	0.74
NGC 3227	1.26	8.98	0.74	0.91	1.23
NGC 3516	2.63	55.32	0.37	0.09	0.24
NGC 3783	3.36	64.08	0.49	0.37	0.76
NGC 4051	4.34	64.04	0.7	0.4	0.57
NGC 4051 (Apr03)	1.78	18.7	0.71	0.42	0.59
NGC 4151 (Apr03)	16.69	68.25	0.59	0.33	0.56
NGC 5548	2.6	43.04	0.79	0.24	0.3
NGC 6104	33.51	66.95	3.25	0.3	0.09
NGC 7213	74.93	63.41	0.2	0.13	0.65
NGC 7469 (E1)	2.04	36.13	0.07	0.11	1.57
NGC 7469 (E2)	29.94	64.95	0.25	0.11	0.44
NGC 7469 (E3)	17.34	53.64	0.23	0.09	0.39
NGC 7603	0.35	44.26	0.21	0.22	1.05
NGC 4593 (E1)	0.55	44.13	0.1	0.46	4.6
NGC 4593 (E2)	2.67	52.23	0.14	0.36	2.57
PB 3894	71.75	84.69	0.54	0.16	0.3
QSO B	13.61	33.99	3.82	1.19	0.31
UGC 3478	2.24	64.15	1.12	1.09	0.97
WAS 45	5.96	25.1	0.83	1.76	2.12
WAS 45 (Apr03)	0.44	19.85	1.12	1.85	1.65

Table 5: Various polarization-related values. The "direct PA swing" measurements in column three are absolute values (since only the magnitude of the swing is pertinent). The ratio in column six was calculated by dividing the core polarization percentage by the continuum polarization percentage.

6 Discussion

The results achieved throughout this study allow us to test several hypotheses regarding AGN. One goal is to discover whether there is supporting evidence for the two-component scattering model (see chapter 3). Though we have already utilized the model when selecting our classifications, separations between the two classifications should be pervasive in our results.

Furthermore, our data can be utilized to find relationships across our sample which map directly to physical processes and characteristics of these AGN. One such relationship is between orbital velocity and luminosity, which should provide insight to the luminosity dependence of both AGN accretion rate and the orbital dynamics of the region close to the SMBH.

We also aim to use IPV values to determine the inclination of these objects. We expect systematic differences between equatorial- and polar-class objects (in support for the two-component scattering model), and can use the calculated inclinations to determine the masses of the SMBHs within our equatorial-class objects.

Finally, we look to compare the velocity centroids of the total and polarized flux profiles. This comparison will provide insight to the inner dynamics of the scattering regions, indicating whether bulk motion of the scatterers and/or emission disk is present.

6.1 Polarized IPV Versus Luminosity

The luminosity of an AGN is assumed be some fraction of the system's Eddington luminosity:

$$L_{AGN} = f L_{Edd} \tag{70}$$

where f is the fraction of the Eddington luminosity at which the AGN radiates. The Eddington luminosity is related to the mass of the central SMBH, and using this relationship with equation 70 we find

$$L_{AGN} = f \left(\frac{4\pi G c m_p}{\sigma_e} \right) M_\bullet \tag{71}$$

where

G : Universal gravitational constant

c : Speed of light

m_p : Mass of a proton

σ_e : Electron scattering cross-section

This luminosity can be related to the radius of the BLR via the BLR ionization parameter, U:

$$U = \frac{Q}{4\pi r_{BLR}^2 nc} \tag{72}$$

where

Q : Ionizing photon luminosity

r_{BLR} : Radius of the BLR

n : Gas density of the BLR

This quantity represents the ratio between ionizing photons and gas density at a distance r_{BLR} from the central source. Effectively, it describes the ionization state of the BLR gas (Netzer 2008)

For a given spectral energy distribution, the ionizing photon luminosity is proportional to the AGN luminosity:

$$Q = \xi \left(\frac{L_{AGN}}{h\nu_H} \right) \tag{73}$$

In this relationship, $h\nu_H$ represents the energy of photons at the Lyman limit, and ξ represents the fraction of photons produced by the AGN which are ionizing. The value of ξ is dependent on the object's spectral energy distribution, but typically has a value $\sim$1. Using this in conjunction with equation 72, we achieve an expression for the BLR radius:

$$r_{BLR} = \left(\frac{\xi}{4\pi ncUh\nu_H} \right)^{1/2} L_{AGN}^{1/2} \tag{74}$$

From the virial theorem (assuming that the dynamics of the BLR clouds are dominated by the

gravitational potential of the SMBH):

$$v = \Upsilon \left(\frac{GM_{\bullet}}{r_{BLR}} \right)^{1/2} \tag{75}$$

Here, Υ is the virial factor. This factor has a value of order unity and accounts for the geometry and detailed dynamics of the BLR (Peterson et al. 2004). Substituting for M_{BH} (via equation 71) and r_{BLR} (via equation 74), we find a relationship between the velocity dispersion and the AGN luminosity:

$$v = \Upsilon L^{1/4} f^{-1/2} \left(\frac{\sigma_e}{m_p} \right)^{1/2} \left(\frac{Unh\nu_H}{4\pi c\xi} \right)^{1/4} \tag{76}$$

An empirical relationship between the BLR radius and the luminosity of the AGN ($r_{BLR} \propto L_{AGN}^{1/2}$) has been established via reverberation mapping (Bentz et al. 2009). This indicates that none of U, n, nor ξ are strongly dependent on the luminosity of the AGN (via equation 74). It is, however, possible that the virial factor (Υ) and/or the Eddington ratio (f) are strong functions of luminosity. This allows us to simplify our expression:

$$v \propto \Upsilon f^{-1/2} L_{AGN}^{1/4} \tag{77}$$

In general, the IPV should be a good indicator of the velocity dispersion of the scattering region. Thus,

$$\text{IPV}_{\text{Pol}} \propto \Upsilon f^{-1/2} L_{AGN}^{1/4} \tag{78}$$

Taking the logarithm of this relationship allows us to re-frame it in a linear form:

$$\log(\text{IPV}_{\text{Pol}}) = \frac{1}{4} \log(L) + \log(k\Upsilon f^{-1/2}) \tag{79}$$

where

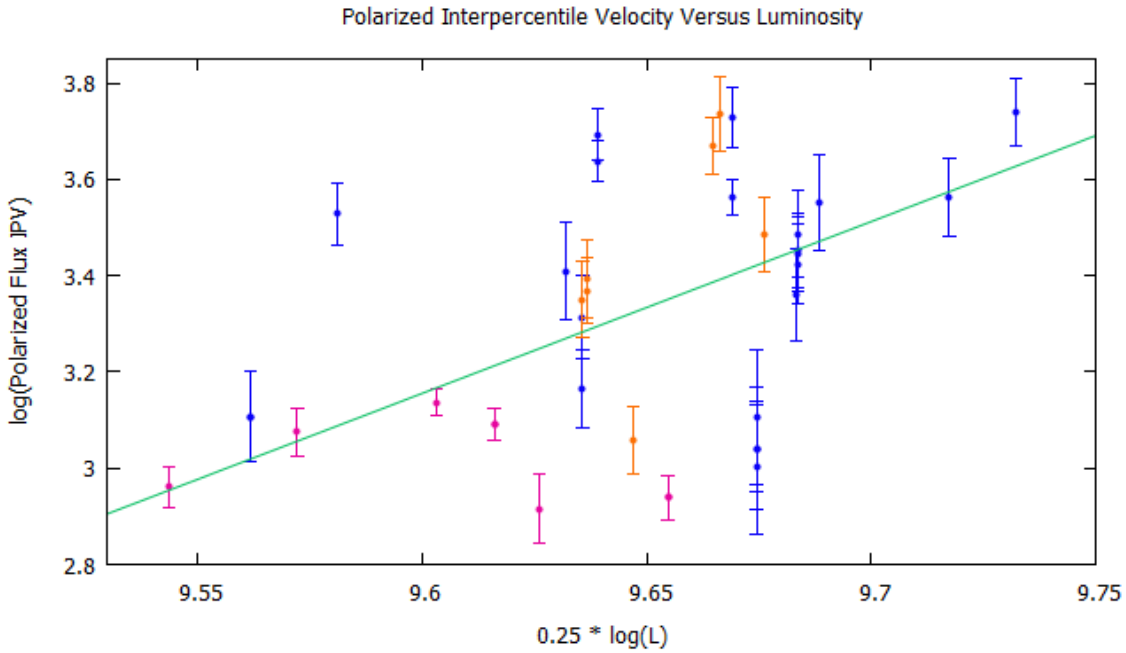

Figure 27: Logarithm of the polarized flux IPV versus one-quarter of the logarithm of the luminosity for various objects. The blue dots represent equatorial-class objects, the pink dots represent polar-class objects, and the orange dots represent objects with no clear class. The plotted line is the line of best fit for these data.

$$k = \left(\frac{\sigma_e}{m_p}\right)^{1/2} \left(\frac{Unh\nu_H}{4\pi c\xi}\right)^{1/4} \tag{80}$$

Under our analytical uncertainty propagation (see equation 52),

$$\delta \log(\text{IPV}_{\text{Pol}}) = \frac{\delta(\text{IPV}_{\text{Pol}})}{\text{IPV}_{\text{Pol}}} \frac{1}{\ln(10)} \text{km s}^{-1} \tag{81}$$

If the virial factor and the Eddington ratio are not strongly dependent on the AGN luminosity, we expect to find a linear relationship with a slope of order unity (see figure 27).

The line of best fit is given by

$$\log(\text{IPV}_{\text{Pol}}) = (3.6 \pm 1.0)\left(\frac{1}{4}\log(L)\right) - (31 \pm 10) \tag{82}$$

In this fit, the coefficient of $\frac{1}{4}\log(L)$ has units of km s^{-1} W^{-1} and the constant term has units of

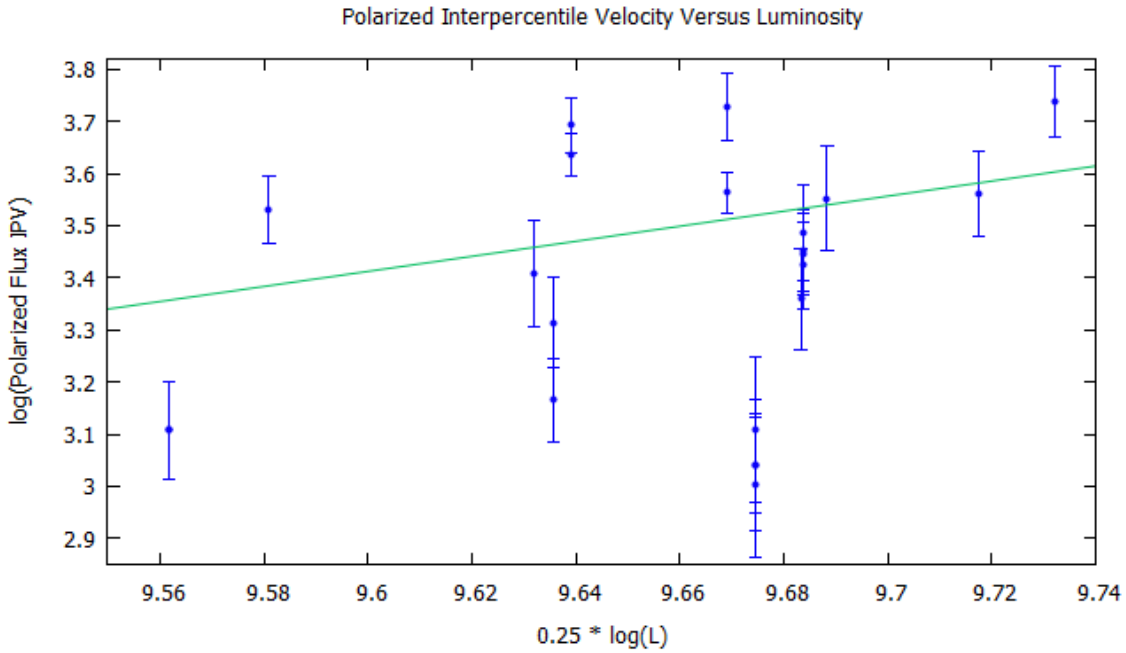

Figure 28: Logarithm of the polarized flux IPV versus one-quarter of the logarithm of the luminosity for our equatorial-class objects. The plotted line is the line of best fit for these data.

km s^{-1}. The units of this coefficient and constant term are the same for all subsequent fits in this section.

This fit had a reduced chi-squared value of $\chi^2 = 15.57$.

This extremely poor fit is indicative of three main possibilities. The first is that there is no significant correlation between the polarized flux IPV and the luminosity of the AGN. Another is that the polarized IPV and the orbital velocity of the scatterers are not as simply related as was presumed. It is possible that the relationship between the virial factor and/or the Eddington ratio is more complex than a simple polynomial correlation. Finally, there may be a significant non-Kerplerian component to the kinematics of the BLR clouds, which would invalidate equation 74.

If we limit our fit to only equatorial-class objects, we should be able to eliminate some of the discrepancies listed above. Firstly, the polar scattering regions do not have Keplerian orbits like the equatorial regions because they are located along the axis of rotation (see section 3.1). Furthermore, polar-class objects will "see" the emission disk face-on, unlike the equatorial region which "sees" the disk edge-on. Observing the emission disk from this face-on perspective, only a portion of the Keplerian velocity field is sampled by the polar region. Upon limiting our sample size, we achieve the fit shown in figure 28.

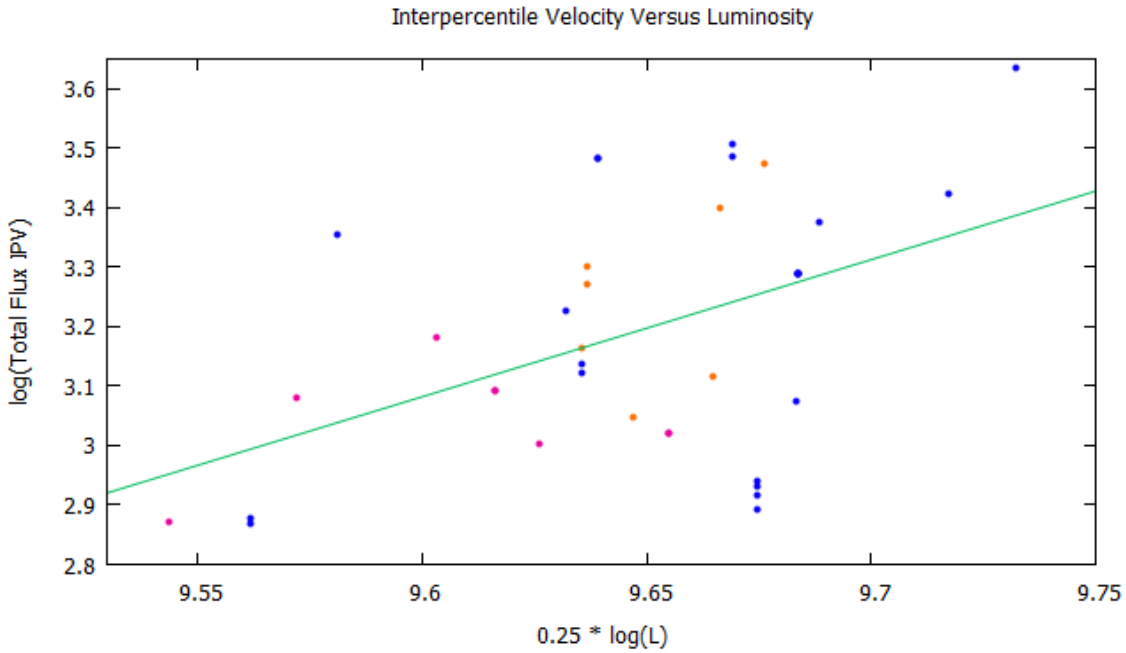

Figure 29: Logarithm of the total flux IPV versus one-quarter of the logarithm of the luminosity for various objects. The blue dots represent equatorial-class objects, the pink dots represent polar-class objects, and the orange dots represent objects with no clear class. The plotted line is the line of best fit for these data.

The line of best fit is given by

$$\log(\mathrm{IPV}_{\mathrm{Pol,\,Eq}}) = (1.4 \pm 1.1)\left(\frac{1}{4}\log(L)\right) - (10 \pm 11) \tag{83}$$

This fit had a reduced chi-squared value of $\chi^2 = 8.09$.

While this fit is consistent with our predictions, the scatter and uncertainty in the data are high and the fit itself is still extremely poor. Because of this, we are unable to learn anything useful about the values of the virial factor and/or Eddington ratio from these data.

Analysis of the total flux IPV and luminosity relationship provided similar insights (see figures 29 and 30)

The best fit lines for these cases are given by

$$\log(\mathrm{IPV}) = (2.3 \pm 0.8)\left(\frac{1}{4}\log(L)\right) - (19 \pm 8) \tag{84}$$

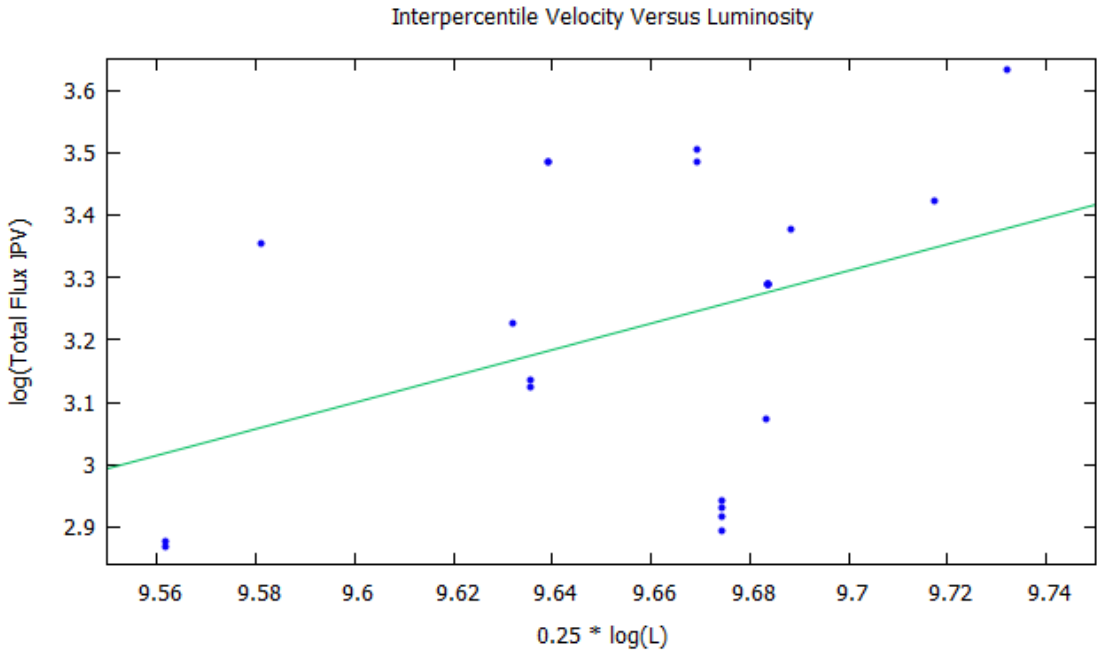

Figure 30: Logarithm of the total flux IPV versus one-quarter of the logarithm of the luminosity for our equatorial-class objects. The plotted line is the line of best fit for these data.

$$\log(\text{IPV}_{\text{Eq}}) = (2.1 \pm 1.2)\left(\frac{1}{4}\log(L)\right) - (17 \pm 11) \tag{85}$$

and had reduced chi-squared values of $\chi^2 = 0.04$ and $\chi^2 = 0.05$ respectively.

6.2 Polarized IPV Versus Total IPV

The equatorial scattering model posits that the broad lines observed in the spectra of AGN are a result of the BLR clouds (which produce the broad Hα lines) being situated in a Keplerian disk. Under this assumption, the polarized IPV should be directly proportional to the Keplerian velocity in the case of equatorial scattering:

$$\text{IPV}_{\text{Pol}} \propto v_k \tag{86}$$

The polarized flux IPV is not influenced by the inclination of the system, as the entire scattering structure is coaxial with the emission disk, "seeing" it edge-on. On the other hand, the IPV of the

total flux profile is influenced by the inclination of the system (i):

$$\text{IPV}_{\text{Total}} \propto v_k \sin(i) \tag{87}$$

If we look at the ratio of these two IPVs,

$$\frac{\text{IPV}_{\text{Pol}}}{\text{IPV}_{\text{Total}}} \propto \frac{v_k}{v_k \sin(i)} \tag{88}$$

we can see that they should relate to each other through a factor of $\sin(i)$:

$$\frac{\text{IPV}_{\text{Pol}}}{\text{IPV}_{\text{Total}}} \propto \frac{1}{\sin(i)} \tag{89}$$

If we presume that the proportionality constants in both equation 86 and 87 are equivalent, we find

$$\frac{\text{IPV}_{\text{Pol}}}{\text{IPV}_{\text{Total}}} = \frac{1}{\sin(i)} \tag{90}$$

This relationship indicates that value of the IPV ratios for our objects should be distributed on either side of a line of best fit, due to the $1/\sin(i)$ proportionality. Due to the fact that polar objects are viewed at higher inclinations, the ratio of their polarized IPV to their total IPV should be lower than those of equatorial objects (and the sample at large). Thus, we can conclude that polar-class objects should lie preferentially below this line. Figure 31 shows confirmation for these expectations.

Our data show this relationship very well with only two polar-class objects (Mrk 1239 and WAS45) located above the line of best fit (to all objects) given by

$$\text{IPV}_{\text{Pol}} = (1.06 \pm 0.04) \cdot (\text{IPV}) \tag{91}$$

This fit had a reduced chi-squared value of $\chi^2 = 2.81$. The poor quality of the fit is not unexpected: the theory suggests that the equatorial-class and polar-class objects should diverge.

The two polar-class objects located above the line of best fit display interesting properties. Mrk

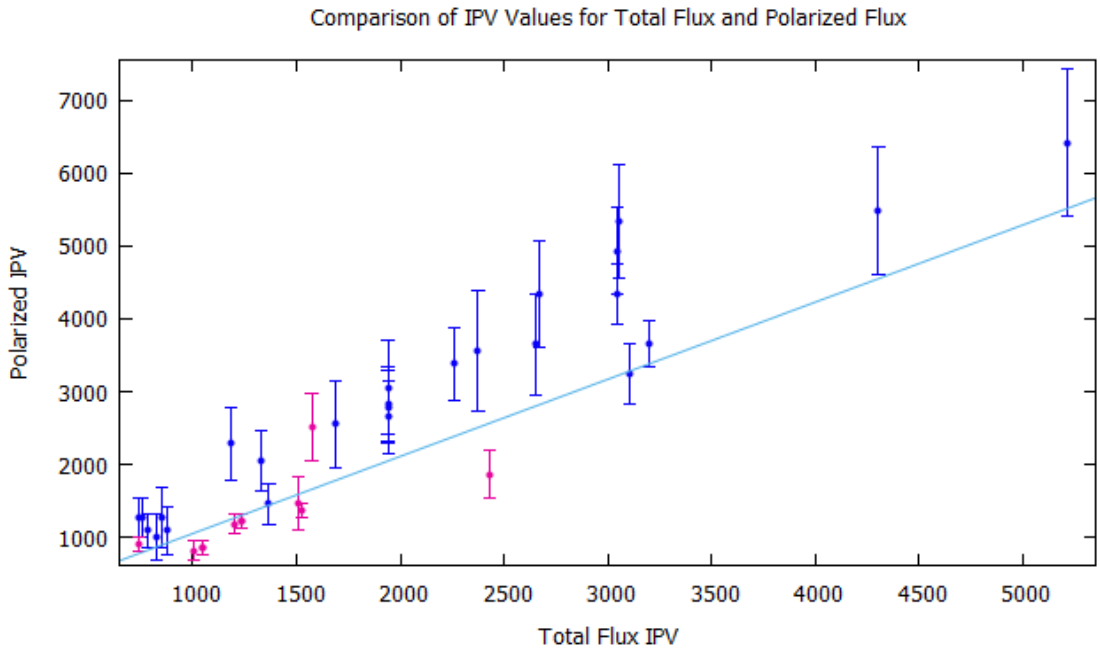

Figure 31: Polarized IPV Versus total IPV for our sample. The blue dots represent equatorial-class objects and the pink dots represent polar-class objects (each with their associated uncertainty in polarized IPV). The plotted line is the line of best fit for these data. The two pink dots above the line of best fit are Mrk 1239 and WAS 45 from left to right respectively.

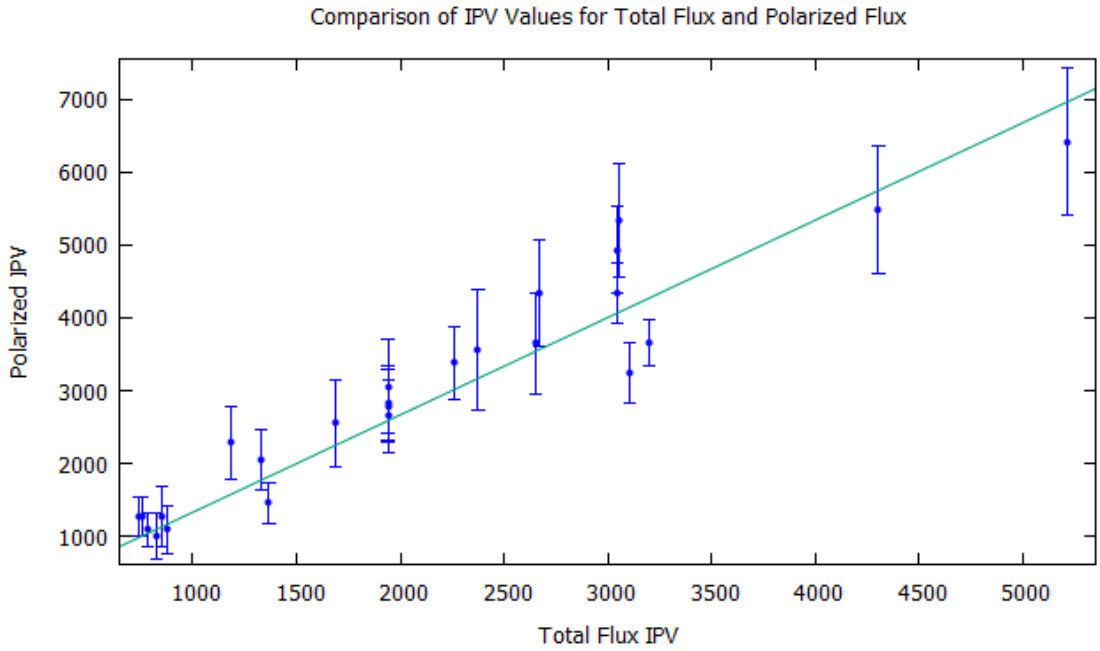

Figure 32: Polarized IPV Versus total IPV for our equatorial-class objects. The plotted line is the line of best fit for these data.

1239 displays extreme polarization signatures which differentiate it from the rest of our sample (see section A.1). WAS 45, on the other hand, shows very fine structure in its post-subtraction polarization spectrum, likely due to the attempts to remove strong narrow-line features in the subtraction process (see section A.2).

Looking at each population individually, we should observe a larger proportionality constant for equatorial-class objects in tandem with a lower proportionality constant for polar-class objects. The fits achieved in these cases are shown in figures 32 and 33 and are given by the following fits respectively:

$$\text{Equatorial: } \text{IPV}_{\text{Pol}} = (1.33 \pm 0.04) \cdot (\text{IPV}) \tag{92}$$

$$\text{Polar: } \text{IPV}_{\text{Pol}} = (0.91 \pm 0.03) \cdot (\text{IPV}) \tag{93}$$

These fits had reduced chi-squared values of $\chi^2 = 0.47$ and $\chi^2 = 0.56$ respectively.

Each of these results are in line with the expected trend, given that polar-class objects lay significantly below equatorial-class objects.

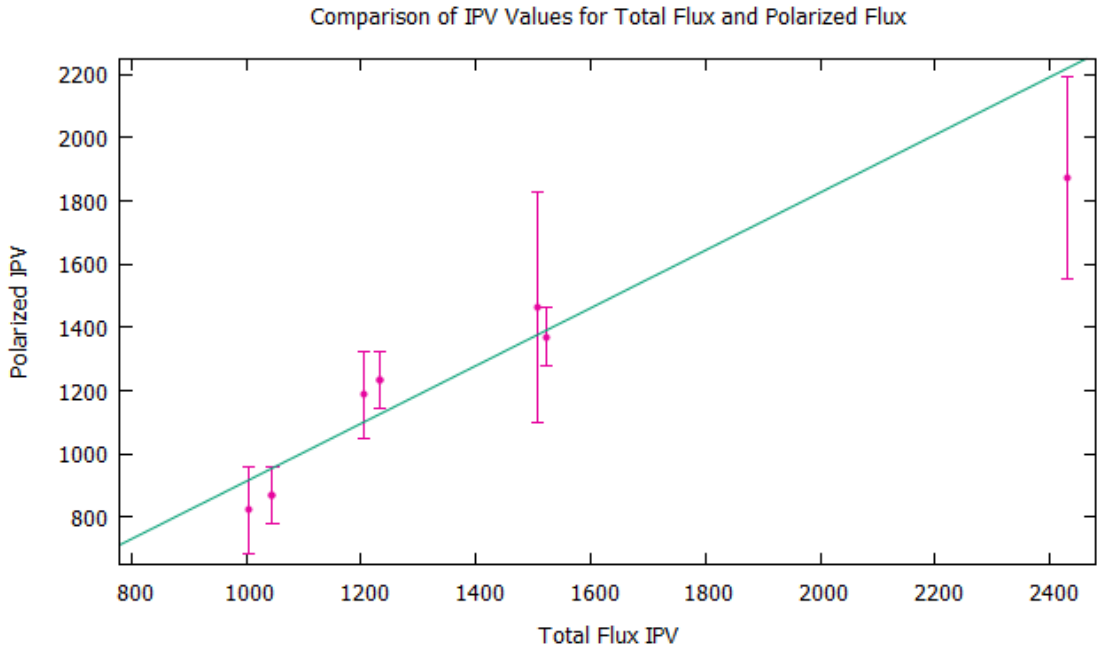

Figure 33: Polarized IPV Versus total IPV for our polar-class objects. The plotted line is the line of best fit for these data. Mrk 1239 and WAS45 were omitted from both the plot and regression.

6.2.1 Mass Estimates of the Central Source

The inclination extracted via the above analysis is instrumental in the estimation of the mass of the central SMBH ($m_\bullet$). Assuming the BLR can be modeled as a Keplerian disk with a radius of r_{BLR}, we know that the velocity (v_k) of the orbiting body is given by

$$v_k{}^2 = \frac{GM_\bullet}{r_{BLR}} \tag{94}$$

This relationship is not immediately useful however, as there is no direct method to measure the Keplerian velocity for an arbitrarily inclined disk. Instead, we must relate the line-of-sight velocity to the Keplerian velocity via the inclination. For a disk of inclination i (where $i = 0^\circ$ indicates a face-on orientation) the line-of-sight and Keplerian velocities are related through

$$v = v_k \sin(i) \tag{95}$$

Using this in conjunction with equation 94 yields an equation for the mass of the central SMBH:

$$M_\bullet = \frac{r_{BLR} v^2}{G \sin^2(i)} \tag{96}$$

In this equation, v is representative of the velocity dispersion rather than the orbital velocity itself. Other similar results in the literature are found using the FWHM of the broad-line profile rather than the IPV. For a Gaussian distribution, the FWHM is approximetly twice that of the IPV. In order to allow for comparison to SMBH masses found in other sources, we will use twice the IPV in place of the velocity dispersion:

$$v = 2\text{IPV} \tag{97}$$

Thus,

$$M_\bullet = \frac{4 r_{BLR} (\text{IPV})^2}{G \sin^2(i)} \tag{98}$$

The radius of the BLR is directly related to the object's luminosity. As was the case when determining the bolometric luminosity of objects in our sample (see section 4.2), we can utilize the 2-10keV X-ray fluxes from NED in conjunction with an empirical correction (Greene et al. 2010) to determine the BLR radius for each object:

$$\frac{r_{BLR}}{10} = (0.09 \pm 0.05) + (0.52 \pm 0.05) \log\left(\frac{L_{2-10\text{keV}}}{10^{36}\text{W}}\right) \tag{99}$$

It is important to note that this model of BLR radius has one major issue when it comes to some objects in our sample. Due to the nature of the logarithmic term, objects with 2-10keV X-ray luminosities significantly lower than 10^{36}W will produce a negative value for the BLR radius. Objects for which this are the case have been omitted from this analysis.

The associated uncertainty of the radii produced by this model follows from 52:

$$\frac{\delta r_{BLR}}{10} = \sqrt{(0.05)^2 + \left[(0.05) \log\left(\frac{L_{2-10\text{keV}}}{10^{36}\text{W}}\right)\right]^2} \tag{100}$$

The luminosities in our sample were of order $L_{2-10\text{keV}} = 5 \cdot 10^{36}$ W, which yields BLR radii of

order $r_{BLR} = 5$ light days (or $r_{BLR} = 1 \cdot 10^{14}$m). Results of our previous analysis yielded an average value for $1/\sin(i)$ of approximately 1.33 (see equation 92) while the IPV values in across our equatorial-class objects were of order IPV $= 2 \cdot 10^3$km/s (or IPV $= 2 \cdot 10^6$m/s). This leads to an estimated average black hole mass of $m_\bullet = 1 \cdot 10^{37}$kg or $m_\bullet = 5 \cdot 10^6 M_\odot$. This value is consistent with measurements of similar objects.

For equatorial-class objects, the value of $1/\sin(i)$ is directly related to the IPV ratio (see equation 90). By using this in conjunction with equation 98, we can formulate a mass estimation which includes only measurements directly taken in this study:

$$M_\bullet = \frac{4 r_{BLR} (\text{PIPV})^2}{G} \tag{101}$$

These masses have uncertainties which again follow from equation 52:

$$\delta M_\bullet = \frac{4\text{PIPV}}{G} \sqrt{\left[(\text{PIPV})(\delta r)\right]^2 + \left[2r(\delta \text{PIPV})\right]^2} \tag{102}$$

Applying these calculations to a subset of our equatorial-class objects yielded the results displayed in table 6.

Object	SMBH Mass (Solar Masses)	Literature Estimates (Solar Masses)	Reference	Percent Discrepancy
Akn 120 (E1)	$(7.9 \pm 2.7) \cdot 10^7$	$2.2 \cdot 10^8$	(Bentz & Katz 2015)	-64
Akn 120 (E2)	$(3.7 \pm 0.9) \cdot 10^7$			-83
ESO 113-45	$(4.9 \pm 2.3) \cdot 10^7$	$1.3 \cdot 10^8$	(Bentz & Katz 2015)	-62
1 zw 1 (Aug06)	$(5.0 \pm 3.4) \cdot 10^6$			
1 zw 1 (E1)	$(3.7 \pm 2.3) \cdot 10^6$			
1 zw 1 (E2)	$(3.1 \pm 2.1) \cdot 10^6$			
1 zw 1 (Sep02)	$(3.7 \pm 1.6) \cdot 10^6$			
Mrk 6 (E1)	$(2.6 \pm 1.2) \cdot 10^7$	$(3.27 \pm 0.04) \cdot 10^7$	(Doroshenko et al. 2012)	-21
Mrk 6 (E2)	$(2.0 \pm 0.9) \cdot 10^7$			-39
Mrk 509 (E1)	$(2.8 \pm 1.1) \cdot 10^7$	$2.4 \cdot 10^8$	(Bentz & Katz 2015)	-88
Mrk 509 (E2)	$(2.5 \pm 1.1) \cdot 10^7$			-90
Mrk 509 (E3)	$(3.3 \pm 1.5) \cdot 10^7$			-86
Mrk 876	$(1.9 \pm 0.7) \cdot 10^8$	$4.9 \cdot 10^8$	(Bentz & Katz 2015)	286
Mrk 926	$(7.3 \pm 2.9) \cdot 10^7$	$1.12 \cdot 10^8$	(Kollatschny & Zetzl 2010)*	35

NGC 3783	$(4.4 \pm 3.3) \cdot 10^6$	$(5.42 \pm 0.99) \cdot 10^6$	(Bentz & Katz 2015)	-74
NGC 7469 (E2)	$(1.9 \pm 1.1) \cdot 10^6$	$(2.21 \pm 0.25) \cdot 10^6$	(Peterson et al. 2004)	-14
NGC 7469 (E3)	$(3.8 \pm 2.3) \cdot 10^6$			70
PB 3894	$(1.9 \pm 0.9) \cdot 10^7$	$(2.66 \pm 0.80) \cdot 10^7)$	(Peterson et al. 2004)	-30

Table 6: SMBH mass estimations calculated using their 2-10keV luminosities. Objects were omitted if their 2-10keV luminosity fell outside the modeled region of equation 99 or the object did not have a luminosity in this band in NED (see table 2). The "literature estimate" for Mrk 926 is an upper limit on the mass rather than an estimate.

A histogram of the logarithm of our estimated masses is displayed in figure 34.

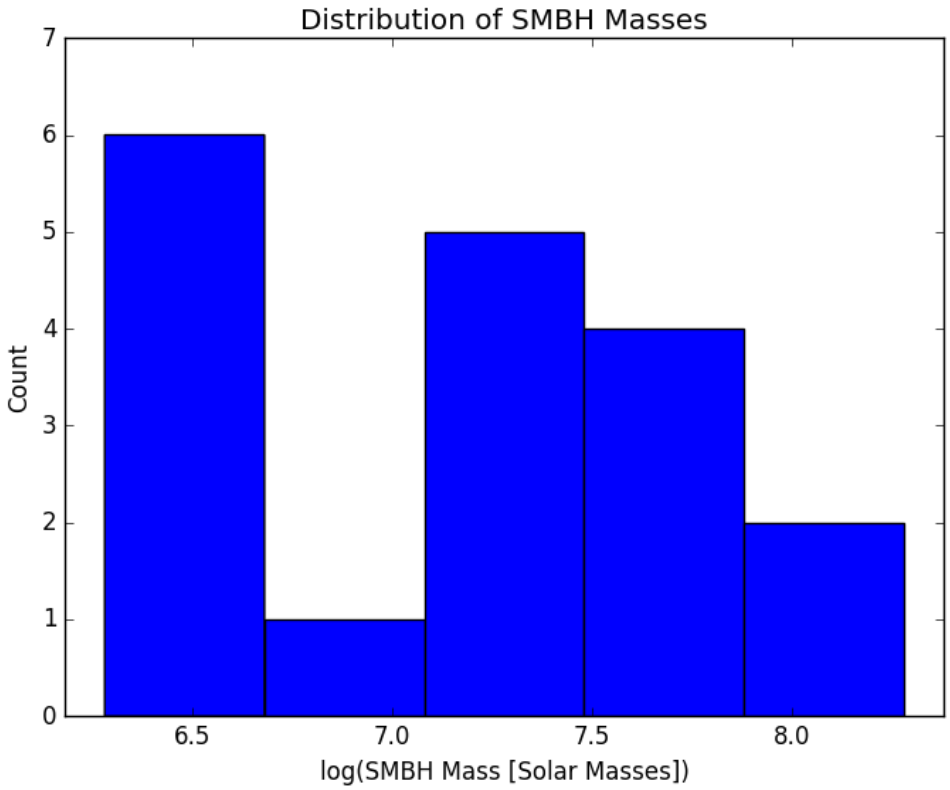

Figure 34: Distribution of SMBH masses calculated using equation 101.

The listed mass estimations from (Peterson et al. 2004) and (Doroshenko et al. 2012) in table 6 are the reported virial mass rather than the reported SMBH masses. This is to account for difference

in virial factor values between those studies and our own (both used $\Upsilon = 5.5$ while we assume $\Upsilon = 1$; see section 6.1).

This methodology does require some refinement in order to accurately compare the results with those from other sources. In general, the radius-luminosity relationship uses $L_{5100\text{Å}}$ rather than $L_{2-10\text{keV}}$. A quick estimation using this band can be achieved for the objects listed in Bentz et al. 2009 by utilizing their r_{BLR} relationship for this wavelength band,

$$\log(r_{\text{BLR}}) = (-21.3 \pm 2.9) + (0.519 \pm 0.066) \log(5100 L_{5100\text{Å}}) \tag{103}$$

and values of $L_{5100\text{Å}}$ listed in the AGN Black Hole Mass Database (Bentz & Katz 2015). If multiple luminosity measurements are presented, the average of the calculated estimated masses is reported. We can compare the estimates we formulate to updated masses found in the AGN Black Hole Mass Database.

In order to compare our estimates to these update masses, some changes needed to be made to the listed values. First, the value of Υ was set to 1 (the site provided this functionality). Furthermore, the masses were recalculated using the FWHM of the line profiles rather than their velocity dispersion (σ). The masses listed in the database were calculated using Keplerian dynamics:

$$M_{\bullet} = \Upsilon \frac{R\sigma^2}{G} \tag{104}$$

Thus, replacing σ with the FWHM changes the masses listed in the database by a square of their ratio:

$$M_{\bullet,\text{FWHM}} = \left(\frac{\text{FWHM}}{\sigma}\right)^2 M_{\bullet,\sigma} \tag{105}$$

For objects with multiple measurements of these properties, the average of the formulated masses is reported. The estimates from our method are compared to these formulated masses in table 7:

Object	Calculated SMBH Mass (Solar Masses)	Literature Estimates (Solar Masses)	Percent Discrepancy
Akn 120 (E1)	$5.8 \cdot 10^8$	$2.2 \cdot 10^8$	168
Akn 120 (E1)	$2.7 \cdot 10^8$		25

ESO 113-45	$3.1 \cdot 10^8$	$1.3 \cdot 10^8$	147
Mrk 509 (E1)	$2.4 \cdot 10^8$	$1.3 \cdot 10^8$	92
Mrk 509 (E2)	$2.2 \cdot 10^8$		74
Mrk 509 (E3)	$2.9 \cdot 10^8$		132
Mrk 876	$1.9 \cdot 10^9$	$4.9 \cdot 10^8$	287
NGC 3783	$3.1 \cdot 10^7$	$1.7 \cdot 10^7$	83

Table 7: Select SMBH mass estimations calculated using 5100Å luminosities rather than 2-10keV luminosities. Literature estimates presented here are calculated via information from the AGN Black Hole Mass Database (Bentz & Katz 2015)

For every observation, our estimated SMBH masses were higher than those listed in the literature. This is expected as the equatorial scattering region (which the polarized IPV probes) samples the entire Keplerian velocity field, whereas the FWHM does not (as a result of system inclination).

6.3 IPV Ratio Versus Polarization Ratio

Ratios involving polarized quantities tend to relate to characteristics of the system's dominating scattering source. One such relation is that polar objects are expected to have high core (corresponding to the inner 95% of the object's flux) polarization whereas equatorial objects should have lower core polarization (as described in section 5.1). As a result, the ratio of percentage polarization of the core to that that of the continuum is expected to be higher in polar dominated objects.

Furthermore, polar scattered objects should have a lower polarized IPV due to their view of the central emission disk. Since they always "see" this disk face on, the polarized IPV should be low due to the orbital velocity of the emitting elements being nearly parallel to the scattering plane. For equatorial objects, the opposite should be true (since they "see" the emitters edge-on).

Between these two effects, we should see a split in the population if we compare the ratio of the IPVs (polarized versus total) to that of the polarization percentages (core polarization versus continuum polarization). Polar objects should be preferentially located at low IPV ratios and high polarization ratios, while equatorial objects should have low polarization ratios (with variable IPV ratios due to having various orientations to the observer).

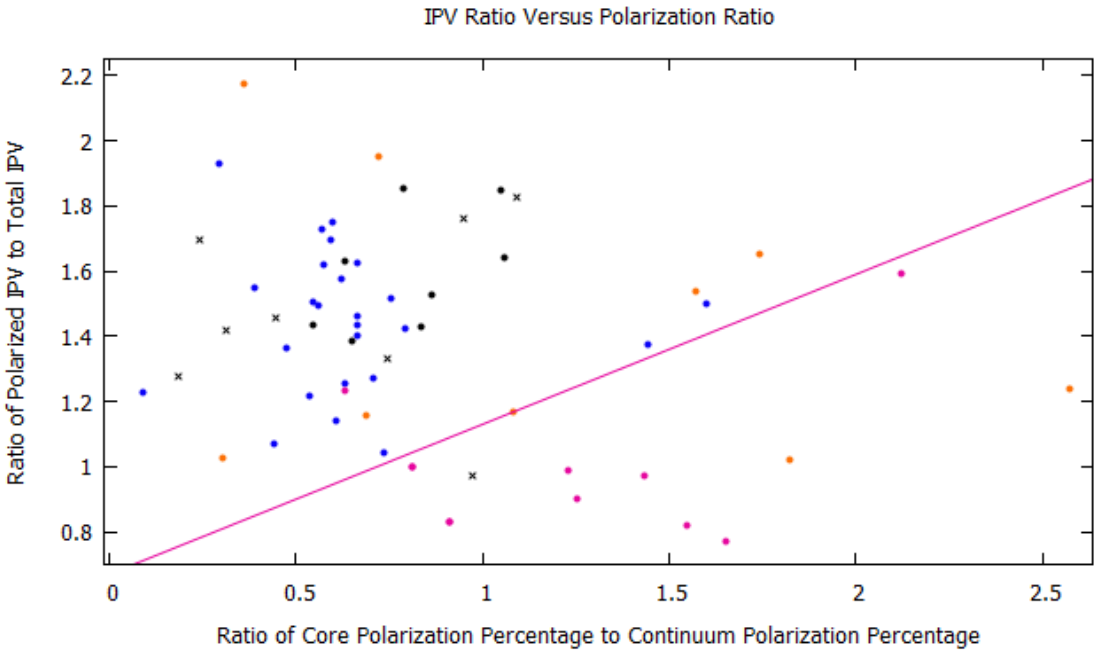

Figure 35: IPV ratio (the ratio of polarized IPV total IPV) versus polarization percentage ratio (the ratio of core polarization percentage to continuum polarization percentage) for each object in our sample. The blue dots represent equatorial-class objects, the pink dots represent polar-class objects, the black dots represent null-class objects, the orange dots represent objects with no clear class, and black crosses represent objects with unreliable spectra. The plotted pink line is the proposed split given in equation 106.

The data in our sample support this prediction rather well. A clear division appears in our distribution (see figure 35). According to these data, polarized objects occur in locations where

$$\frac{\text{IPV}_{\text{Pol}}}{\text{IPV}_{\text{Total}}} < 0.46 \left(\frac{p_{\text{Core}}}{p_{\text{Cont.}}} \right) + 0.67 \tag{106}$$

Only one polar-class object (Mrk 1239) fell significantly outside of the proposed splits.

6.4 PA Swing Versus Core Polarization

As shown in section 6.3, we would expect polar-class objects to have higher core polarization percentages than equatorial objects. This is a result of polar-class objects having narrower polarized emission lines from viewing the central emission disk face-on. This causes the polarization percentage of the core to be higher in these types of objects compared to equatorial-class objects. Furthermore, the two-component scattering model (see section 3) suggests that polar-class objects should have lower PA swings on average than equatorial-class objects due to the polar scattering region's face-on view of the emission disk. These two relationships imply that high core polarization objects will have preferentially lower PA swings and that these objects will also be polar dominated.

Our data show these two expected results nicely (see figure 36). Furthermore, the plot shows a clearly defined envelope containing all of the objects (displaying no objects of high core polarization *and* high PA swing).

Only two objects lay significantly outside of their respective populations: Mrk 915 (a polar-class object) and MS 1849.2-7832 (an equatorial-class object). We believe that the discrepancy of Mrk 915 is a result of the narrow-line emission being polarized at a significantly different polarization position angle than the continuum emission. This effect could result in artificially high PA swing measurements, which is what separates the object from the rest of its classification's objects in this analysis.

MS 1849.2-7832 is not so significantly removed from the remainder of its classification. It is possible that this is a result of the object's spectra being rather noisy, causing the calculation of of core polarization percentage to yield a larger result than anticipated.

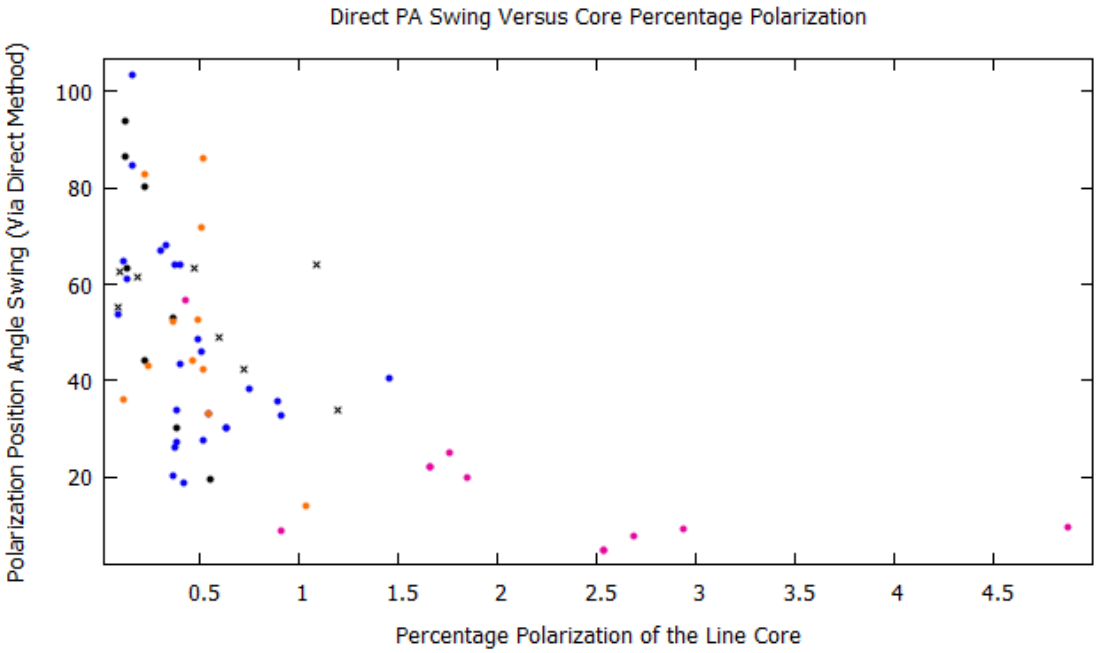

Figure 36: Polarization position angle swing measured using direct analysis (see section 4.9.2) versus average percent polarization in the Hα core. The blue dots represent equatorial-class objects, the pink dots represent polar-class objects, the black dots represent null-class objects, the orange dots represent objects with no clear class, and black crosses represent objects with unreliable spectra.

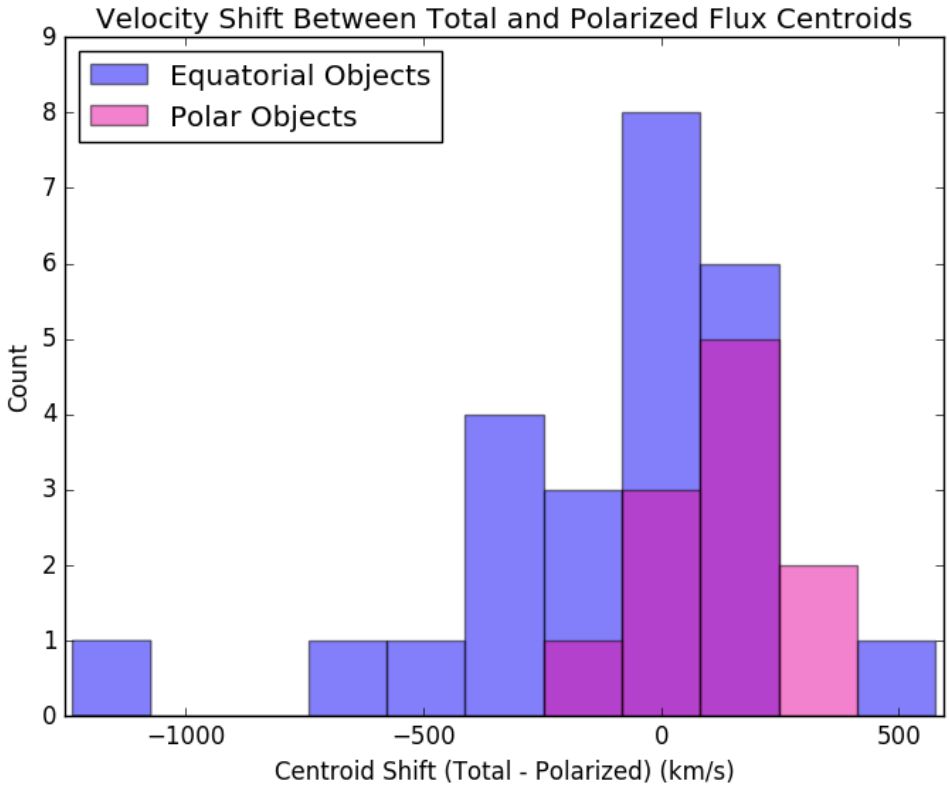

Figure 37: A histogram of velocity shifts between total and polarized flux centroids. The median values for the distributions are 0km/s for equatorial-class objects and 91.42km/s for polar-class objects.

6.5 Comparison of Flux Centroids

Comparing the centroids of the total and polarized flux profiles provides insight to the relative bulk motion of the scatterers and the emission disk. If the scatterers or the emission disk are moving relative to each other (along the line of sight of the scatterers), we would expect to see a difference in the location of the line profile centroids as a result of redshifting or blueshifting. The polarized flux spectrum would be offset from the total flux spectrum since the scatterers would "see" this relative motion.

Comparison of the centroids revealed that equatorial-class objects had their polarized flux centroid preferentially red-shifted, while polar-class objects displayed preferential blue-shifting (compared to the total flux centroid). These results are shown in figure 37.

6.6 Sample Comparisons

As discussed in section 5.1, our sample is divided into two main types of AGN: those which are dominated by equatorial scattering and those which are dominated by polar scattering. These classifications represent the difference in scattering geometries as well as the difference in the way each scattering region "sees" the emission disk. This distinction should cause the observational properties of these classes to differ, separating them into two distinct groups.

To test this, we utilized a Kolmogorov-Smirnov test (KS test) between two sets of results (for example, total IPV and polarized IPV for equatorial objects). The KS test compares the cumulative probability distribution function (CDF) of the two samples, using their maximum difference in order to determine the likelyhood that the samples are drawn from the same initial distribution.

A collection of the results detailed in this section are collected in table 8:

Samples Compared	**Maximum Difference (D)**	**p-Value (p)**
Equatorial-versus-Polar IPV Ratio	0.8182	0.0001
Equatorial-versus-Polar Total IPV	0.5491	0.0200
Equatorial-versus-Polar Polarized IPV	0.6400	0.0038
Equatorial-Class Total-versus-Polarized IPV	0.3600	0.0783
Polar-Class Total-versus-Polarized IPV	0.2727	0.8080

Table 8: Collection of the results from various KS tests on subsets of our data. The first three rows refer to comparisons between classifications while the final two are comparisons within classifications.

The p-value in this test indicates the likelyhood that the two sets are drawn from the same distribution. In general, a p-value of 0.05 suggests that the data are drawn from the same distribution, while values lower than this suggest they are not. It is important to note, however, that the p-value at which one accepts this hypothesis is dependent on the desired certainty.

6.6.1 Equatorial/Polar IPV Ratio Comparison

The IPV ratio values (the ratio of polarized IPV to total IPV) between our equatorial-class and polar-class objects should reveal a difference in their distribution. Since the equatorial and polar objects each have their own scattering geometry, it would logically follow that their polarization characteristics would differ (see section 6.2).

The KS test for these samples returned a maximum difference in the CDFs of $D = 0.8182$ which

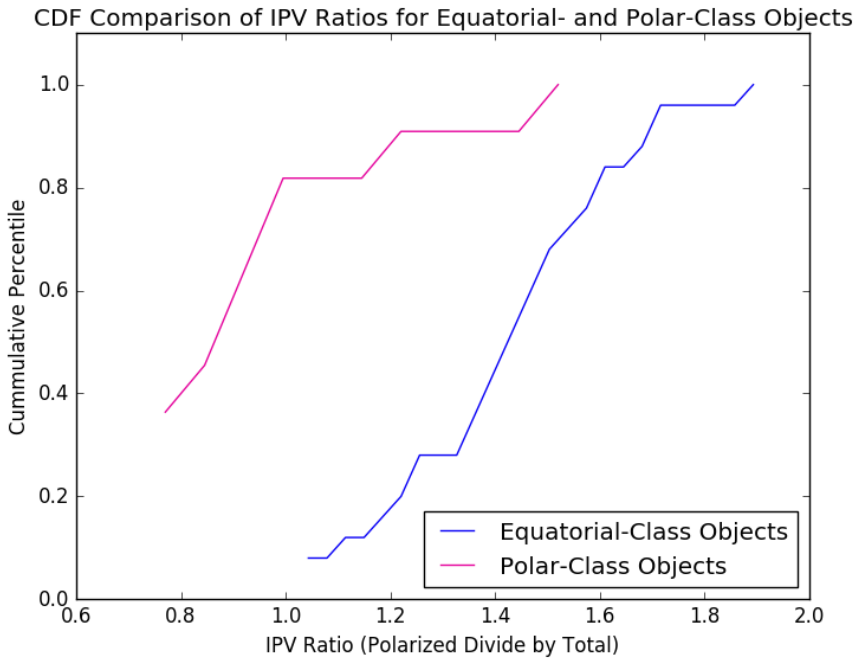

Figure 38: Cumulative distribution functions of the IPV ratios (polarized to total) for our equatorial- and our polar-class objects.

corresponds to a p-value of $p = 0.0001$ (see figure 38). Thus, it is very unlikely these two data sets are drawn from the same distribution.

6.6.2 Equatorial/Polar Total IPV Comparison

The IPV values between our equatorial and polar objects should also be systematically different since they are likely the same type of object viewed at different orientations. Equatorial dominated objects are likely viewed closer to face-on while polar dominated objects are presumed to be viewed edge-on. This difference in orientation will cause the total IPV distributions in the classes to differ.

The KS test for these samples returned a maximum difference in the CDFs of $D = 0.5491$ which corresponds to a p-value of $p = 0.0200$ (see figure 39). Thus, it is unlikely these two data sets are drawn from the same distribution.

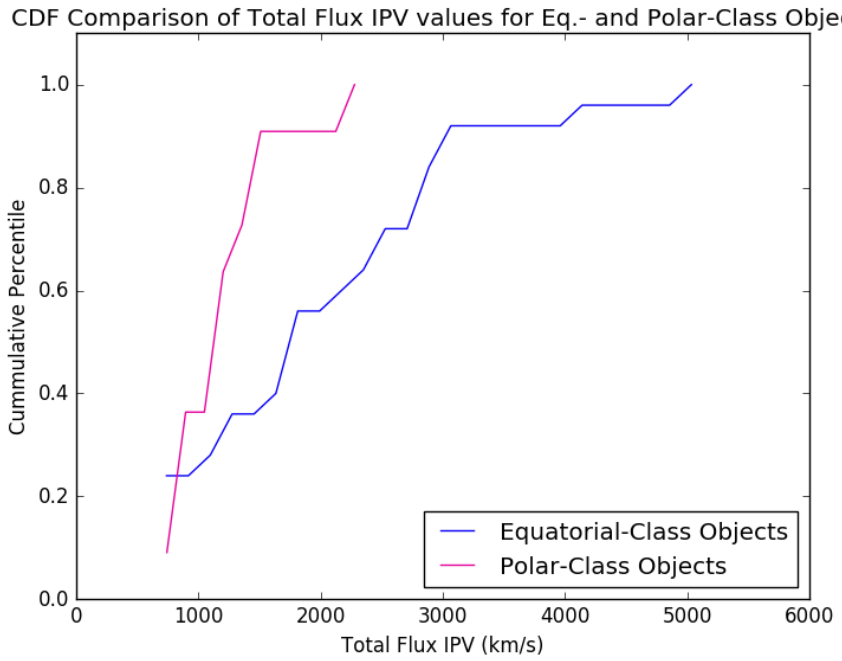

Figure 39: Cumulative distribution functions of the total IPV for our equatorial- and our polar-class objects.

6.6.3 Equatorial/Polar Polarized IPV Comparison

Following the logic of section 6.6.1, the polarized IPV values between our equatorial and polar objects should be drawn from different distributions. The KS test for these samples returned a maximum difference in the CDFs of $D = 0.6400$ which corresponds to a p-value of $p = 0.0038$ (see figure 39). Thus, it is very unlikely these two data sets are drawn from the same distribution.

6.6.4 Equatorial-Class Total/Polarized IPV Comparison

Equatorial-class objects have their primary scatterers viewing the emission disk edge-on. Furthermore, we would expect these objects to be directly observed at low inclinations (more face-on). Together, these two effects should lead to a systematically higher polarized IPV than total IPV for equatorial-class objects (see section 6.2).

The KS test between the total IPV and polarized IPV values for our equatorial objects returned a maximum difference in the CDFs of $D = 0.3600$ which corresponds to a p-value of $p = 0.0783$ (see figure 41). At this level of confidence, we conclude that these two samples are drawn from

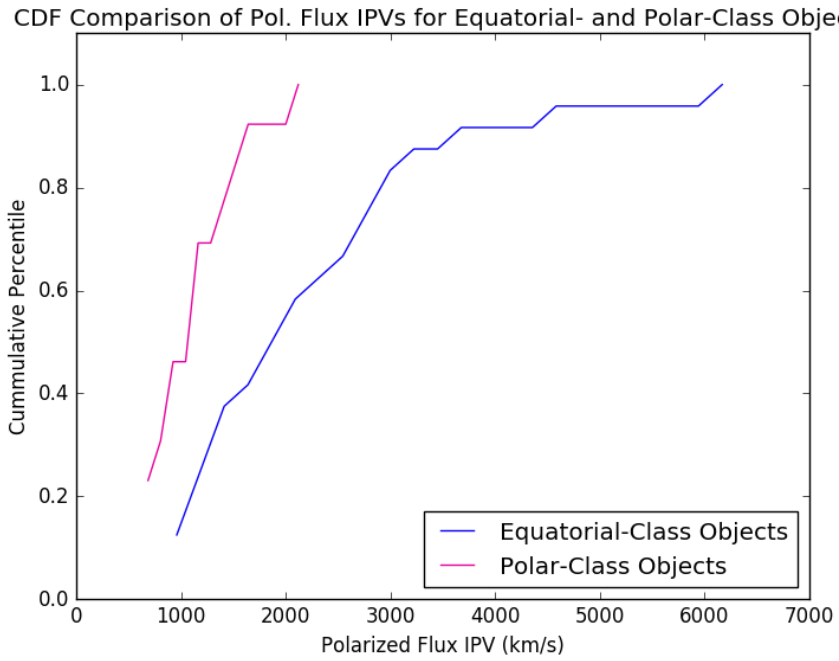

Figure 40: Cumulative distribution functions of the polarized IPV for our equatorial- and our polar-class objects.

similar, but distinctly different distributions. Furthermore, figure 41 displays the systematic difference in polarized and total IPV we expect, with the polarized IPV values being systematically higher than the total IPV values.

6.6.5 Polar-Class Total/Polarized IPV Comparison

Unlike in section 6.6.4, polar-class objects have their primary scatterers viewing the emission disk face-on. Furthermore, direct observation of the emission disk is blocked by the optically thick torus. Together, these two effects should lead to similar distributions for both total IPV and polarized IPV in these objects..

The KS test for these samples returned a maximum difference in the CDFs of $D = 0.2727$ which corresponds to a p-value of $p = 0.8080$ (see figure 39). Thus, it is very likely these two data sets are drawn from the same distribution.

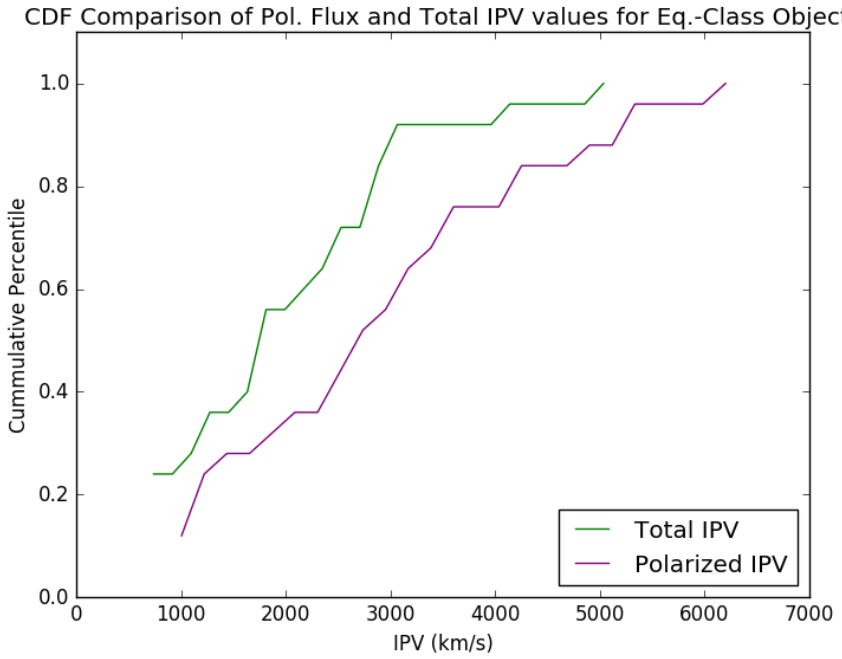

Figure 41: Cumulative distribution functions of the total IPV and polarized IPV for our equatorial-class objects

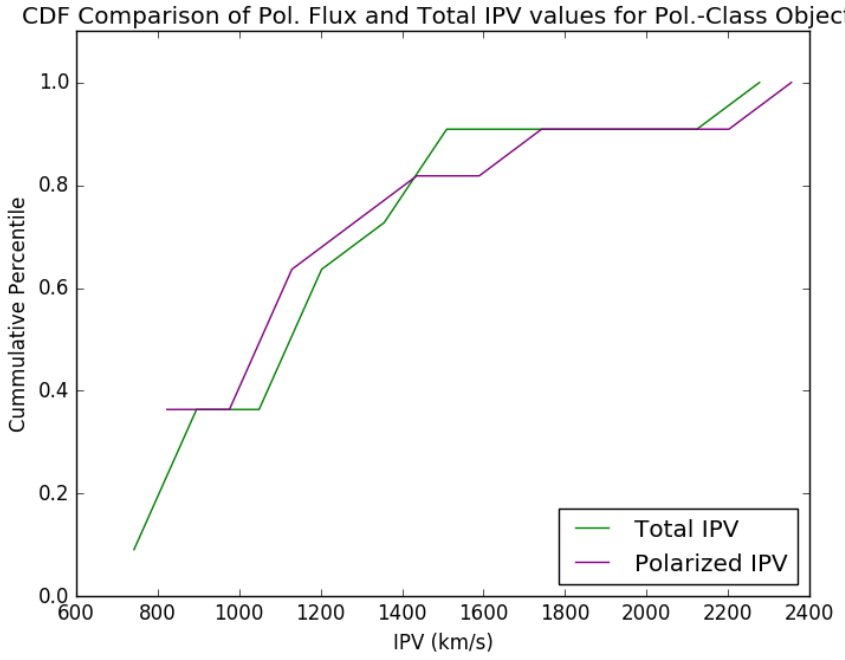

Figure 42: Cumulative distribution functions of the total IPV and polarized IPV for our polar-class objects.

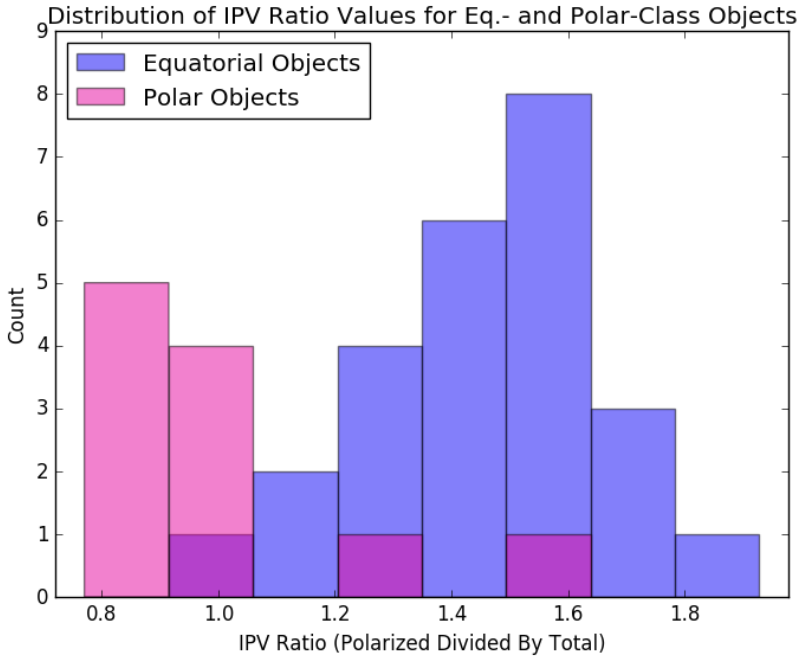

Figure 43: A histogram of IPV ratio values for our sample. The IPV ratio is defined as polarized IPV value divided by the total flux IPV value.

6.6.6 Total IPV and Polarized IPV Distributions

The results achieved in sections 6.6.1, 6.6.2, and 6.6.3 indicate that both the total flux IPV and polarized flux IPV values in our sample are drawn from different distributions. This observation is further supported by the histograms of the IPV ratio values (figure 43), the total flux IPV values (figure 44), and the polarized flux IPV values (figure 45).

In each histogram, we see a clear separation between classifications, confirming the results of the K.S. tests and section 6.2.

6.7 Major Results

The results of our study point to a clear distinction between equatorial- and polar-class objects across our sample.

Comparison of total and polarized flux IPV values show a definitive split between the two populations (see section 6.2). We found that equatorial-class objects were systematically positioned above the line of best fit to our sample as a whole (see figure 31) while polar objects were posi-

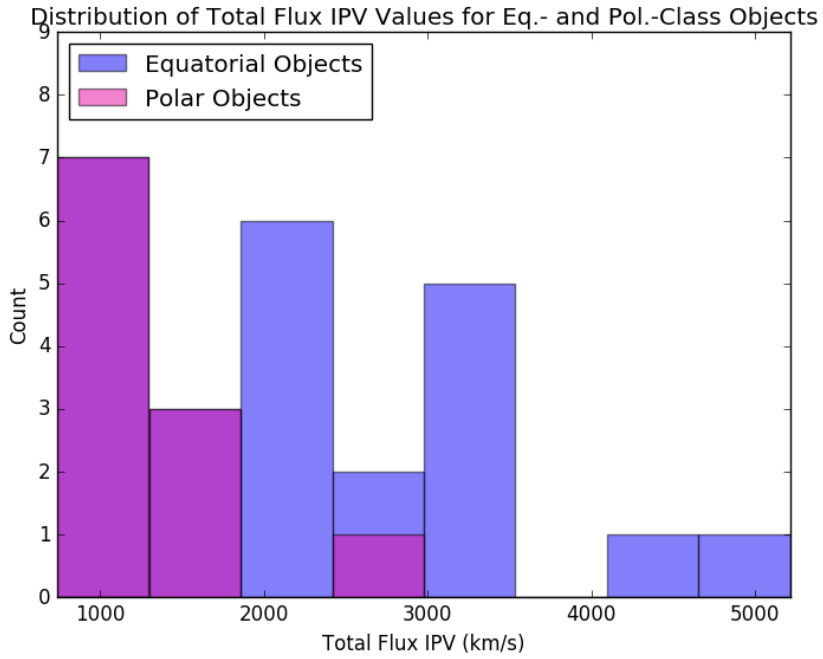

Figure 44: A histogram of total flux IPV values for our sample.

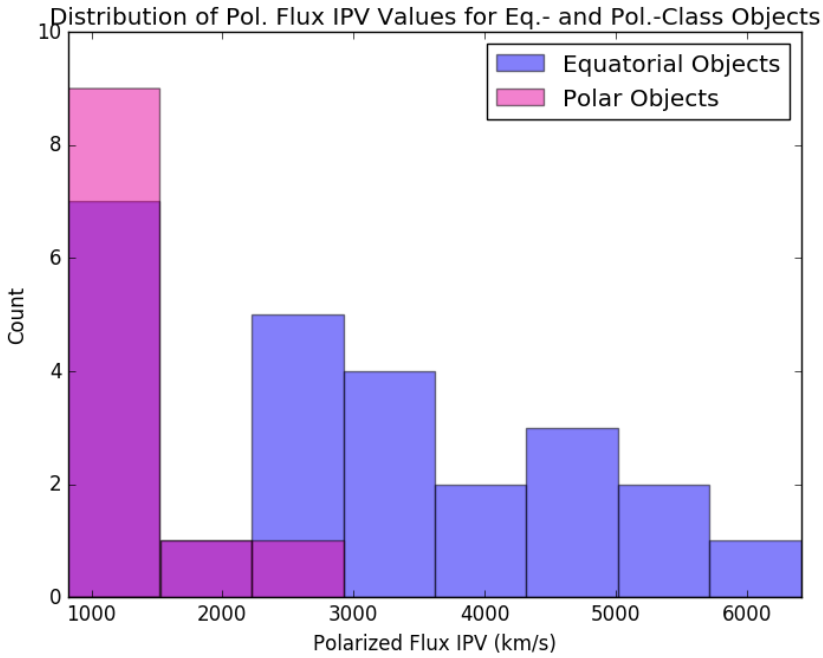

Figure 45: A histogram of total polarized IPV values for our sample.

tioned below this line. These results are further confirmed by fits to the individual classifications (see figures 32 and 33). The relationship between the IPV ratio and $1/\sin(i)$ was also utilized to calculate estimated SMBH masses.

Analysis of IPV ratios (polarized to total) and polarization percentage ratios (core to continuum) again demonstrated a distinction between the two classifications. In this case, a clear split was found (see figure 35). All polar-class objects (with the exception of one outlier) were located below this split, while all equatorial-class objects were above it. This split was determined empirically and is merely a representation of the trend seen in our data.

Differences in centroid locations between total and polarized flux spectra are seen in our data. Equatorial-class objects seem to have their polarized flux spectra preferentially redshifted while polar-class objects display a preferential blueshifting (compared to total flux spectra). These results point to the existence of relative bulk motion of the scatterers and emission disk.

Finally, Kolmogorov-Smirnov tests comparing multiple subsets of our sample again implied similar differences (see section 6.6). When comparing the IPV ratio, total IPV, and polarized IPV values between equatorial- and polar-class objects, we found that it was unlikely that they were drawn from the same distribution. In other words, the test indicates a fundamental difference between equatorial- and polar-class objects in both total flux and polarized flux spectra.

Within our equatorial-class objects, the KS test indicated that the total and polarized IPV values were possibly drawn from separate distributions, though the results were inconclusive. It should be noted that a systematic difference between the two subsets is expected as a result of the two-component scattering model. For polar-class objects, the test indicated that the total and polarized IPV values were drawn from the same distribution.

7 Conclusions

7.1 Distinctions In Polarization Classification

The analysis detailed in chapter 6 indicates a significant distinction between equatorial- and polar-class objects. These differences are very clearly displayed across multiple separate analysis techniques and are generally consistent with predictions of the two-component scattering model.

7.1.1 Total flux and polarized flux IPV Comparison

We have found that equatorial- and polar-class objects display a clear contrast in their IPV distribution. Figure 31 shows the difference in distribution of IPV values. Equatorial-class objects lay above the line of best fit for the sample as a whole, while polar-class objects largely fall below this line. Linear fits to the individual classifications furthered these conclusions.

The histograms of IPV ratios, total flux IPVs, and polarized flux IPVs further display this distinction (see figures 43, 44, and 45 respectively). In each of these cases, the distribution of equatorial-class objects is visibly separate from that of polar-class objects. This indicates a difference in the distribution of IPV values between classifications with equatorial-class objects having broader Hα lines in both total and polarized flux.

The significantly larger IPV ratios of equatorial-class objects likely stems from the viewing angle difference between the scatterers and the observer. The two-component scattering model suggests that the equatorial scattering region is co-axial with the emission disk, causing it to "see" it edge-on. This leads to the systematically higher polarized IPV (compared to total flux IPV) we see in this class.

Equatorial-class objects are observed from a low inclination, when the BLR and the equatorial scattering region itself are not blocked by the torus. This more face-on viewing angle causes the Hα line to have a lower total flux IPV than polarized flux IPV. In conjunction with the larger polarized flux IPV, equatorial-class objects should have high IPV ratios. These expectations are well-represented throughout our analysis.

7.1.2 IPV Ratio Versus Polarization Ratio

In section 6.3, we compared the IPV ratio (polarized IPV divided by total IPV) to the polarization ratio (core polarization percentage divided by continuum polarization percentage). We found that there was a distinct separation between equatorial- and polar-class objects (see figure 35). With the line defined by equation 106 separating all of the equatorial-class objects in our sample from all but one of the polar-class objects (being Mrk 1239).

We see that polar-class objects have higher polarization ratios and lower IPV ratios than equatorial class objects. This means that polar-class objects have (on average) higher core polarization and lower polarized flux IPV than equatorial-class objects. Higher core polarization indicates that more of the light in the broad-line Hα region which reaches the observer is polarized, while lower polarized flux IPV points to a face-on viewing of the emission disk by the scatterers.

The two-component scattering model also suggests that polar-class objects have lower polarized flux IPVs (compared to total flux IPVs) since they view the emission disk face-on. This leads to a higher degree of core polarization percentage when compared to equatorial-class objects, since a large portion of the polarized flux is concentrated in the core of the line profile. The division displayed in these data indicate that each classification of object not only "sees" the emission disk differently, but they also have different geometries when projected on the sky. These properties are clearly shown in our analysis.

7.1.3 Kolmogorov-Smirnov Tests

In section 6.6, we explored how the distribution of IPV ratio, total flux IPV, and polarized flux IPV values compare both between and within the two major classifications of AGN. The results of these tests are contained in table 8 and represent the likelyhood that each of the two samples are drawn from the same distribution. In short, it indicates whether the two tested parameters are caused by the same physical process.

The KS test indicates that the IPV ratios, total IPVs, and polarized IPVs for equatorial- and polar-class objects are drawn from separate distributions. This points to a difference not only in the relative orientation of the scattering region and emission disk, but also the projection of the object on on the sky. These results support the two-component scattering model, as the polar scattering region is thought to view the emission disk face-on while the equatorial scattering region is thought to view the emission disk edge-on.

Polar-class objects did not display a significant difference in total and polarized IPV distributions which is inconsistent with the model. The polar scattering region is expected to be along the axis of rotation, viewing the emission disk face-on and leading to narrow polarized flux emission lines. On the other hand, the total flux emission lines for our objects are all rather broad. This indicates that we should observe polar-class objects to have lower polarized flux IPV than total flux IPV, which is not shown in our analysis.

Equatorial-class objects, on the other hand, did indicate separate distributions for total and polarized IPV. Again, the two-component scattering model is supported by this observation. Equatorial-class objects are viewed from a more face-on orientation in the sky, leading to lower total flux IPV values compared to polarized flux IPV. The equatorial scattering region, on the other hand, views the emission disk edge-on and causes a high polarized IPV. As a result, the polarized IPV values of equatorial-class objects should be systematically higher than total IPV values.

7.1.4 Summary of Classification Conclusions

Our results indicate a clear distinction between equatorial- and polar-class objects consistent with the classifications we've enforced on the sample. The equatorial-class objects displayed significantly higher IPV ratios than polar-class objects. Plotting IPV ratio versus polarization ratio again displays a clear division between equatorial- and polar-class objects. Finally, KS tests pointed to a difference in distributions between the two classifications for IPV ratio, total IPV, and polarized IPV values.

These distinctions are in-line with the two-component scattering model. The model suggest the existence of two distinct scattering regions within AGN, one viewing the emission disk from an edge-on orientation (the equatorial scattering region) and the other from a face-on orientation (the polar scattering region). The significant differences in scattering geometry between these two classifications is expected to lead to significant differences between the samples, a result which is shown in our analysis.

7.2 Polarization Position Angle Swing and Core Polarization

Figure 36 displays an interesting relationship between polarization angle swing and core polarization. At low core polarization percentages (less than approximately 1%) we find mostly equatorial-class objects. These objects display PA swings from as low as about 20 degrees to as high as over

100 degrees. With one exception (MS 1849.2-7832), we find no equatorial-class objects with core polarization percentages above 1% and only two with PA swings less than 20 degrees.

At high core polarization percentages (those higher than 1.5%) we find exclusively polar-class objects. With one exception (Mrk 915), these objects all display PA swings less than 30 degrees. Only two objects (Mrk 915 and NGC 3227) had core polarization percentages less than 1%.

Our data also display a larger structure across the whole sample. This "envelope" encompasses all of our objects and limits objects with high core polarizations to low PA swing values. Furthermore, we see a large spread in PA swing values in low core polarization objects. As the polarization of the core increases, the spread in PA swing decreases. Furthermore, the tail of this envelope (high core polarization and low PA swing) contains exclusively polar-class objects.

These data display many characteristics expected as a result of the two-component scattering model (see section 3). Firstly, we see that the majority of our polar-class objects have lower PA swings than our equatorial-class objects. According to the model, the polar scattering region views the emission disk from a face-on orientation, while the equatorial scattering region is expected to be co-axial with the emission disk. This should lead to polar-class objects having systematically lower PA swings (compared to equatorial-class objects), a result mirrored in our data.

The data also show a clear relationship between object class and core polarization percentage, with polar-class objects displaying higher core polarization on average than equatorial-class objects. As discussed in section 7.1.3, polar objects are expected to have narrow polarized emission lines, leading to higher core polarization compared to equatorial-class objects. As such, these results support the two-component scattering model as well.

The observed envelope can be considered a result of these effects together. Polar-class objects are expected to have both higher core polarization percentages in addition to lower PA swing values. As a result, the only objects with high core polarization percentages are those with low PA swings, leading to the "tail" seen in 35. Similarly, equatorial-class objects are expected to have a high range of possible PA swing values while maintaining low core polarization percentages, leading to the remaining features in the aforementioned plot.

The conformity of our data to the results predicted by the two-component scattering model is evidence towards the accuracy of the model. Further studies could increase the density of data in the tail of the distribution, allowing a better approximation of the envelope's shape.

7.3 Relative Motion of Scatterers and the Emission Disk

Figure 37 points to significant relative motion between the scatterers and the emission disk in both classifications of AGN. The results indicate that equatorial-class objects have their polarized flux spectra preferentially redshifted while polar-class objects have their polarized flux spectra preferentially blueshifted (compared to their total flux spectra). Each of these preferences imply relative motion between the scatterers and the emission disk.

Equatorial-class objects display polarized flux spectra which are redshifted compared to their total flux spectra. Redshifting is resultant from relative motion bringing the source and the observer further apart. This can occur in one of two ways: the scattering medium traveling away from a stationary source or a source traveling towards a stationary scattering medium. Since the equatorial scattering region is coaxial with the emission disk, this translates to either outwards radial motion of the scatterers and/or inwards radial motion of the emission disk.

It is unlikely that the emission disk is infalling at rates comparable to those seen in our results (hundreds of kilometers per second). Thus, we conclude that these redshifts are evidence of outwards radial motion of the equatorial scattering region. This result is consistent with a coaxial ring of scatterers being pushed outwards by radiation pressure from a highly active accretion disk.

Polar-class objects display blueshifted polarized flux spectra (relative to their total flux spectra). Blueshifting is a result of relative motion which brings the observer and the source closer together. Similar to redshifting, it can be caused either by the scattering medium moving towards a stationary source, or a source moving towards a stationary scattering medium. Since the polar scattering region is along the axis of rotation, this blueshift indicates either a polar outflow of emitting material, and/or polar infall of the scatterers.

The more likely of these scenarios is polar ejection of emitting material. This scenario is supported as a possibility by the presence of polar jets in some AGN (see section 1.2.2).

7.4 SMBH Mass Estimation

Figure 32 displays the linear relationship between the polarized and total flux IPVs. The data clearly show that for equatorial-class objects, the polarized flux IPV is systematically higher than the total flux IPV. This is a result of the inclination of the system, which can be extracted from the ratio of the two IPV values. With the line-of-sight velocity and the inclination, it is possible

to determine the Keplerian velocity of the broad-line-emitting disk and – from this – estimate the mass of the central body.

For equatorial-class objects, we found that the mass of the central SMBH was of order $10^6 M_\odot$ to $10^8 M_\odot$. These mass estimates are consistent with other current estimations. Furthermore, our results are comparable to values presented in the literature.

7.5 Luminosity Dependence of AGN Parameters

Comparisons between polarized flux IPV and object luminosity proved inconclusive. Attempts at fitting the data linearly in each of these cases produced fits with large uncertainties (see figures 27, 28, 29, and 30). For both the sample as a whole and the equatorial-class objects alone, this indicates that there is no clear relationship between the two properties. A similar non-relation is suggested in the distribution of total flux IPV values compared to object luminosity.

In section 6.1 we outlined a theoretical relationship between the luminosity of AGN and their polarized inter-percentile velocity. This relationship is expressed in full as equation 76, though we simplified this expression in a linear form (equation 79) to compare it to our data. The two main parameters of interest are the virial factor (Υ), which accounts for geometry and detailed dynamics of the BLR, and the Eddington ratio (f), which is the fraction of the Eddington luminosity at which the AGN radiates. Results from other studies have shown that the other parameters in equation 76 are likely not strongly correlated with AGN luminosity.

If neither the virial factor nor Eddington ratio are strongly correlated to AGN luminosity, we would expect a linear relationship between the logarithms of the polarized IPV values and the AGN luminosities across our sample. We would also expect to see some vertical offset – the logarithm of the proportionality constants.

Since our results did not show a clear linear correlation between the two quantities, it is possible that one or more of the assumptions made in our theoretical approach are incorrect. The most direct explanation is that there is no significant relationship between polarized flux IPV and object luminosity. While the theory does indicate a relationship between the velocity dispersion of the Blr and the luminosity, it may be the case that the polarized IPV and velocity dispersion are not as simply related as expected.

Upon limiting our sample to only the objects classified as equatorial, the fit approaches what is expected (see figure 30 and the associated fit given by equation 83). Again however, the uncertainty

of the fit is quite large. Due to the fact that polar-class objects have their scattered light sampling only a portion of the Keplerian velocity field, this reduced selection is expected to provide more significant results.

Overall, these results indicate that there is some issue(s) with our theoretical approach. While our fits did provide slopes that were of the proper value within uncertainty (at least for equatorial-class objects), the uncertainties themselves were large. As such, the results presented here are much more speculative than conclusive.

In the future, more numerous and more precise measurements of the total and polarized flux IPV could lead to a more conclusive result. If this non-correlation were seen again, it could point to a more complex relationship between polarized IPV and luminosity and/or between the polarized IPV and velocity dispersion. If a stronger linear fit which deviated from the predicted result were found, it would be possible to extract information regarding the luminosity dependence for the product of the virial factor and Eddington ratio. If the expected linear fit was found, the value of the product $k\Upsilon f^{1/2}$ could be extracted instead.

7.6 Major Findings

This study represents the analysis of the largest pool of polarization spectra of broad-line AGN studied to date. Looking at AGN through the lens of spectrapolarimetry has proven useful in the past, but it wasn't until now that the field has had a sample this large to explore. This analysis has given us supporting evidence for the two-component scattering model of AGN and opens avenues to more in-depth future research.

Comparison between IPV values (both polarized and total) and AGN luminosity produced fit parameters which were close to expected values, though the fits themselves had large uncertainties. This indicates that there is no significant correlation between the two properties, but better data is required to confirm this. It is possible that this is a result of a more complex relationship between polarized IPV and orbital velocity of the scatterers which was not accounted for.

Multiple tests supported the two-component scattering model (which was utilized to classify the objects in our sample as equatorial- and polar-scattering dominated objects). Distributions of IPV values (both total and polarized) displayed a clear difference between equatorial- and polar-class objects. This qualitative result was strengthened by quantitative results from KS tests between the same parameters, which indicated that the two subsets had their IPV ratio, total IPV, and polarized IPV values drawn from different distributions. This clear difference is seen again when plotting

IPV ratio versus polarization ratio, allowing a linear boundary to be drawn between the two subsets. These results all directly support the two distinct classifications which would come from the two-component scattering model.

A separation in the two classifications is also seen when comparing PA swing and core polarization. The distribution shows another interesting trend; an "envelope" which encompasses the entirety of our sample. No objects with high core polarization (greater than 1.5%) were found to have large PA swings (greater than 30°), while objects with low core polarization had no preferential PA swing range. This leads us to believe that there are no objects which have both a high core polarization and a high PA swing. This trend is supported by the two-component scattering model, as these high core-polarization objects would be largely polar-scattering dominated, leading to low PA swing (as the polar scattering region would see the emission disk face-on).

Using polarized flux IPV values, we were able to estimate the masses of the central SMBHs across in our sample without the need for direct measurements of the system inclination. The masses found were of order $10^{6-8} M_{\bullet}$; consistent with other mass estimations. Estimating the mass of the same objects using their total flux IPV values gives masses which are about half of those found using the polarized IPV, further supporting the two-component scattering model. These results open the possibility for a refined method of determining black hole masses.

Analysis of the the locations of total and polarized flux centroids indicated relative motion between the emission disk and both scattering regions. Equatorial-class objects displayed a preferential redshift, while polar-class objects displayed a preferential blueshift. These velocity shifts indicate two different cases of relative motion; one for each scattering region. Our results indicate an outward radial motion of the equatorial scattering region and a polar outflow of emitting material.

Finally, a distinction in distribution of total IPV and polarized IPV values is seen within equatorial-class objects. A KS test of this sample indicated that it was possible these two subsets were drawn from the same distribution, though the confidence of this result is rather low. This result is supportive of the two component scattering model. Equatorial-class objects are expected to be observed from a more face-on orientation (since the torus is not blocking the light from the equatorial scattering region), while the equatorial scattering region itself sees the emission disk edge-on. This dichotomy is expected to result in systematically higher polarized IPV values (compared to total IPV) within equatorial-class objects.

References

[Akiyama et al. 2019] Akiyama, K., Alberdi, A., Alef, W., et al., 2019, ApJ, **875L**, 5E

[Alexander & Netzer 1994] Alexander, T., Netzer, H., 1994, MNRAS, **270**, 781

[Alloin, Boisson, & Pelat 1988] Alloin, D., Boisson, C., Pelat, D., 1988, A&A, 200, 17A

[Angel & Stockman 1980] Angel, J.R.P., Stockman, H.S., 1980, ARA & A, **18**, 321

[Antonucci & Miller 1985] Antonucci, R.R.J., Miller, J.S., 1985, ApJ **297**, 621 (AM85)

[Antonucci 2001] Antonucci, R.R.J., 2001, in Astrophysical Spectropolarimetry, Trujillo-Bueno, J., Moreno-Insertis, F., Sanchez, F. (eds), Cambridge University Press, Cambridge

[Barthe, Greene, & Ho] Barthe, A.J., Greene, J.E., Ho, L.C., 2005, ApJ **619**, L151

[Barthel 1992] Barthel, P.D., 1992, in Physics of Active Galactic Nuclei, Duschl, W.J., Wagner, S.J. (eds), Springer-Verlag, Heidelberg

[Botte et al. 2004] Botte, V., et al., 2004, ApJ, **127**, 3168

[Bradley & Puetter 1986] Bradley, S.E., Puetter, R.C., 1986, A & A, **165**, 31

[Bentz et al. 2009] Bentz, M.C., et al., 2009, ApJ, **697**, 1

[Bentz et al. 2013] Betnz et al., 2013, ApJ, **767**, 149

[Bentz & Katz 2015] Betnz, M.C., Katz, S., 2015, in Publications of the Astronomical Society of the Pacific, **127**, 67

[Carone et al. 1996] Carone, T.E., Peterson, B.M., Bechtold, J., et al., 1996, ApJ, **471** 717

[Christopoulou et al. 1997] Christopoulou, P.E., Holloway, A.J., Steffen, W., et al., 1997, MNRAS, **284**, 385

[Clavel et al. 1991] Clavel, J., Reichert, G.A., Alloin, D., et al., 1991, ApJ, **366**, 64

[Clavel et al. 1992] Clavel, J., Nandra, K., Makino, F., et al., 1992, ApJ, **393**, 113

[Coleman & Shields 1990] Coleman, H.H., Shields, G.A., 1990, ApJ, **363**, 415

[Collin-Souffrin et al. 1988] Collin-Souffrin, S., Dyson, J.E., McDowell, J.C., et al., 1988, MNRAS, **232**, 539

[Collin-Souffrin 1991] Collin-Souffrin, S., 1991, A & A, **249**, 344

[Collin & Kawaguchi] Collin, S., Kawaguchi, T., 2004, A&A, **426**, 3

[Das et al. 2006] Das, V., Crenshaw, D.M., Kraemer, S.B., et al., 2006, ApJ, **132** 620D

[Disney et al. 1995] Disney, M.J., Boyce, P.J., Baldes, J.C., et al., 1995, Nature, **376**, 150

[Disney 1998] Disney, M, 1998, Sci.Am., **278**, 36

[Doroshenko et al. 2012] Doroshenko, V.T., et al., 2012, Monthly Notices of the Royal Astronomical Society, **426**, 1

[Edwards 1980] Edwards, A.C., 1980, MNRAS, **190**, 757

[Eracleous & Halpern 1994] Eracleous, M., Halpern, J.P., 1994, ApJS, **90**, 1

[Evans et al. 1993] Evans, I.N., Tsvetanov, Z., Kriss, G.A., et al., 1993, ApJ, **417**, 82

[Fabian et al. 1995] Fabian, A.C, Nandra, K., Reynolds, C.S., et al., 1995, MNRAS, **277**, L11

[Greene et al. 2010] Greene, J.E., Hood, C.E., Barth, A.J., 2010, ApJ, **723**, 1

[Haardt, Maraschi, & Ghisellini 1994] Haardt, F., Maraschi, L., Ghisellini, G., 1994, ApJ, **432**, L95

[Halpern et al. 1996] Halpern, J.P., Eracleous, M., Filippenko, A.V., et al., 1996, ApJ, **464**, 704

[Heckman et al. 1995] Heckman, T.M., Krolic, J., Meurer, G., et al., 1995, ApJ, **452**, 549

[Hutchings, Janson, & Neff 1989] Hutchings, J.B., Janson, T., Neff, S.G., 1989, ApJ, **342**, 660

[Jackson, Paglioni, & Ishizuki 1993] Jackson, J.M., Paglioni, T.A.D., Ishizuki, S., 1993, ApJ, **418**, L13

[Kaspi et al. 2000] Kaspi, S., Smith, P.S., Netzer, H., et al., 2000, ApJ, **533**, 631

[Kassebaum, Peterson, & Wanders 1997] Kassebaum, T.M., Peterson, B.M., Wanders, I., 1997, ApJ, **475**, 106

[Kollatschny & Zetzl 2010] Kollatschny, W. & Zetzl. M., 2010, A&A, 522, A36

[Krolik et al. 1991] Krolik, J.H., Horne, K., Kallman, T.R., et al., 1991, ApJ, **371**, 541

[Lane 2007] Lane, D.M., 2007, *Introduction to Statistics (Online Edition)*, Rice University

[Macchetto, Capetti, & Sparks 1994] Macchetto, F., Capetti, A., Sparks, W.B., 1994, ApJ, **435**, L15

[Marco & Alloin 2000] Marco, A., Alloin, D., 2000, A & A, **353**, 465

[Mundell, Holloway, & Pedlar 1995] Mundell, C.G., Holloway, A.J., Pedlar, A., 1995, MNRAS, **275**, 67

[Nandra et al. 1997] Nandra, K., George, M., Mushotzky, R.F., et al., 1997, ApJ, **477**, 602

[Netzer 1990] Netzer, H., 1990, in Active Galactic Nuclei, Saas-Fee Advance Course 20 Lecture Notes, Springer-Verlag, Berlin

[Netzer 2008] Netzer, Hagai, 2008, New Astronomy Reviews, **52**, 6

[Norman & Scoville 1988] Norman, C., Scoville, N., 1988, ApJ, **332**, 124

[Osterbrock 1993] Osterbrock, D.E., 1993, ApJ, **404**, 551

[Padovani 1993] Padovani, P., 1993, MNRAS, **263**, 461

[Penston 1988] Penston, M.V., 1988, MNRAS **233**, 601

[Peterson et al. 1991] Peterson, B.M., et al., 1991, ApJ, **368**, 119

[Peterson 1997] Peterson, B.M., 1997, *An Introduction to Active Galactic Nuclei*, Cambridge University Press, Cambridge

[Peterson et al. 2004] Peterson, B. M., et al., 2004, ApJ, **613**, 2

[Planesas, Scoville, & Myers 1991] Planesas, P., Scoville, N.Z., Myers, S.T., 1991, ApJ, **369**, 364

[Pogge 1989] Pogge, R.W., 1989, ApJ, **345**, 730

[Robinson 1995] Robinson, A., 1995, MNRAS, **272**, 647

[Runnoe, Brotherton, & Shang 2012 (1)] Runnoe, J.C., Brotherton, M.S., Shang, Z., 2012, Monthly Notices of the Royal Astronomical Society, **422**, 478

[Runnoe, Brotherton, & Shang 2012 (2)] Runnoe, J.C., Brotherton, M.S., Shang, Z., 2012, Monthly Notices of the Royal Astronomical Society, **426**, 478

[Rybicki & Lightman 1979] Rybicki, G.B., Lightman, A.P., *Radiative Processes in Astrophysics*, Harvard-Smithsonian Center for Astrophysics

[Serkowski, Mathewson, & Ford 1975] Serkowski, K., Mathewson, D.S., Ford, V.L., 1975, ApJ, **196**, 261

[Seyfert 1943] Seyfert, C., 1943, ApJ, **97**, 28

[Smith et al. 2002] Smith, J.E. et al., 2002, Monthly Notices of the Royal Astronomical Society, **335**, 3

[Smith et al. 2004] Smith, J.E. et al., 2004, Monthly Notices of the Royal Astronomical Society, **350**, 1

[Smith et al. 2005] Smith, J.E., 2005, Monthly Notices of the Royal Astronomical Society, **359**, 3

[Stripe 1991] Stripe, G.M., 1991, A & A, **247**, 3

[Tacconi et al. 1994] Tacconi, L.J., Genzel, R., Bleitz, M., et al., 1994, ApJ, **426**, L77

[Taylor et al. 1996] Taylor, G.L., Dunlop, J.S., Hughes, D.H., et al., 1996, MNRAS, **283**, 930

[Terlevich et al. 1992] Terlevich R., Tenorio-Tagle, G., Franco, J., et al., 1992, MNRAS, **255**, 713

[Ulrich, Maraschi, & Urry 1997] Ulrich, M-H., Maraschi, L., Urry, C.M., 1997, ARA & A, **35**, 445

[Urry, & Padovani 1995] Urry, C.M., Padovani, P., 1995, PASP, **107**, 803

[Wanders et al. 1995] Wanders, I., Goad, M.R., Korista, K.T., et al., 1995, ApJ, **453**, L87

[Warner, Hamann, & Dietrich 2004] Warner, C., Hamann, F., Dietrich, M., 2004, ApJ, **608**, 136

[Weymann et al. 1991] Weymann, R.J., Morris, S.L., Foltz, C.B., et al. 1991, ApJ, **373**, 23

[Vestergaard, Wilkes, & Barthel 2000] Vestergaard, M., Wilkes, B.J., Barthel, P.D., 2000, ApJ, **538**, L103

[Zheng, Binette, & Sulentic 1990] Zheng, W., Binette, L., Sulentic, J.W., 1990, ApJ, **365**, 115

A Notes on Individual Objects

A.1 Mrk 1239

Mrk 1239 displays extreme polarization characteristics which coincide with each narrow line. Furthermore, the polarization characteristics of the broad Hα region are very nuanced, displaying significant structure in both the stokes Q and U parameters across the centroid. Figure 46 displays these characteristics.

This unique polarization spectrum is what we believe lead to the oddities this object displays in our analysis. Further study of this object in particular is recommended.

A.2 WAS 45

The post-subtraction spectra of WAS 45 is rather noisy. This is the result of attempts to fit and subtract individual narrow-line profiles present in the observed spectrum. The low signal in conjunction with these noise features likely lead to the inconsistencies displayed by this object. Figure 47

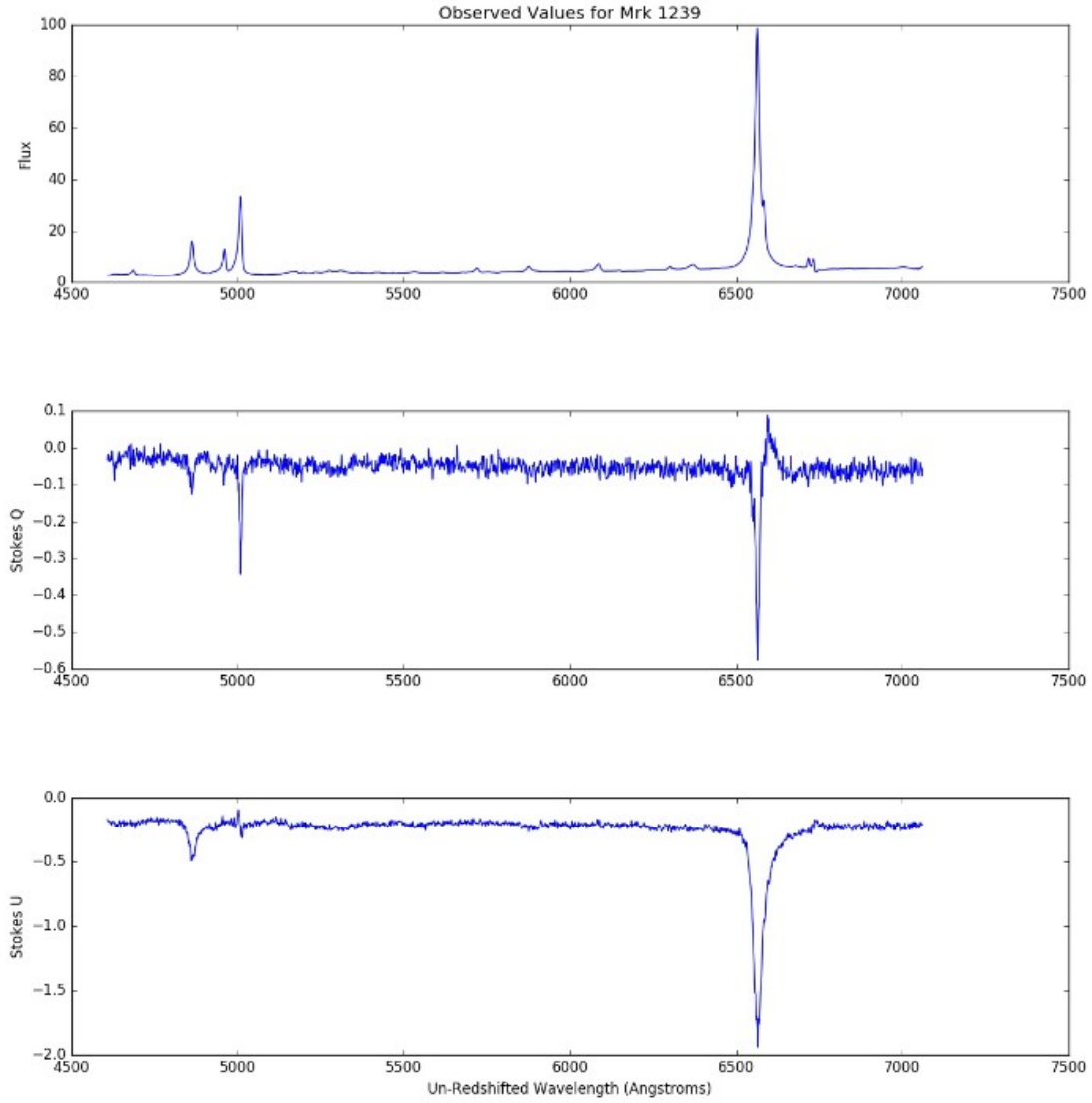

Figure 46: Polarization spectrum of Mrk 1239. This object displays strong polarization signatures which coincide with each narrow line. There is also significant structure across the broad Hα profile.

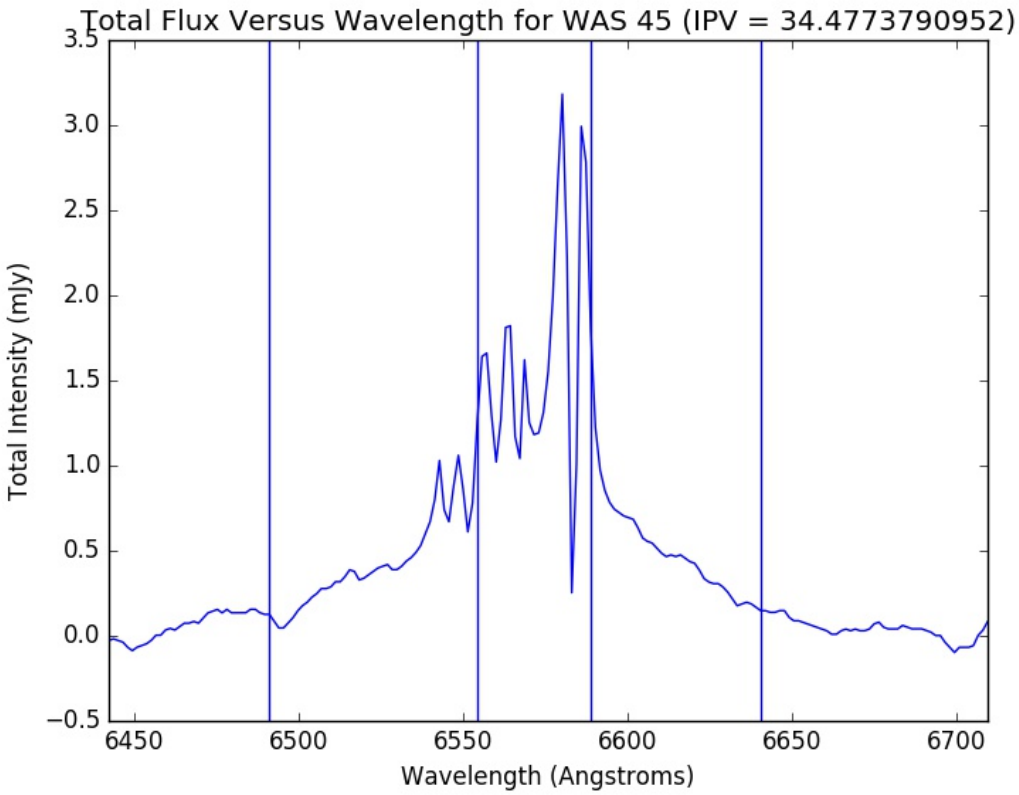

Figure 47: Broad-line Hα profile of WAS 45. the high-noise features displayed across the region are a result of attempted subtraction of the narrow-line profiles present in the observational data.